Phase Transitions and Mesophases in Molecular Liquids and Solutions: Spectroscopic and Imaging Studies

Joanna Edyta Findlay

School of Chemistry

University of Glasgow

Submitted in fulfilment of the requirements for the degree of

Doctor of Philosophy

I declare that, except where due reference is made, that this thesis for the degree of Doctor of Philosophy is my own work and has not been submitted for any other degree at this institution or elsewhere.

Joanna Edyta Findlay
University of Glasgow
October 2017

PUBLICATIONS COVERED IN THIS THESIS

Crystal templating through liquid–liquid phase separation
Joanna Mosses, David A. Turton, Leo Lue, Jan Sefcik and Klaas Wynne
Chem. Commun., 51, 1139-1142 (2015)

Order parameter of the liquid-liquid transition in a molecular liquid
Joanna Mosses, Christopher D. Syme, and Klaas Wynne
J. Phys. Chem. Lett., 6, 38-43 (2015)

Frustration of crystallisation by a liquid–crystal phase
Christopher D. Syme, Joanna Mosses, Mario González-Jiménez, Olga Shebanova, Finlay Walton and Klaas Wynne
Sci. Rep., 7, 42439 (2017)

Acknowledgements

First of all I would like to thank my supervisor Klaas Wynne for giving me the opportunity to work on this PhD project. His passion for science, enthusiasm and guidance are what motivated me to carry on with my work despite months of not working experiments. The fact that I was able to submit this thesis, after almost three years since completing my experiments, is the biggest gift of his support. It has been a privilege to work under his supervision.

Secondly, my thanks go to Chris Syme for hours spent working on our FLIM and Raman experiments, which resulted in an abundance of publishable data and two papers (great team work Chris!). His perseverance, patience and calm approach to experimental obstacles made the time spent in the lab not only very productive but really enjoyable.

My special thanks go to David Turton whose hard work and drive to achieve perfection in everything he does was very inspiring and highly motivating. He is the creator of our DIY low-temperature glove box, which made our experiments possible. His knowledge and constructive criticism undoubtedly improved the quality of my work.

I also would like to thank other members of my research group - Mario, Gopa, Judith and Andy – for their help, support and friendship. I always felt I could count on them and our coffee breaks were a great way to vent our scientific frustration and motivate each other.

Outside of work I would like to thank Richard for his never-ending support and constant reminding of what a PhD is really about. This really helped me through some difficult moments. I would also like to express my deep gratitude to my parents for their love, support and the gift of independence from early childhood, which helped me to pursue my dreams at every stage of my life that includes moving from Poland to Scotland, which is now my home.

I also wish to thank my work supervisor Donald Hay for his amazing support and understanding. Thanks to him I was able to write my thesis whilst working full-time as a police officer with a demanding shift pattern.

Lastly, I wish to thank my wonderful family – Russell and Daisy. Their drive to achieve their goals, love and constant support is what made me sit down between my shifts and write this thesis to make my dream come true and make them proud. They are both a constant source of my inspiration.

Thank you all very much.

Abstract

Liquids are the primary medium for chemical and biological reactions. Phase transitions can give rise to phase separation through nucleation or spinodal decomposition. This phase separation may be the reason behind structure in many liquids, which then has an effect on more practical processes. Mesoscopic (1 nm-1 μm) structuring of the liquid in the neighbourhood of a second critical point associated with a liquid-liquid transition (LLT) can cause anisotropic diffusion, which greatly affects the wetting properties of the liquid. It may also segregate reactants and products, affecting reaction rates and outcomes. Some examples of processes, which may be affected by this, include the synthesis and preparation of pharmaceutical drugs (which is sensitive to liquid structure, phase separation, and nucleation), preparation of nanometre scale materials, electrochemistry, dye-based solar cells, separation technology, and heterogeneous catalysis.

This thesis concentrates on advancing of the understanding of some of the phase transitions and mesophases occurring in liquids. The first two chapters are introductory and the remaining chapters describe original research.

Chapter 3 describes our studies on crystal nucleation in the presence of a liquid-liquid phase separation. The subjects of these studies were two binary liquid systems: nitrobenzene-hexane and water-1,2-*trans*-dichloroethylene. Our discovery of template-less asymmetric water crystals (water fluff), which we were able to reproduce repeatedly, strongly suggests that, despite common belief, high driving force does not necessarily lead to ill-defined crystalline forms. We also propose that crystal templating induced by liquid-liquid phase separation might be a general phenomenon, not limited to water.

In Chapter 4 we explore one of the most interesting and challenging postulates in the field of liquid science, that is the existence of more than one isotropic liquid states in a single-component liquid at constant temperature and an LLT between these different states. By employing a number of experimental techniques, some of them not previously used to study this subject, we provide a new evidence for the existence of the LLT in triphenyl phosphite (TPP). Furthermore we answer an important and fundamental question of what is the order parameter characterising the LLT in TPP.

Finally, Chapter 5 shows how our investigations into the existence of the LLT in *n*-butanol led to the conclusion that the observed phenomenon is in fact a transition

between a supercooled isotropic liquid and a liquid-crystalline (LC) state. The LC is in general considered a form of matter “in between” the liquid and the crystal. However, the LC phase in n-butanol geometrically frustrated the formation of the stable crystalline phase. This frustrated phase can be seen as a template for similar ordering in other molecular liquids and is likely to be essential in their supercooling and LLTs.

Contents

List of Figures

List of Tables

1

Introduction

Due to its fluidity, the liquid state of matter is convenient for processing and controlling chemical reactions. Understanding of the structure of liquids and solutions is of enormous relevance to chemistry, chemical engineering and related fields. This chapter introduces the underlying principles of the liquid-state phenomena, which are the subject of this research, along with a survey of current thinking around these topics.

1.1 Liquid-Liquid Transition

The basic concept behind a liquid-liquid transition (LLT) is that a liquid is not just a single amorphous state. Experimental and theoretical studies suggest that not only are liquids not homogeneous but more than two liquid states may exist even for a single-component material as a function of temperature. The term "polyamorphism" was introduced to describe this phenomenon of the existence of multiple states in amorphous materials, by analogy with the term polymorphism, which was long used for crystalline phases. The transition between two liquid states is thought to be an amorphous to amorphous (polyamorphic) transition.[1-3] Such transition is predicted to be similar to a gas-liquid transition, except that it occurs between two states of the liquid.[4]

The topics of polyamorphism and LLTs have gained increasing interest since Mishima *et al.* reported the existence of two amorphous phases in water, differing in density by about 23%.[5, 6] Since then, other examples of polyamorphism have been observed.

The direct observation of coexistence of two liquid phases at ambient pressure in the supercooled melt Al_2O_3- Y_2O_3 just above the glass transition temperature was reported by Aasland and McMillan. These two phases differed in density even though their chemical composition, confirmed by electron probe analysis, was identical.[7] However, the composition range and experimental conditions required to observe this phenomenon are still a matter of debate.[8]

High-pressure experiments[9-11] and numerical simulations[12] suggested the existence of more than one amorphous (or even liquid) phases in silicon. Two amorphous phases were observed in silicon dioxide (SiO_2) and their distinction confirmed by X-ray diffraction studies[13] and sound velocity measurements.[14]

Synchrotron X-ray scattering facilitated a discovery of the first-order LLT in phosphorus (P) at high pressure and high temperature.[15, 16] The coexistence of both liquid phases was confirmed and their structure factors were obtained revealing that during this transition phosphorus transformed from tetrahedral to network-forming polymeric liquid. Further studies showed that phosphorus undergoes the first-order transition between a high-density molecular fluid and a low-density polymeric liquid.[17] These results were supported by the first principle simulation carried out by Morishita.[18]

Hints of a first-order reversible transition between two amorphous states were found in germanium dioxide (GeO_2) through experimental high-pressure X-ray absorption spectra.[19, 20]

Theoretical predictions and experimental evidence suggested the existence of an LLT in carbon (C)[21-23], although this phenomenon is a subject of a debate.[24, 25]

Another promising candidates for an LLT at ambient conditions are colloidal liquids, however experimental evidence is still to be obtained as it presents practical challenges.[26, 27]

Until 1996, the most common examples of polyamorphism were substances characterised by an open, tetrahedral network of bonds at ambient conditions (*e.g.* water, SiO_2, GeO_2). When treated with high pressure or temperature, these networks might have collapsed forming a second denser structure. In 1996, Kivelson *et al.* reported the discovery of the first-order transition leading to a new amorphous solid phase in the glass-former triphenyl phosphite (TPP) existing at normal pressure, with no rigid

three-dimensional network.[28] LLTs have also been suggested for *trans*-1,2-dichloroethylene and *n*-butanol at atmospheric pressure.

It has been predicted that LLTs should be common in all molecular liquids[29] but despite all the evidence, the phenomenon of LLTs remains controversial and the physical origin of this phenomenon is largely unknown. This is mainly due to experimental difficulties. For example, where the transition occurs at high temperature and pressure (*e.g.* for P, C)[30] or is hidden by crystallisation (*e.g.* water).[31]

1.1.1 Water

Water is the most common and the most important liquid on Earth - without it life would not survive. But it seems that the properties, which make water 'the solvent for life', also make it the most unusual of all liquids as this simple molecule exhibits various thermodynamic and kinetic anomalies.[1, 32-34] Its density maximum at 277 K, discovered in the 17th century by the members of the 'Academie del Cimento' - a scientific society based in Florence,[35] enables life to exist under the surface of frozen lakes, seas and other reservoirs. Other anomalies include the density decrease upon its freezing at 273 K, and the increase in heat capacity and isothermal compressibility upon supercooling.[36] The shear viscosity also behaves anomalously – initially decreases with increasing pressure but above ~ 2 kbar starts to increase again.

In principle, below T_m at normal atmospheric pressure, water should crystallise forming hexagonal ice I_h. However, under high pressure the open tetrahedral structure of I_h progressively collapses, density increases, resulting in over 15 different crystal polymorphs. Water can also be supercooled, as was first described in 1775 by Joseph Black.[37] Four centuries later, despite extensive studies, there is still no consensus to the origin of water's peculiar behaviour. Many theories have ascribed it to the unique features of hydrogen bonding.[38-40] In the 1970s, Speedy and Angell proposed a concept known as "stability limit conjecture" which suggested that nearing the limit of mechanical stability of the supercooled liquid phase (at ~220 K at atmospheric pressure) could explain many odd behaviours of water.[41]

In the following decade, Mishima *et al.* discovered that there are at least two amorphous forms of water: high-density amorphous (HDA) and low-density amorphous (LDA) ices with the transition between them of the first-order nature.[42, 43] LDA can be prepared by vapour deposition or hyperquenching at 77 K. When LDA is pressurised to

10 kbar at 77 K, HDA is formed and remains stable even if the pressure (at this temperature) is lowered to 1 atm. HDA can be converted to LDA by heating to 120 K. Raman and neutron scattering studies revealed that the structure of LDA ice is similar to the I_h, whilst the structure of HDA ice resembles high-density ice VI.[44-46]

The existence of these two low-temperature amorphous forms of water implied that there are at least two liquid states in water and an LLT between them. This discovery formed a basis for another hypothesis, which suggested the existence of a liquid-liquid critical point (or a second critical point, LLCP) associated with an LLT,[47, 48] which is supported by a number of computer simulations.[49, 50] The simulated location of the LLCP was compared to the location predicted from experiments, however the results were inconclusive as even the smallest change in the water potential significantly shifted the location of LLCP.[34] Some theories propose that critical phenomena associated with an LLT may explain peculiar properties of water.[1, 32-34]

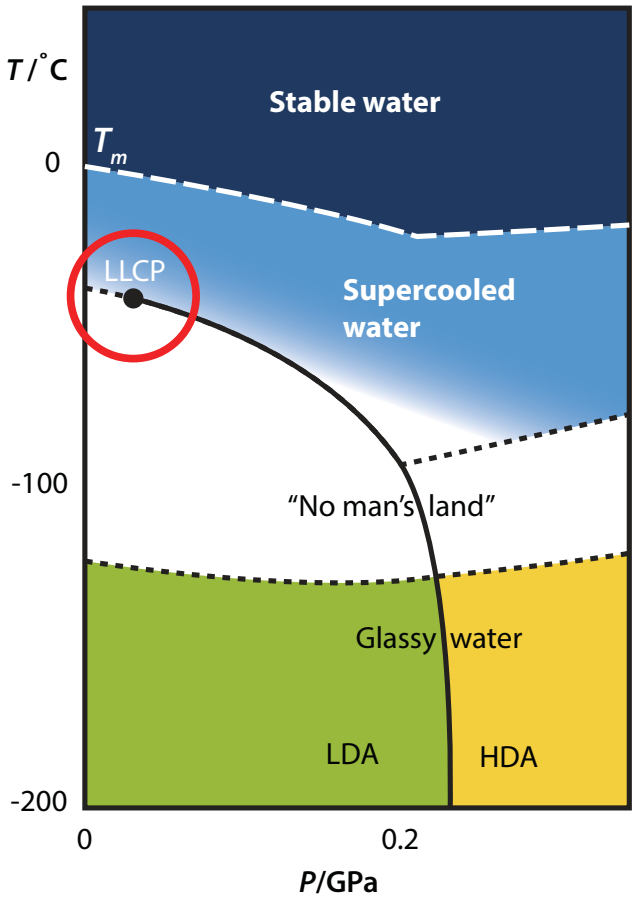

Figure 1. *The amorphous forms of water at one atmospheric pressure inspired by diagrams presented by Mishima.*[35]

On the other hand, Tanaka argued that a simple two-order-parameter model (explained in detail in Section 1.2), predicting the existence of two competing orderings in water - density ordering and bond ordering, could explain water's anomalies.[50, 51]

The unique properties of water puzzled and fascinated scientists for centuries. There are many hypotheses to explain them, but unfortunately it is very difficult to verify any of them experimentally. The reason for this is that the water's predicted LLT takes place in the physically inaccessible temperature range known as "no man's land" (Figure 1) in the supercooled phase below the homogeneous nucleation temperature. Some up-to-date experimental approaches to access a hidden LLT in water included confinement in nanometre-size pores[52, 53] and protein-hydration water.[54] However, the results of these experiments were not widely accepted as one may argue that the confinement introduced water-wall interactions and the reduced dimensionality not present in bulk liquid.[55-57]

1.1.2 Triphenyl phosphite

In 1996 Kivelson *et al.* discovered what appeared to be a first-order phase transformation at ambient pressure between deeply supercooled liquid and a rigid amorphous-like phase in triphenyl phosphite (TPP), a glass-former with the molecular formula $P(OC_6H_5)_3$ (see Figure 43A). When a sample of liquid TPP was rapidly cooled to the temperature in the range 227-213 K and annealed at this temperature (T_a) for hours, the sample initially got cloudy, then turned opaque and eventually cleared up. The new phase, named "glacial phase", was initially believed to be amorphous as the low-resolution X-ray scattering measurements were practically indistinguishable from the results obtained for the supercooled liquid and the glass. NMR spectroscopy provided no further insight into the structure of the glacial phase, as the lines in the solid-state spectra were extremely broad masking potential shifts of the different phases at low temperatures. Magic-angle-spinning solid state NMR could not be performed due to weight imbalance preventing required spinning of the sample. However measured spin-lattice relaxation times of different solid phases of TPP (liquid/glass, glacial and crystal) were all distinct implying that on molecular level they all differed. On slow heating of the glacial phase, the sample was often lost due to breakage of the glass container indicating that the glacial phase was denser than the stable crystal and it expanded from one rigid phase to another less dense one on heating. At higher temperatures (225-227 K), apparent phase separation and

coexistence of small opaque ball-like regions floating in a clear liquid was observed. The report was concluded with a hypothesis that the glacial phase might be associated with the LDA ice and not in fact be amorphous but defect-ordered, predicted by the frustration-limited domain theory.[58] In such a phase the domains, characteristic of a supercooled liquid, would arrange themselves into a crystal array, where the internal organisation could vary between domains. This hypothesis was based on the results of model calculations and the fact that this type of structure would not be detected by low-resolution X-ray scattering.[59] It was established that the glacial phase was structurally distinct from the crystal and the glass and it existed and was at equilibrium above T_g (T_g ~ 205 K), in fact, it was a more stable phase than the supercooled liquid.[28]

Following the findings of Kivelson and co-workers, several controversial explanations of the nature and origin of this new phase have been proposed. These included the glacial phase being an orientationally disordered crystal or liquid crystal,[60] a rigid solid with a structure resembling orientational glasses or glassy crystals,[61] a nematic crystal or a highly viscous liquid,[62] a highly correlated liquid,[63] an unusual metastable plastic crystal,[58] and a highly ordered amorphous phase.[64] After years of extensive research only two major scenarios remain and are still being explored: the nanocrystals scenario formulated by Hédoux *et al.* and the LLT scenario proposed by Tanaka and co-workers.

1.1.2.1 Nanocrystals Scenario

The main techniques employed by Hédoux and co-workers to investigate the origin and physical nature of the glacial phase were Raman scattering, X-ray diffraction and neutron diffraction.[65-78] All three phases of TPP were studied – the liquid, the stable crystal and the glacial phase. The standard glacial phase preparation (also called the glaciation) protocol involved cooling of the sample below T_g and thereafter increasing the temperature and annealing of the sample at the selected T_a until full transformation was achieved.

Raman scattering investigations of the low-frequency range revealed that the spectrum of the glacial phase corresponded to the perfect envelope of the phonon peaks observed in the crystalline phase, *i.e.* its local order resembled the crystalline symmetry.[65] The Raman spectrum of the glacial phase could be considered as a combination of the spectrum of the crystal and the spectrum of the supercooled liquid. The downshifting of some of the Raman bands, presumably due to the force field inside the crystalline

domains, and significant sharpening of internal modes further supported the scenario of the glacial phase being partially crystalline.[69]

The X-ray patterns obtained at different T_a temperatures in the range 210 – 222 K were interpreted as distinctive stages in the crystallisation process. This process was considered to be aborted, as the glacial phase seemed indefinitely stable without any further heating.[66, 67]

Hédoux and co-workers published a numerous reports on the subject, however their conclusion remained the same – the glacial phase formed in the temperature range 210 – 235 K was composed of untransformed supercooled liquid and crystallites of the stable crystal. The size of these crystallites depended on the temperature at which the glacial phase was prepared. It was suggested that the glacial phase could be described as microcrystalline, rather than nanostructure, above 224 K.[69] The origin of the glacial phase was believed to be the result of high nucleation rate frustrating crystallisation due to the residual supercooled liquid being subdivided (by small crystallised particles) in interstitial volumes not exceeding the critical size for crystallisation.[73]

1.1.2.2 LLT Scenario

In 2004, Tanaka and Kurita reported the results of their studies proposing that the phenomenon observed in supercooled TPP was a result of an LLT and that the new (glacial) phase should be considered a glassy state of the second liquid state (liquid 2), with its own glass transition temperature T_g^2 (T_g^2 = 225 K).[79, 80]

Phase-contrast microscopy images obtained at different T_a revealed two distinct transformation patterns, sharply changing at the spinodal temperature T_{SD}= 215.5 K. The glacial phase was observed below the binodal temperature T_{BN} ~ 230 K. A few different experimental techniques, including morphological observations and rheological and calorimetric measurements, were applied to determine and verify the location of these two temperatures. The proposed schematic LLT phase diagram of TPP in a *T-S* plane is shown in Figure 2.[79, 80]

When TPP was rapidly quenched and annealed at a constant temperature $T_{SD} < T_a < T_{BN}$, the glacial phase nucleated in the form of spherical droplets in liquid 1 and grew with a constant (estimated) speed until the whole system became apparently homogenous again. This behaviour was associated with the nucleation and growth (NG)-type transformation. The digital image analysis was performed on the images

obtained with phase-contrast microscopy. The intensity distribution function *P(I)*, proportional to the density distribution function, was calculated. Initially there was only one peak - peak 1, corresponding to liquid 1. With the appearance of the nuclei of the glacial phase, peak 2 appeared with contrast distinct from peak 1. Over time, the amplitude of peak 1 decreased whilst the amplitude of peak 2 increased. Finally, only peak 2 was present. Neither the positions nor the widths of both peaks changed during the transformation. This *P(I)* pattern was reminiscent of the (NG)-type phase separation in phase-separating binary mixtures.[79]

At lower temperatures, $T_a < T_{SD}$, just after the quench of TPP, in initially homogenous liquid 1, density fluctuations grew very slowly, but continuously. The amplitude of these fluctuations initially increased exponentially, but later decreased, and eventually the whole system became a homogeneous glacial phase. *P(I)* showed a different behaviour to that observed at higher temperatures. With the formation of the glacial phase, the amplitude of peak 1 (liquid 1) decreased and became broader with time. When peak 1 became quite broad, another peak (glacial phase) appeared and grew and sharpened with time. Lastly only peak 2 remained, suggesting the transition was complete. This pattern of the temporal change of *P(I)* was a clear indication that liquid 1 transformed to liquid 2 in a continuous manner and the new phase was formed with a spinodal-decomposition (SD)-type mechanism. The presence of the (SD)-type pattern evolution was not consistent with any first-order transitions between liquid and ordered solids, including plastic crystals, and it was a feature distinctive to an LLT. This strongly suggested that the observed transformation from supercooled liquid to the glacial phase was an LLT. [79]

The estimated, from optical microscopy observations, growth speed and nucleation frequency of the glacial phase domains changed their temperature dependencies at 223 K. The observed steep increase of the nucleation frequency with decreasing T_a and the change of T_a dependencies at 223 K could not be explained by the classical nucleation theory and thus was another argument supporting the LLT scenario.[80]

Rheological evolution also changed its pattern around T_{SD}. The rheological measurements demonstrated that the supercooled liquid 1 was in a viscous fluid state without static elasticity, while the glacial domain was in a glassy state of liquid 2 (glass 2).[80]

The AC calorimetry measurements confirmed previously reported [63, 81] glass transition of liquid 1 at $T_g^1 = 205$ K. However, a second glass transition temperature, $T_g^2 = 225$ K, was

detected for the glacial phase formed at 220 K. The existence of two glass transition temperatures for a single-component system further confirmed the existence of an LLT.

The polarisation microscopy revealed that the glacial phase domains formed via the (NG)-type LLT exhibited optical anisotropy due to the presence of micro- or nanocrystallites embedded in the amorphous glacial phase. Below T_{SD} no birefringence was detected in the system throughout the entire (SD)-type transformation. These observations were further investigated by employing time-resolved polarised and depolarised light scattering. The results led to the hypothesis that the LLT and nanocrystals formation occur at the same time, possibly the latter being induced by the former due to the interfacial energy barrier between crystals and liquid 2 being much lower than the energy barrier between crystals and liquid 1.[82] This conclusion was additionally supported by the experiments performed at elevated pressures, which showed that in such conditions crystallisation was suppressed whilst the LLT was observed.[83]

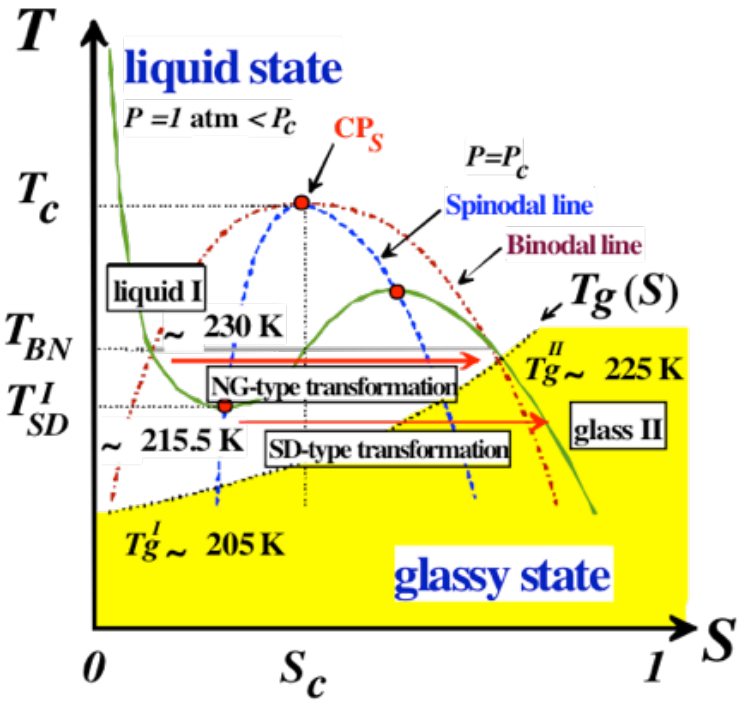

Figure 2. *Schematic LLT phase diagram of TPP in a T-S plane; S is a nonconserved order parameter governing LLT.*[84]

The overall conclusion of the studies carried out by Tanaka and co-workers was that the glacial phase was formed as a result of an LLT, which exhibited two different types of kinetic behaviour depending on the temperature. The glacial phase formed below T_{SD} was a homogeneous glassy state of liquid 2 (pure glass 2), while that formed above T_{SD} was a mixture of glass 2 and microcrystallites.[80]

1.1.3 Butanol

In 2003, following the discovery of the second apparently amorphous phase and an LLT in TPP, a similar phenomenon was reported by Bol'shakov and Dzhonson for another molecular liquid, namely *n*-butanol.[85] They observed that when supercooled and annealed in the temperature range 130-160 K, *n*-butanol (T_m = 183.4 K) transformed into a white or transparent solid phase, which differed in properties from the known crystal and glass phases (T_g = 118 K). The conclusion that the new phase was amorphous was based on the experimental observations that *tert*-butyl chloride, diphenylamine and oxygen dissolved in liquid *n*-butanol prior to the transformation, were not expelled, as it would be expected from a crystalline state. This new phase was stable at low temperatures and became liquid when heated to 170 K. Further investigations of the properties of the new phase (called by some glass 2 or, similarly to TPP, the glacial phase) by oxidation kinetics revealed that its diffusional properties differed significantly from glass 1 obtained by rapid cooling of the liquid *n*-butanol (liquid 1) below T_g.[86]

Kurita and Tanaka, who proposed the scenario of the existence of an LLT in TPP, predicted a similar scenario for *n*-butanol. Using phase-contrast microscopy, they identified two types of transition patterns, strongly suggestive of an LLT. When *n*-butanol was quenched to 120 K, "darker" droplets of the new phase (liquid 2) were observed nucleating and gradually growing in the supercooled liquid 1. The appearance of these droplets indicated a higher refractive index and therefore higher density of this new phase in relation to liquid 1. The droplets of liquid 2 grew and collided until full transformation was achieved. As it was the case with TPP, Tanaka and co-workers used digital image analysis for quantitative analysis. The intensity distribution function, proportional to the density distribution, was calculated. The presence of two peaks, with one of them decreasing (liquid 1) and the other increasing (liquid 2) in amplitude, implied the coexistence of two phases. The linear growth of the droplets with the annealing time

strongly suggested that the observed phenomenon was a nucleation and growth-type (NG) LLT.[29]

When *n*-butanol was annealed at 115 K, a different pattern evolution was observed. The "darker" droplets of liquid 2 appeared in liquid 1 with spatial correlation and the contrast between liquid 1 and liquid 2 gradually increased over time. The intensity distribution function behaved distinctly different to the one observed at higher temperature. Only one peak was observed throughout the whole transformation. This peak (initially corresponding to liquid 1) gradually broadened as a result of the increasing contrast between both liquids, resembling time evolution of the intensity distribution function characteristic of spinodal decomposition of a binary mixture. The position of this single peak gradually shifted to the left as the transformation progressed. Further analysis revealed that the spatial correlation in the density distribution at this temperature was consistent with the scenario that the observed phenomenon was a spinodal-decomposition-type (SD) LLT.[29]

Calorimetric measurements, carried out by Tanaka and co-workers, to substantiate the conclusions of the existence of the second liquid phase and an LLT in *n*-butanol, concluded with the findings that liquid 1 transformed to the glassy state of liquid 2, with liquid 2 having its own glass transition temperature at 133 K. As TPP and *n*-butanol differ significantly in the molecular structure, and yet their behaviour was strikingly similar, it was suggested that an LLT might be a general property all molecular liquids.[29]

Hédoux and co-workers used Raman spectroscopy and X-ray diffraction to study the isothermal transformation of *n*-butanol at 120 K with the aim to probe its local and long-range order. Their sample preparation protocol was different to that utilised by Tanaka as the samples were cooled from room temperature to 100 K (below T_g) and then the temperature was slowly increased to 120 K, rather than quenched directly from room temperature to the selected annealing temperature. The overall conclusion of their studies was that *n*-butanol transformed into a mixed state composed of micro- or submicrocrystallites and supercooled (non-transformed) liquid. The estimated degree of crystallinity was about 70% at 120 K. They argued that the observed phenomenon, just above T_g, was associated with the devitrification process driven by the formation of new associations via hydrogen bonding and was possibly frustrated due to a very high nucleation rate and very low molecular mobility in the deeply supercooled state, preventing rearrangement of molecules.[87-89]

Hassaine *et al.* reported that the thermal behaviour of the new (glassy) phase of *n*-butanol was different to that of the stable crystal and the glass, but it was, however, close to a strongly defective crystal. They detected no traces of the second glass transition and agreed with the conclusions of Hédoux and co-workers that the new phase was a mixture of submicrocrystallites embedded in a disordered (solid or liquid) matrix formed as a result of an aborted crystallisation. This was further supported by Brillouin-scattering measurements showing peaks corresponding to the stable crystal to be present in the glacial phase, increasing in intensity and displaying improved definition as the temperature of annealing was increased.[90]

Ramos and co-workers addressed the question of the nature of the apparently amorphous glacial phase by carrying out more extensive X-ray studies in the temperature range from 96.5 K (glass 1) to 180 K (stable crystal 1). They reported that the spectra of the stable crystal phase and the crystal obtained from the glacial phase were identical and described the glacial phase as "some kind of disordered, not-well grown crystal".[91] This conclusion was further supported by heat capacity and thermal conductivity measurements which showed that the behaviour of the glacial phase in *n*-butanol was not as expected from an amorphous solid but rather a very defective crystal.[92]

As it is in the case of TPP, despite extensive studies utilising various experimental techniques there is no consensus as to the nature and origin of the glacial phase in *n*-butanol. And similarly, two main scenarios used to explain the phenomena observed in deeply supercooled *n*-butanol are the existence of an LLT or an aborted crystallisation leading to the formation of microcrystals.

1.2 Order Parameter

The order parameter, briefly mentioned in the previous sections and Figure 2, is a parameter chosen to best represent physical changes occurring during a phase transition. In case of the most common phase transitions, *i.e.*, solid-liquid and liquid-gas, the order parameter is known to be density, which maximises the efficiency of the molecular packing. In ferromagnetic systems undergoing a phase transition it is the net magnetisation. Isotropic to nematic liquid-crystalline (LC) transitions are characterised by the degree of orientational ordering. In such cases, the order parameter S describes the average orientation angle θ of molecules in an LC at one time with respect to

the preferred direction in which the molecular axis of the bulk tends to point and is defined as[93]

$$S = \left\langle \frac{3}{2}\cos^2\theta - \frac{1}{2} \right\rangle \quad (1)$$

Perfect order results in $S = 1$, while $S = 0$ means that there is no orientational order. Figure 3 shows the typical variation of S with temperature for so-called thermotropic LCs in which the degree of orientational and positional order depends on temperature. Typical values of S are between 0.8 and 0.3 and this value decreases with increasing temperature and entropy. At the clearing temperature T_c, the system becomes an isotropic liquid.

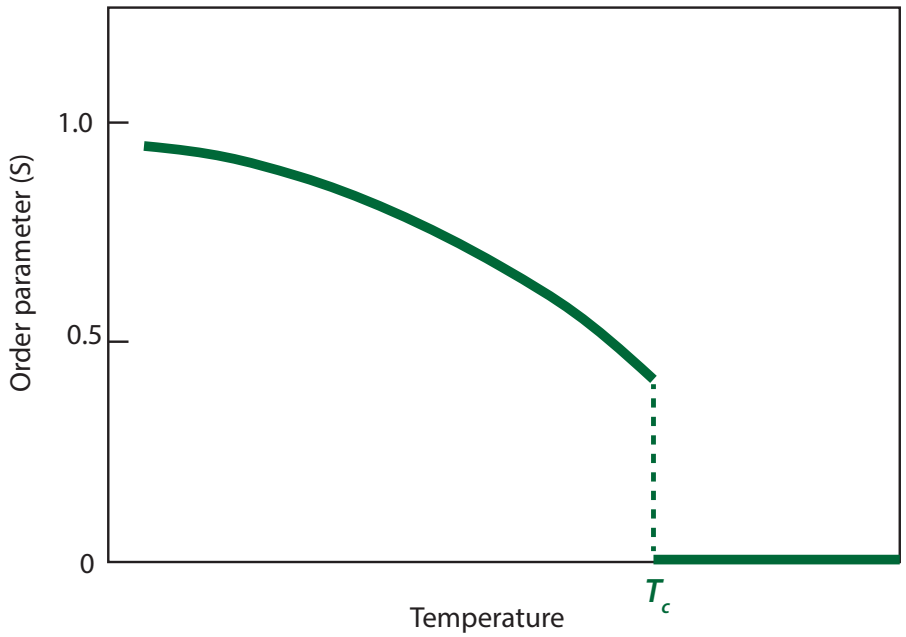

Figure 3. *Temperature dependence of the order parameter characterising liquid-crystalline phases. T_c is the clearing temperature at which transition to (isotropic) liquid occurs.*[94]

In the case of LLTs, transitions between two disordered states, up to date there has been no consensus to what the most suitable order parameter is. Tanaka and co-workers postulated that, despite a common belief that a liquid can be described using only density, at least two order parameters are needed to understand and describe the physical properties of the liquid state. Two-order-parameter model was developed to explain water anomalies, formation of glasses and LLTs (both from kinetics and

thermodynamics point of view). The model proposed that most liquids could be physically described as consisting of unique, locally favoured structures (short-range bond order) cooperatively excited in a sea of disordered background structures (normal-liquid). This locally favoured structure (LFS) can be identified as a minimum structural unit (volume or symmetry element). The number of the LFSs increases with decreasing temperature as they are (in the ground state) energetically more favourable than normal-liquid structures (in the excited state) (Figure 4). The assumption is that the energy and the lifetime between LFSs and normal-liquid structures are distinctly different, indicating whether the LFS is a symmetry element or not. This description shows that additional order parameter, named bond order parameter *S*, is required to satisfactorily describe a liquid state and the LLT. *S* represents the fraction or number density of LFSs.[3, 95, 96]

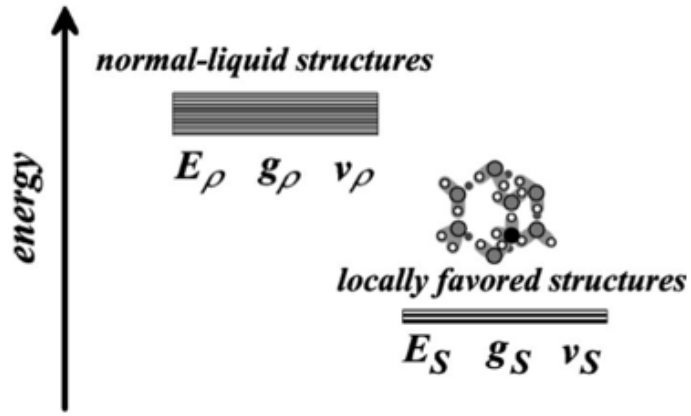

Figure 4. *Schematic illustration showing the energy levels of normal-liquid and locally favoured structures and a proposed locally favoured structure for water. Note that* $E_S < E_\rho$, $\upsilon_S > \upsilon_\rho$ *and* $g_S \ll g_\rho$ *- energy, specific volume and degeneracy respectively. The subscript S represents parameters of locally favoured structures, whilst ρ corresponds to normal-liquid structures.*[3]

Up to date, the coupling of the bond order parameter and density is the only alternative to the classical description of the liquid state using only its density. However it is still unclear what the bond order parameter actually represents on the molecular level and how to measure it.

1.3 Nucleation

Crystallisation lies behind many natural phenomena and plays a crucial role in various industrial processes, such as synthesis, purification and separation of drugs, chemicals and food.

For crystallisation to occur a solution must be supersaturated, *i.e.* the solute's concentration must exceed its thermodynamic solubility limit. Nucleation, a first-order transition during which solid particles are formed from atoms, ions or macromolecules, is an essential part of every crystallisation process. In general, nucleation can be divided into primary (when there is no crystalline substance in the supersaturated solution) or secondary (when a crystalline substance is present in the supersaturated solution). The primary nucleation can be further divided into homogeneous and heterogeneous. Foreign particles, present in the supersaturated solution, induce heterogeneous nucleation, whilst homogeneous nucleation occurs in their absence.

The importance of crystallisation in many fields of science and technology led to the formulation of well-established theories for nucleation and crystal growth.[97]

Crystal nucleation in melts or solutions is typically described by so-called classical nucleation theory (CNT). This theory, formulated at the end of the 19th century by Gibbs, is based on the competition between the free energy of solidification and the free energy due to the presence of the interface.[98] The latter results in a barrier to crystallisation and hence supersaturation and a metastable nonequilibrium state. Thermodynamic fluctuations then lead to pre-nucleation sites, the majority of which will redissolve.[99] Occasionally, a nucleus will grow big enough to overcome the barrier (a *critical nucleus*) and continue to grow. Only at considerable supersaturation will the energy barrier disappear, at which point homogeneous nucleation will occur (Figure 5). As a result, crystal nucleation is generally a rare process that is difficult to study either experimentally or even through computer simulation.

The total free energy ΔG required for the formation of a spherical critical nucleus with radius r:

$$\Delta G = -\frac{4}{3}\pi r^3 n_s \delta\mu + 4\pi r^2 \gamma \qquad (2)$$

where n_S is the number density of particles in the solid, $\delta\mu$ is the difference between chemical potential of the liquid and the solid, and γ is the liquid-solid interfacial tension. The critical size (*i.e.* the minimum size) of the stable nucleus r_C and the critical free energy of the system ΔG_C (see Figure 5) are given by

$$r_C = 2\gamma / (n_S \delta\mu) \tag{3}$$

$$\Delta G_C = \frac{16\pi\gamma^3}{3(n_S\delta\mu)^2} \tag{4}$$

Nuclei with a radius smaller than r_C will redissolve and the ones larger than r_C will continue to grow as it reduces their free energy. The nucleation frequency I, equal to the number of nuclei per volume, is given as

$$I = \frac{k}{\tau_t}\exp\left[-\Delta G_C / k_B T\right] \tag{5}$$

where is k a constant, k_B is Boltzmann's constant and T is temperature. τ_t, the characteristic time of material transport which controls crystallisation, governs the kinetics of nucleation.[100]

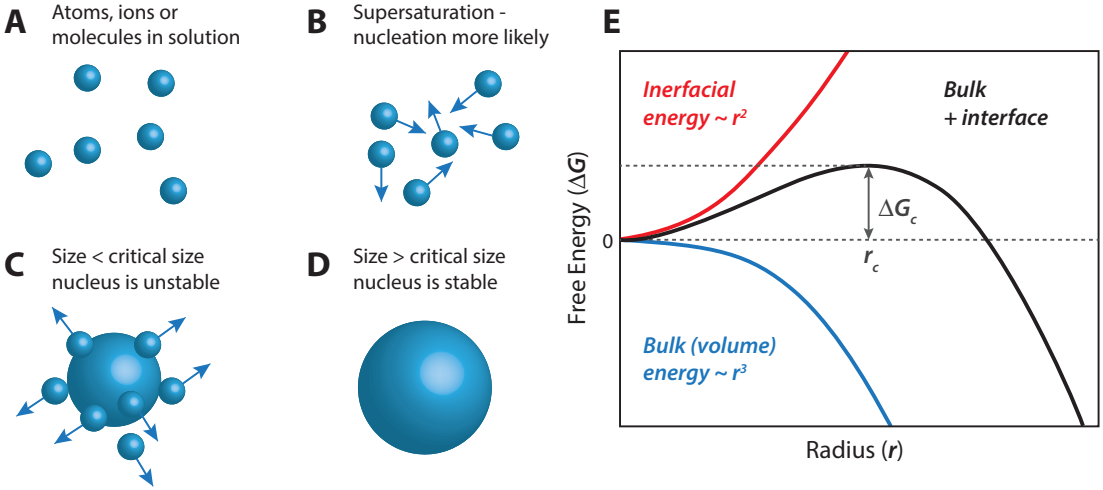

Figure 5. *Classical nucleation theory – simplified illustration of the concepts. Increasing supersaturation makes it more likely for random density fluctuations to occur, ions or molecules (**A**) to cluster (**B**). If the size of the formed cluster is smaller than the critical nucleus size, the cluster is unstable and will redissolve (**C**). However, if the size of the cluster is larger the critical nucleus size, nucleation occurs (**D**).*[101]

There are a number of assumptions underlying the CNT: the nuclei are spherical (or constant shape), there is only one interfacial energy for the entire forming nuclei and finally - the nucleation is entirely homogeneous.[101] Whilst the CNT allows the estimation of the critical size of the nucleus and the nucleation frequency, it does not take into account that the nucleating phase may have a structure distinctly different from the final product of crystallisation. This is crucial for understanding and controlling of the outcome of any crystallisation process in terms of its size, purity, morphology and structure.

The CNT describes the early stages of crystallisation by two main processes: nucleation of stable nuclei and their subsequent growth. However this point of view has been shown to be rather limiting and inadequate in many cases. More than a century ago Ostwald argued that a system in an unstable state does not necessarily transform directly into the most thermodynamically stable one. Such system could firstly transform into another intermediate state, accompanied by the smallest free energy loss, before the stable state is reached. Hence, the nucleated phase is not necessary the most thermodynamically stable one, but the one which free energy is closest to the disordered (liquid) phase. This so-called Ostwald's rule of stages suggests that the recognition and understanding of these intermediate metastable states is critical to the understanding of the path and thermodynamics of nucleation.[102] The difficulty is that such metastable states are typically too rare or short-lived to be observed.

Another concept, developed primarily within the field of bio mineralisation, proposed existence of small, thermodynamically stable pre-nucleation clusters (PNC) in the homogeneous region of the phase diagram. Recent work by Gebauer and others has shown that in some cases (such as the nucleation of carbonates from aqueous solution)[103-106] formed solute clusters may aggregate into amorphous clusters. The elimination of the interface and re-crystallisation within clusters may lead to formation of crystal nuclei.[103, 106-108] Such non-classical nucleation theories do not require a "critical nucleus". These theories appear to, but may not necessarily,[109] be counter to thermodynamic theory. Interestingly, a number of light scattering studies of solutions have shown anomalous clustering in solution suggesting that the effect might be more general.[110, 111]

1.4 Liquid Crystal Phases

In a crystal, the order is usually both positional and orientational. A liquid, on the other hand, is considered a dynamically changing phase with molecules undergoing random tumbling motion and constant re-arrangement. The term "liquid crystal" (also called a mesophase) indicates a state intermediate between the amorphous liquid and the ordered crystalline solid, characterised by some degree of long-range orientational order and sometimes one-, two- or even three-dimensional long-range translational or positional order (Figure 6). In a mesophase, the affinity for the molecules to spend more time in a certain position or to point in one direction is much less pronounced which is reflected in the latent heat values of crystal-LC transition, close in value to normal melting.[94] A typical LC molecule consists of two parts – the rigid central part called mesogen and the flexible side chains called spacer.[112] The elongated cigar-shaped molecules are in constant thermal motion but prefer parallel alignment due to the strong intermolecular interactions ($\pi-\pi$). Despite the fact that LCs combine the properties of amorphous isotropic liquids and ordered crystalline solids, they exhibit unique electro-optical properties, not observed in case of other solids and liquids. The orientational order of constituent anisotropic molecules controls the physical properties of the LC and can be monitored by weak electric or magnetic fields, effectively changing optical and mechanical properties of an LC. This switchability has broad practical applications in modern technologies such as displays and opto-electronic devices.[112] The predominant orientation of alignment, called the "director", is a unit vector *n* that characterises the long-order of constituent molecules (Figure 6).[94]

There are a great variety of LC phases varying in their structure and physical properties. In general, they are classified into two major classes – thermotropic and lyotropic. Thermotropic LCs are formed by the substances which transit to the LC state with increasing temperature via the following path of reversible first-order phase transitions: solid-LC-isotropic liquid. Three examples of thermotropic LCs are shown in Figure 6. In the least ordered, so-called nematic phase, the molecules are still able to move but their orientation remains constant. Smectic phase exhibits both orientational and positional order. As the molecules are arranged in layers, their movement is restricted inside them. Cholesteric phase is the nematic phase in which molecules are arranged at a slight angle to one another resulting in a natural twist between layers. On the other hand, lyotropic LC phase appear when LC-forming substances are dissolved, within

certain concentration range, in water or other solvents. Lyotropic LCs play a great role in biology (*e.g.* in metabolic processes of living organisms) and are found in more materials than thermotropic LCs.[113]

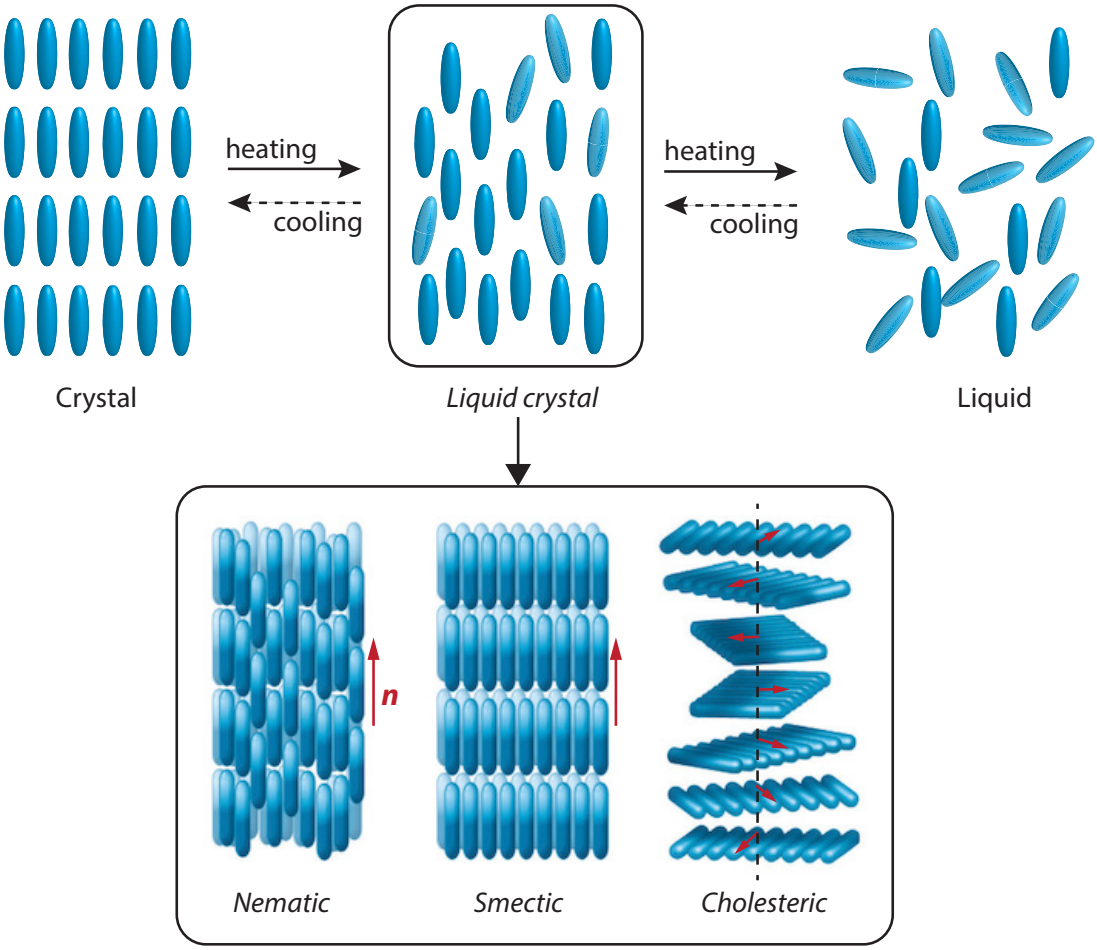

Figure 6. *Illustration of relationship between liquid crystalline phase with liquid and crystalline solid phases (**top**) and structure diagrams of three types of liquid crystalline phases (**bottom**).[112, 114] The red arrows indicate the long-order of molecules represented by the director n.*

2

Experimental

This chapter introduces the imaging and spectroscopic techniques used to study phase transitions and mesophases, which are the subject of this work. It also provides full experimental details, including materials used, configurations of experimental set-ups, and sample preparation methods.

2.1 Dark Field Imaging

2.1.1 Introduction

The observation of very small objects and many fine details against a bright background is, in most cases, very difficult, if not impossible. Dark field imaging is a technique, which enables such observations through formation of the image exclusively from scattered light.[115]

In practice, dark field imaging can be achieved by placing a so-called 'patch stop' (an opaque disc) onto a standard bright-field condenser or using special dark field condensers, which concentrate light by reflection. The patch stop blocks out the central portion of the illumination and ensures that only light deviated by the sample enters the objective and forms the image (Figure 7). The contrast enhancement comes from

elimination of the background intensity and the resulting image is that of the small objects in negative contrast, *i.e.*, they appear bright against a dark background.[115-117]

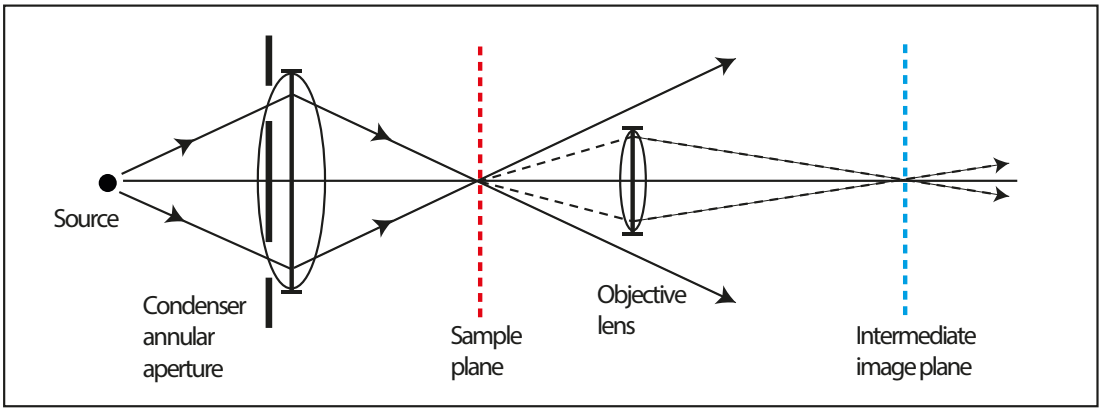

Figure 7. *Image formation in dark field imaging.*

2.1.2 Experimental Set-up

The experimental set-up for dark field imaging is shown in Figure 8. The set-up enabled experiments to be performed at cryogenic temperatures by using an Optistat DN liquid nitrogen (LN_2) optical spectroscopy cryostat (Oxford Instruments) offering a temperature range between -196 and 27° C and optical access to the sample space via up to five windows.

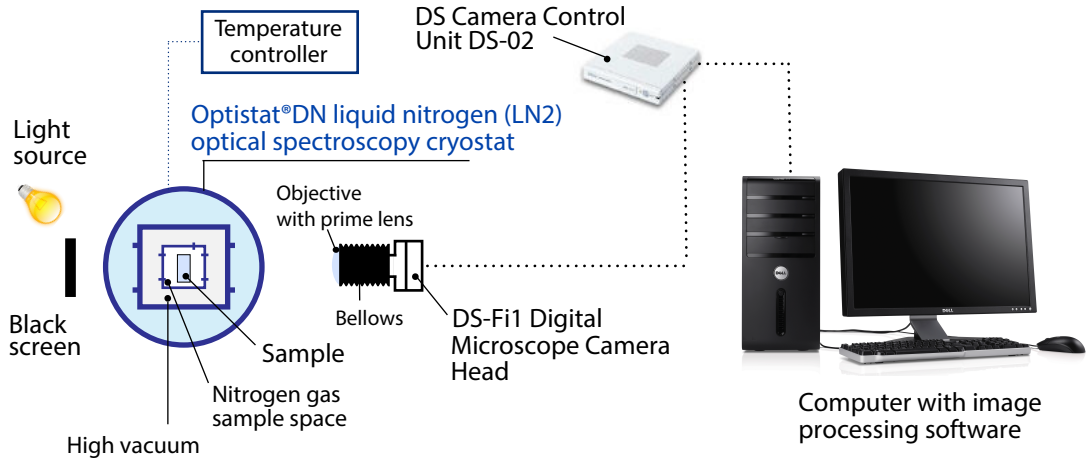

Figure 8. *Experimental set-up for dark field imaging at variable temperatures.*

Dark field imaging was performed using a visible light source placed behind a black screen acting as a patch stop. Images and movies were recorded using a 5-megapixel Nikon DS-Fi1 camera interfaced to a computer through a USB port. It was integrated via

Nikon Digital Sight DS-U2 controller with Nikon's NIS-Elements Documentation software that allowed image acquisition.

Magnification offered by this experimental set up did not allow accurate determination of the size of the observed crystalline structures.

2.1.3 Sample Preparation

This technique was used to study the mixture of water in *trans*-1,2-dichloroethylene described in Chapter 3. All samples were degassed by freeze-thaw cycling under vacuum and distilled directly into a 2mm-deep by 10mm-wide quartz rectangular cuvette with a long glass tube attached. The end of this tube was connected to a vacuum pump via series of PTFE tubes, connectors and valves. The whole system was sealed enabling evacuation of atmospheric gases and preventing their reabsorption. The experiments were performed at the vapour pressure.

2.2 Bright Field Microscopy

2.2.1 Introduction

Bright field microscopy is the most basic transmitted light microscopy technique. Bright field illumination (also called Köhler illumination) is designed to provide an even illumination of a large area using a small light source. This technique is suitable for samples with relatively high contrast, coloured or stained.[117]

To explain how it works, let us consider two sets of light rays, which coincide with each other whilst performing different roles. The first set - the illuminating rays - contains successive images of the lamp filament. It is first focused at the condenser aperture plane and then at the so-called back focal plane, inside the objective. In between these two focus points these light rays provide a desired wide and even illumination for the specimen. Finally, the eye lens projects them onto the retina (Figure 9).[117, 118]

The second set consists of so called image-forming rays and it carries successive images of the specimen. Light rays passing through a specimen (evenly illuminated by parallel illuminating rays) are focused at the primary image plane by the objective (Figure 9). On this plane an image is magnified but rotated by 180°. The image is rotated

to the correct position by the eyepiece lenses and it is formed at a small distance from the top lens of the eyepiece.

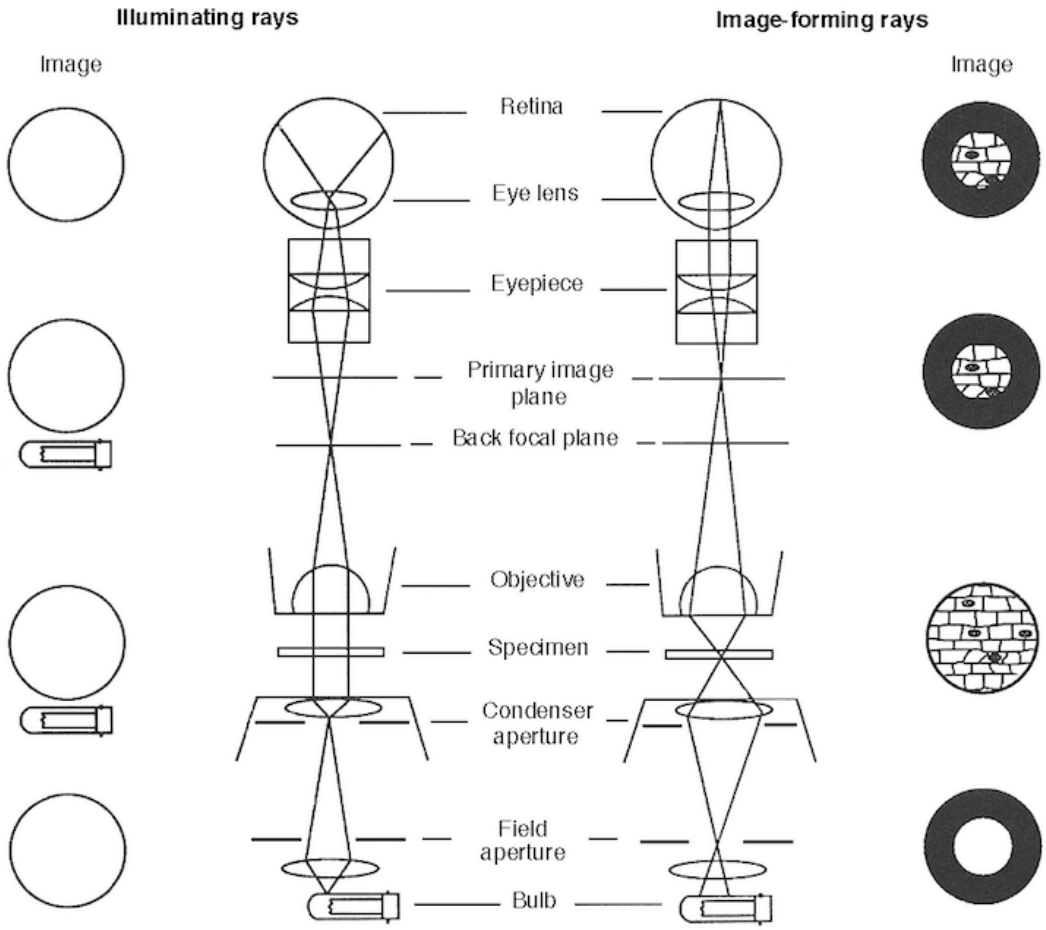

Figure 9. *Bright field illumination diagram showing illuminating and image-forming rays with images formed at particular planes.* [117]

The total magnification achieved is the product of the magnification of two lens systems: the objective and the eyepiece.

2.2.2 Experimental Set-up

The experimental set-up for bright field microscopy is shown in Figure 10. It consisted of a Nikon Eclipse 50i microscope with an attached 5-megapixel DS-Fi1 camera and a heating and freezing microscope stage (Linkam) replacing a standard microscope stage.

A Nikon Digital Sight DS-U2 controller interfaced the camera to a PC through a USB port. It was integrated with Nikon's NIS-Elements Documentation software that allowed image acquisition from the microscope.

A sample was placed in the sample chamber of a heating and freezing microscope stage (Linkam). A T95 system controller (including Linksys 32 system control software) communicated with an LNP95 cooling pump and regulated the temperature of the sample by adjusting the flow of liquid nitrogen. The rate at which the sample could be cooled was between 0.01 and 100° C/min and the heating rate was up to 150° C/min. The temperature range could be controlled between -196° C and 300° C, with 0.1° C accuracy. The dry nitrogen exhausted from the unit was used to purge the sample chamber and keep the tubing flexible.

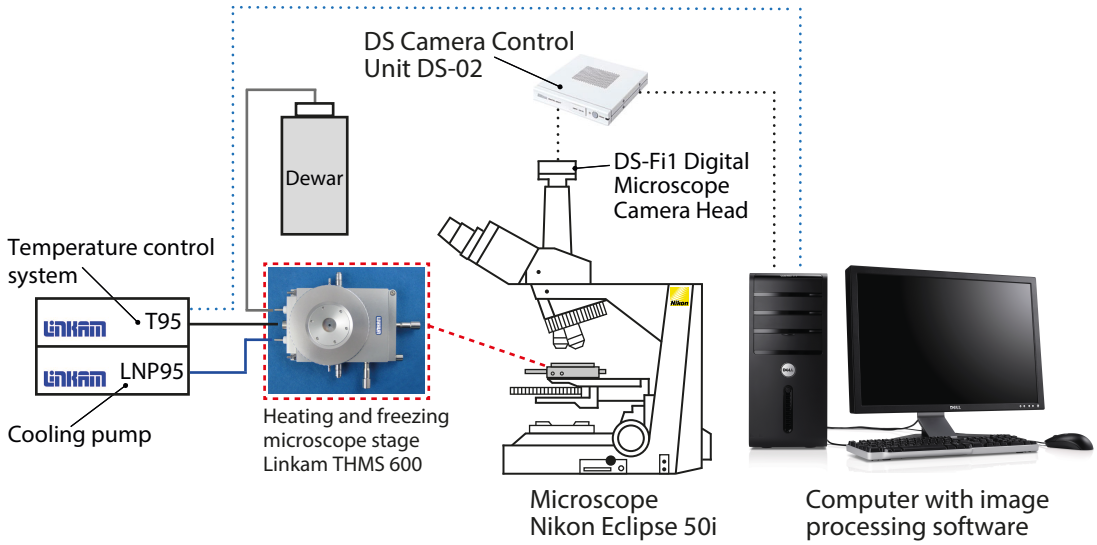

Figure 10. *Experimental set-up for bright field microscopy at variable temperatures (Nikon).*

2.3 Phase Contrast Microscopy

2.3.1 Introduction

The aim of phase contrast microscopy is to produce a visible image of structures in samples or specimens, which are invisible to the eye under standard bright field illumination.

A phase contrast microscope is designed in such a way that it enables the segregation of the surround (undiffracted) and diffracted light emerging from the sample and projects them onto different locations in the rear focal plane of the objective (Figure 11). Additionally, to generate contrast visible to our eyes, the amplitude of the surround light is reduced and the phase is either advanced or retarded by about a quarter wavelength (*λ/4)*.

To achieve this a bright field microscope is equipped with two additional specialised accessories - a condenser annulus and a phase contrast objective featuring a phase plate positioned either in or near its rear focal plane.

A phase annulus (a ring-shaped hole), placed in a condenser, illuminates the sample with defocused, parallel light. The light, which goes through a sample, is retarded by about *λ/4*. The light passing through the sample and the thick portion of the phase plate (outside the phase ring) is given an additional phase difference of $\lambda / 4$:

$$\Phi = x + \lambda / 4 + \lambda / 4 = x + \lambda / 2 \qquad (6)$$

where *Φ* is the phase difference, *x* is the retardation given to the light ray by the thinner portion of the plate, and *λ* is the wavelength. Therefore there is a *λ/2* phase difference between the surround ray (*Φ = x*) and the diffracted ray and it results in destructive interference. On the resultant image, the sample looks darker than the background. Obtained contrast differs across the sample depending on the phase retardation and creates detail in the image. The intensity of the image is proportional to the refractive index contrast and therefore to the density contrast.[116, 117]

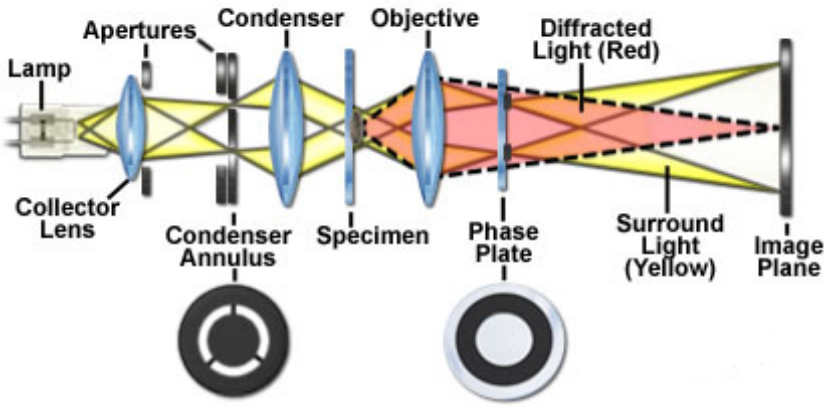

Figure 11. *Phase contrast microscope optical train.*[119]

2.3.2 Experimental Set-ups

Two different experimental set-ups were used to record phase contrast microscopy images presented in this work and it is specified in the particular chapters which one was used to obtain the results.

The first experimental set-up for phase contrast microscopy is described in detail in Section 2.2.2 and is shown in Figure 10.

The second experimental set-up used to record phase contrast microscopy images is described in Section 2.6.2.

2.4 Polarised Light Microscopy

2.4.1 Introduction

The polarised light microscopy is primarily used to detect and measure birefringence - the variation of sample's refractive index with the polarisation and propagation direction of light. This technique enables us to determine the sign and type of birefringence and locate the optical axes of birefringent structures. Due to the fact that anisotropic effects reveal the presence of regularity in the chemical bond orientations, the polarised light microscopy can be used to infer the nature of structures at dimensions not accessible by optical microscopy due to its resolution limits.

At the early stages of development of this technique, only samples with a high degree of anisotropy were examined, however nowadays it is possible to perform high-resolution measurements of low-level birefringence.

In order to perform polarised light observations, the microscope must be equipped with two polarisers. The first one is positioned in the optical pathway before the sample and the second one - called an analyser - between the objective rear aperture and the camera port.

In polarised light microscopy, image contrast comes from the interaction of plane-polarised light with a birefringent (or doubly-refracting) sample, the result of which are two wave components polarised in perpendicular to each other's planes. These components - called the ordinary and the extraordinary wavefronts - travel at different speeds depending on the propagation direction through the sample. On exiting the sample, the components become out of phase. The purpose of the analyser is to recombine them with constructive and destructive interference as shown in Figure 12.[115-117]

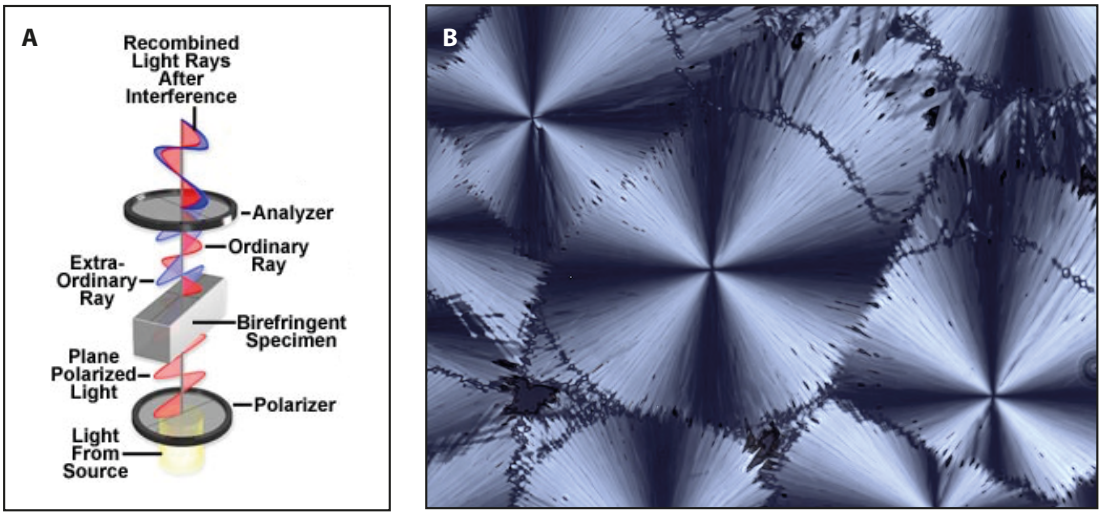

Figure 12. *(**A**) Polarised light microscope optical train.[120] (**B**) Triphenyl phosphite crystals under polarised light. The appearance of 'Maltese crosses' is a result of their birefringence.*

2.4.2 Experimental Set-up

The experimental set-up used to record simple polarisation microscopy images presented in this work is described in Section 2.2.2. The only additional accessory required to obtain polarisation microscopy images was a polariser, which was positioned in the light path between the light source and the condenser. This polariser could be manually rotated

through 360 degrees. The second in-built polariser (analyser), located above the objective, could be inserted into or removed from the light path but it could not be rotated.

2.5 Confocal Raman Microscopy

2.5.1 Introduction

Confocal Raman microscopy combines two very powerful analytical techniques: confocal microscopy and Raman spectroscopy.

This technique enables us to collect the signal from a single point on a sample thanks to a special optical design shown schematically in Figure 13. The single point focus on a sample is achieved by placing a pinhole aperture in front of the laser, which is then refocused by the microscope objective. Another pinhole aperture, placed between the microscope objective and the image plane, acts as a spatial filter eliminating any residual scattering arising from out-of-focus points on the sample. The signal collected from the sample is dispersed into a spectrum by a spectrometer and detected by a CCD detector.

The spectral information, obtained through Raman spectroscopy, provides a molecular fingerprint by probing the vibrational energy levels within a molecule. It is based on the inelastic scattering of monochromatic light, occurring upon interaction of the electromagnetic radiation with vibrational and/or rotational motions of molecules. The frequency of the scattered light is shifted in respect to the original monochromatic frequency, which is known as the Raman effect. This frequency shift (Raman shift) is characteristic of vibrational and rotational energies of the specific molecular bonds. Therefore this technique provides information about the chemical composition of the chosen spot in a sample.[121, 122]

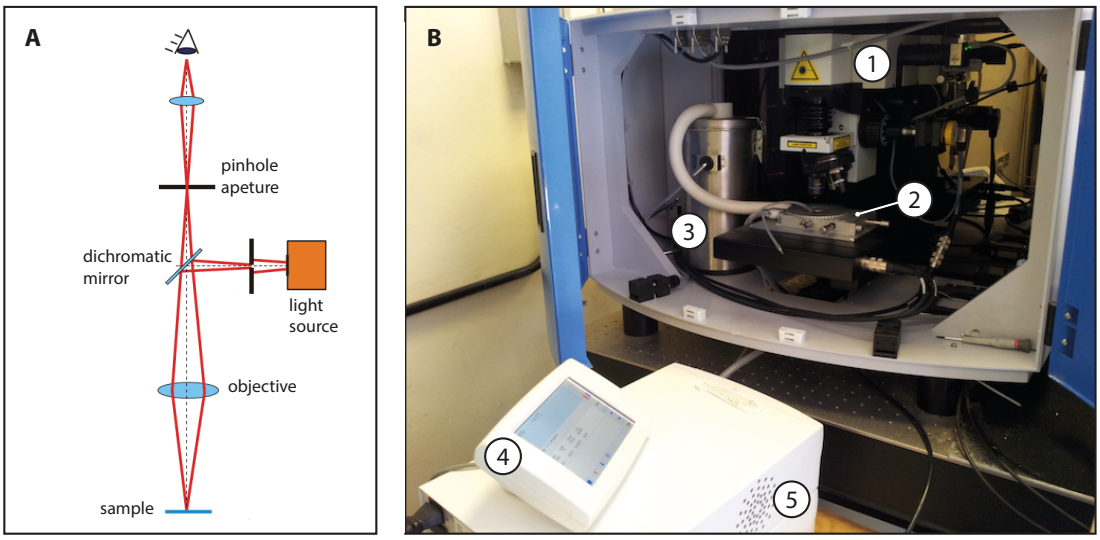

Figure 13. *(**A**) Schematic of confocal Raman microscopy system.[121] (**B**) Confocal Raman microscopy experimental set-up (1 - Horiba LabRAM HR confocal microscope, 2 - Linkam stage, 3 - Dewar, 4 - LinkPad controller, 5 - Linkam LNP95 cooling system).*

2.5.2 Experimental Set-up

The experimental set-up for confocal Raman microscopy is shown in Figure 13 and Figure 14. The integral part of this set-up is a Horiba LabRAM HR confocal microscope system. The excitation source was a 532 nm diode-pumped solid-state (DPSS) laser. The measured laser power at the sample stage was 28 mW. A 50 µm diameter aperture and 50× long-working-distance objective were used to record the Raman spectra.

All samples were placed in the heating and freezing microscope stage (Linkam) and the sample loading protocols are described in Section 2.6.5. The operating system of the temperature control system (LNP95, Linkam) was accessed through the touch screen display called LinkPad.

The Raman microscopy experiments carried out on water crystals, phase-separated from a mixture of water and *trans*-1,2-dichloroethylene (*trans*-DCE), required *trans*-DCE to be removed prior to measurements. This was achieved by controlled vacuum evaporation at 233 K.

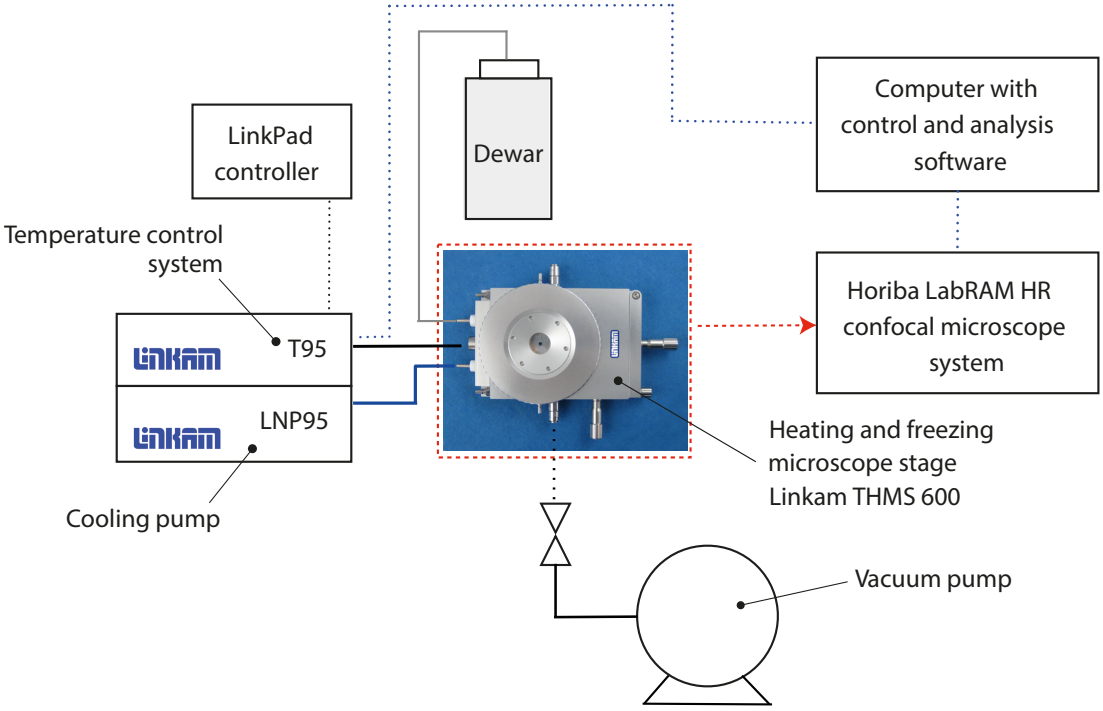

Figure 14. *Experimental set-up for confocal Raman microscopy at variable temperatures. The vacuum pump was used only in experiments required the removal of liquid trans-1,2-dichloroethylene.*

2.5.3 Data Analysis

Raman scattering intensity and the linewidth (FWHM) were analysed by fitting a Gaussian function to the chosen peaks using IGOR Pro 6.21.

2.6 Fluorescence Lifetime Imaging Microscopy

2.6.1 Introduction

Fluorescence occurs when a fluorophore (or a fluorescent dye) is excited by light of appropriate wavelength. The light emitted as a result is usually characterised by a longer wavelength than the excitation wavelength. The fluorescence light produces a characteristic spectrum and it is emitted with a characteristic time constant known as the fluorescence lifetime τ (or fluorescence decay time):[123]

$$\tau = \frac{1}{k_r + k_{nr}} \tag{7}$$

where k_r and k_{nr} are the radiative and non-radiative rate constant respectively. The fluorescence lifetime of a fluorophore, within reasonable limits, is not affected by its concentration but it is highly dependent on its molecular environment and hence can be used to probe and investigate molecular effects. Environmental properties and factors, which can influence the fluorescence lifetime, include the local refractive index,[124] the local viscosity,[125-127] the solvent polarity,[128] pH,[123] ion concentrations, oxygen, binding to proteins and proximity to metal surfaces.[129] Therefore imaging the fluorescence lifetime allows mapping of this molecular information.[130]

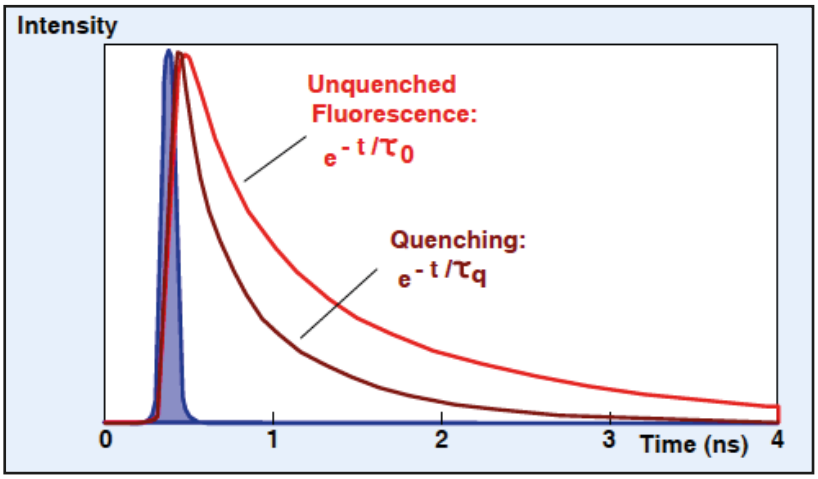

Figure 15. *Decay of the fluorescence (red) after excitation with a short light pulse (blue).*[129]

The radiative rate constant k_r is a function of the refractive index due to the polarisability of the medium surrounding the fluorescence probe. This relationship is known as the Strickler-Berg formula

$$k_r = \frac{1}{\tau_0} = 2.88 \times 10^{-9} n^2 \frac{\int I(\nu) d\nu}{\int I(\nu) \nu^{-3} d\nu} \int \frac{\varepsilon(\nu)}{\nu} d\nu \tag{8}$$

,

where τ_0 is the natural lifetime, I is the fluorescence emission, ε is the extinction coefficient, ν is the wavenumber, and n is the refractive index. It predicts that the florescence lifetime is inversely proportional to the square of the refractive index, $\tau_0 \propto n^{-2}$, and there is experimental evidence to support that.[130]

The technique used to perform fluorescence lifetime imaging (FLIM) is time-correlated single photon counting (TCSPC). Due to its high sensitivity, it enables recording of low-level light signals with picosecond resolution and extremely high precision.

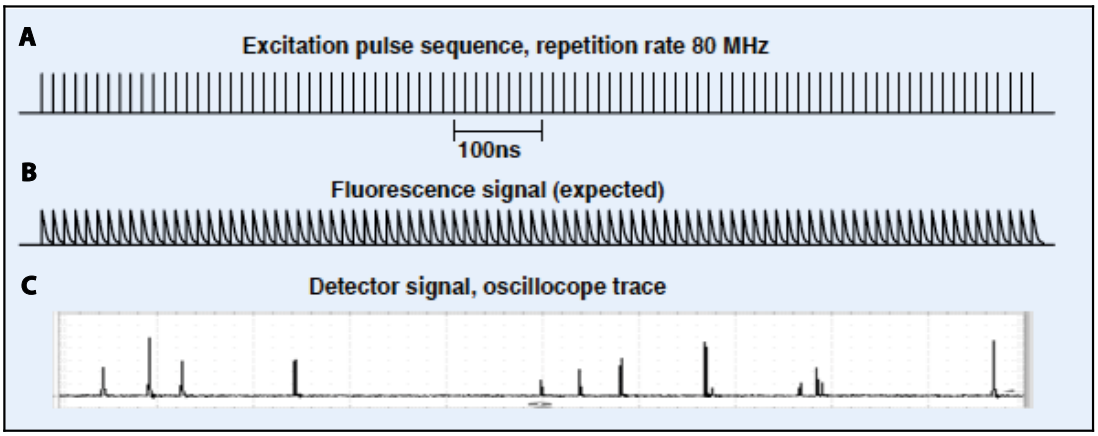

Figure 16. *Detector signal for fluorescence detection at a pulse repetition rate of 80 MHz (**A**) and the detection rate of 10^7 photons per second (**C**).*[129]

The classic TCSPC detects single photons of a periodic light signal, measures the detection times, and reconstructs the waveform from the individual time measurements. A sample excited by a laser pulsed with a repetition rate of 80 MHz, should in theory produce the fluorescence signal shown in Figure 16. However, the detector signal consists of only random pulses representing the detection of single photons of the fluorescence signal with the photon detection rate of about 10^7 s^{-1}. This order of magnitude represents the maximum possible detection capability of most photon counting detectors. Therefore it is necessary to consider the fluorescence signal as a photon distribution function created by measuring the arrival times of the photons after the excitation pulses and building up a histogram (Figure 17). The major limitation of the classic TCSPC is the fact that it is essentially one-dimensional. In practical terms that means that the scanner of a laser scanning microscope would have to stop and wait for a fluorescence decay curve to be recorded for each individual pixel.

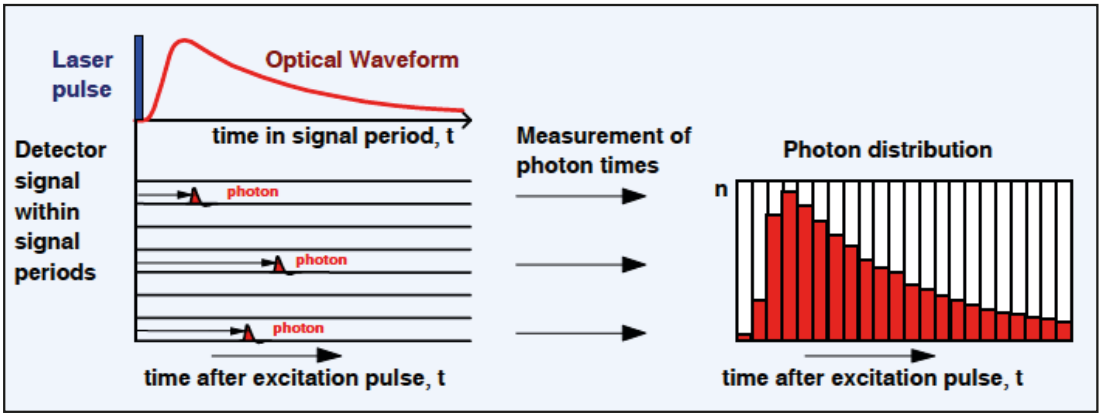

Figure 17. *Principle of time-correlated single photon counting (TCSPC).*[129]

In 1993 Becker & Hickl overcame this limitation by introducing a multi-dimensional TCSPC technique capable of characterising the photons not by one but by a number of parameters such as the wavelength, their location in a scan area, the time from the start of the experiment, or the time from a stimulation of the sample. An example of a resulting photon distribution is shown in Figure 18. The multi-dimensional TCSPC combined with a confocal laser scanning microscope delivers multi-wavelength FLIM with picosecond time resolution, close to ideal counting efficiency, and the multi-exponential decay profile resolving capability.

Figure 18 shows the basic architecture of a TCSPC FLIM device. The laser scanning microscope scans the sample and the resulting fluorescence is detected by a photon counting detector, which sends an electrical pulse into the TCSPC module for each detected photon. The TCSPC module also receives scan clock pulses from the microscope and determines, for each received pulse, the time in the fluorescence decay (t) and the location within the scanning area (x, y) building the photon distribution density over x, y and t.

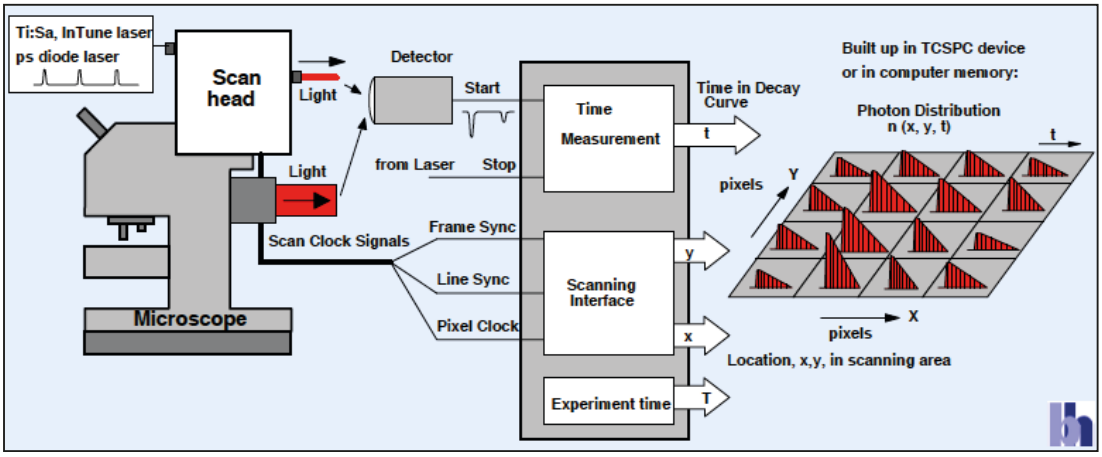

Figure 18. *Multi-dimensional TCSPC architecture for FLIM.*[129]

The result of such measurement is an array of data corresponding to the scan area with each pixel containing a fluorescence decay curve displayed as a pseudo-colour image. An example of a FLIM image is shown in Figure 19. The colour may represent any parameter of the decay profile, for example a lifetime of a decay component or its amplitude, whilst the brightness corresponds to the number of photons per pixel.[129]

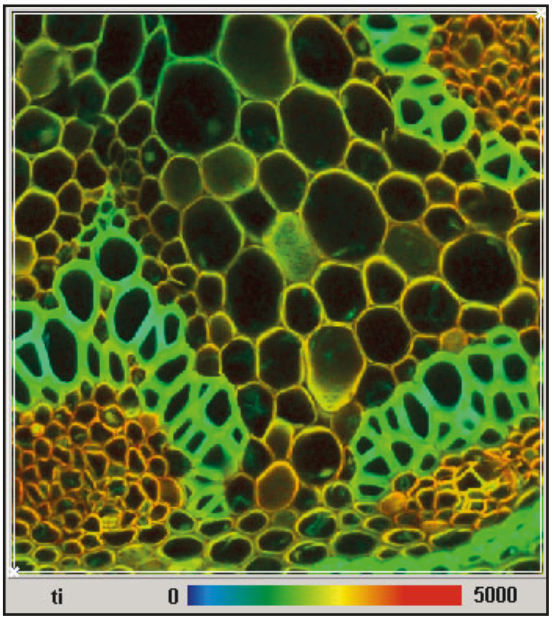

Figure 19. *Lifetime image of a Convallaria sample.*[129]

2.6.2 Experimental Set-ups

The fluorescence lifetime imaging microscopy set-up is shown in Figure 20. It consisted of a Zeiss LSM710 laser-scanning confocal microscope equipped with a 20× objective lens (NA = 0.4) providing a spatial resolution of 0.4 µm. This system, equipped with a number of CW laser sources ranging from 405 nm to 633 nm, was used for phase-contrast, fluorescence, polarisation, and differential interference contrast (DIC) microscopy. For FLIM measurements, the system used a 405-nm laser pulsed with a repetition rate of 20 MHz. A Becker & Hickl Simple-Tau detection system was used for time-correlated single photon counting (TCSPC). Areas of 212.1 x 212.1 µm^2 were mapped with a total acquisition time of ~30 s per frame. The emission wavelength of selected fluorophores, perylene and coumarin 153, was in the range 420-550 nm and 450-700 nm, respectively.

All samples were placed in the heating and freezing microscope stage (Linkam), replacing a standard microscope stage, and the sample loading protocols are described in Section 2.6.5. The operating system of the temperature control system (LNP95, Linkam) was accessed through the touch screen display called LinkPad.

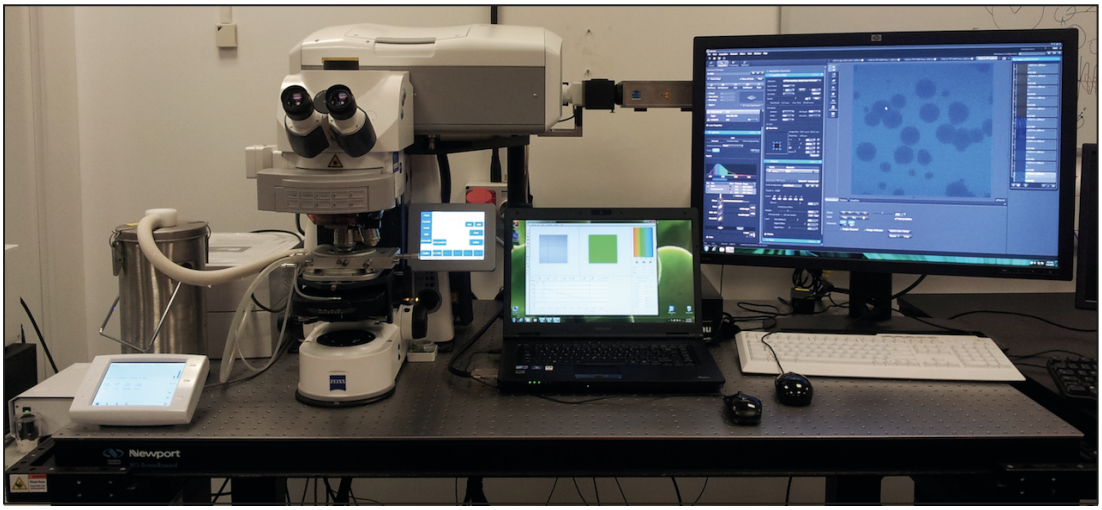

Figure 20. *The fluorescence lifetime imaging microscopy set-up (Zeiss / Becker & Hickl).*

FLIM images comprising 256 x 256 pixels were obtained at an approximate average photon flux of ~1 x 10^6 photons s^{-1}, and data were accumulated such that the total photon count was sufficient for fitting purposes (at approximately 3,500 photons per pixel followed by 9-pixel binning, which was applied as a sliding average). Fluorescence decay curves were collected to a total delay time of ~50 ns to ensure a good fit (X^2 ~ 1) and

an accurate determination of the background noise level in order to avoid underestimating the lifetime.

2.6.3 Data Analysis

Data analysis was performed using SPCImage software (Becker & Hickl). The accumulated fluorescence decay curves in each pixel of the scanned area were fitted with an appropriate model yielding a lifetime for each pixel in the image (Figure 21). In case of all results presented here, this model was a single exponential decay.

As the measured fluorescence lifetimes were much longer than the instrument response function (IRF) of the FLIM system, tail fitting was applied to all decay curves. The accuracy of the tail-fitting method was tested by performing a number of full fits (starting from the rise of the decay curve and including an experimentally obtained IRF). These fits yielded the same lifetime values within the signal-to-noise ratio.

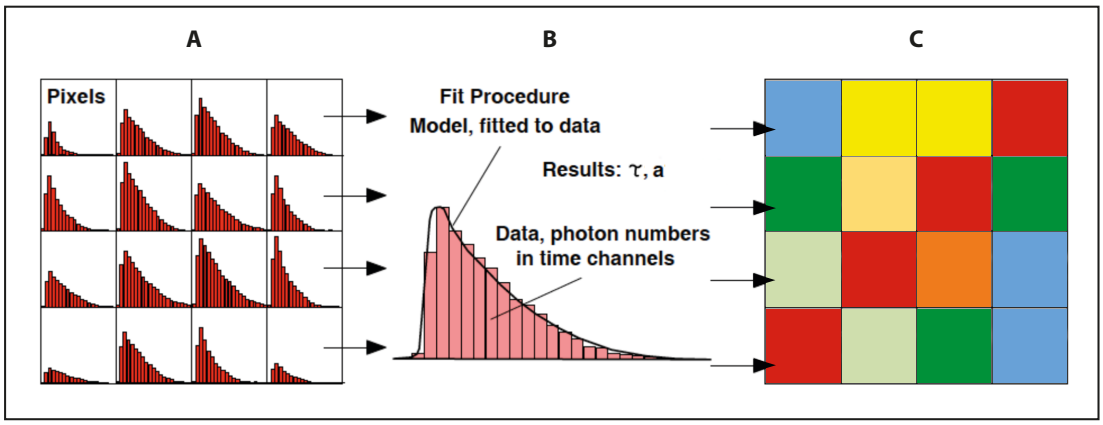

Figure 21. *Analysis of FLIM data. (**A**) Raw data - pixels containing decay curves. (**B**) Fit procedure delivers lifetimes and amplitudes for individual pixels. (**C**) Pixels contain results of fit procedure.*[129]

The FLIM data presented in the following chapters were obtained by tail fitting from 2 ns after the peak of the fluorescence decay curve (where the IRF has fallen to 1/1000$_{th}$ of its peak value) to about 30 ns where the fluorescence decay reached the noise level. It was confirmed that the 9-pixel binning procedure did not affect the lifetime distributions apart from a reduction in width by a factor of $\sqrt{9}$ as expected.

To obtain the peak value of the fluorescence lifetime distribution, it was fitted to one or two Gaussians using IGOR Pro 6.21 (Figure 22).

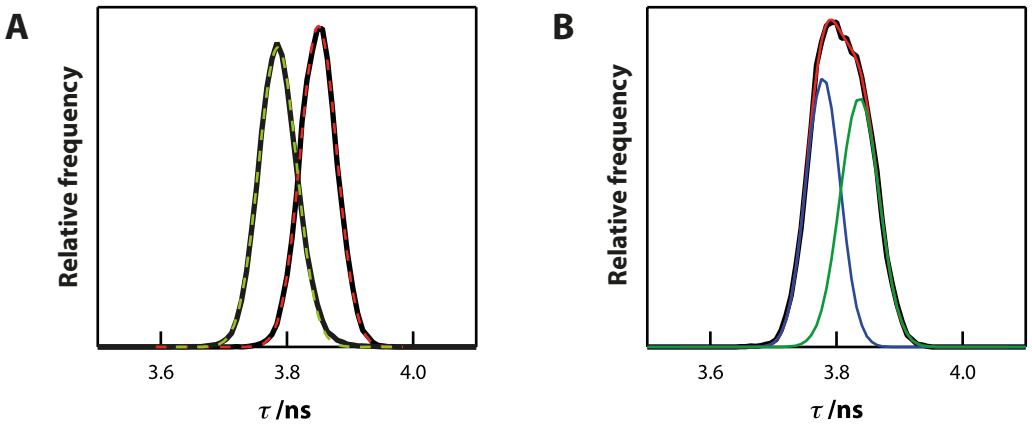

Figure 22. *Fluorescence lifetime distributions of the probe perylene in TPP at 220 K. (**A**) The lifetime distribution of liquid 1 (right/black) and liquid 2 (left/black) and their corresponding Gaussian fits (dashed lines). (**B**) The lifetime distribution obtained at the approximate halfway point in the transition (black). The distribution was fitted with two Gaussians (blue and green).*

2.6.4 FLIM vs. TCSPC

The FLIM technique is uniquely capable of distinguishing small differences in fluorescence lifetimes in inhomogeneous samples that cannot be resolved by bulk measurements. This was imperative in our studies of the LLT in TPP described in Chapter 4. To demonstrate this, TCSPC data were simulated using an exponential decay function that incorporated Poisson noise (to simulate the effect of laser noise) decaying to a Poisson noise floor (to simulate the effect of detector noise). The simulated TCSPC data removed uncertainties due to pulse shape in the experimental data.

Figure 23B shows that the data sets collected from two distinct regions, with fluorescence lifetimes of 4.0 and 4.3 ns, could be easily resolved through fitting. When combined into a single set, to simulate a bulk measurement (Figure 23C), fitting with a single exponential resulted in an average fluorescence lifetime of 4.15 ns and $X^2 \sim 1$. Fitting the same set of data to a double exponential did not improve the fit and did not allow the extraction of two fluorescence lifetimes.

This reflects what was observed in case of the actual experimental data – the fluorescence lifetimes of liquid 1 and liquid 2 could be easily identified by FLIM measurements. However, averaging of all TCSPC data from a FLIM map into a single TCSPC decay curve, led to a single exponential decay with a fluorescence lifetime with the value corresponding to the average of that in liquid 1 and liquid 2.

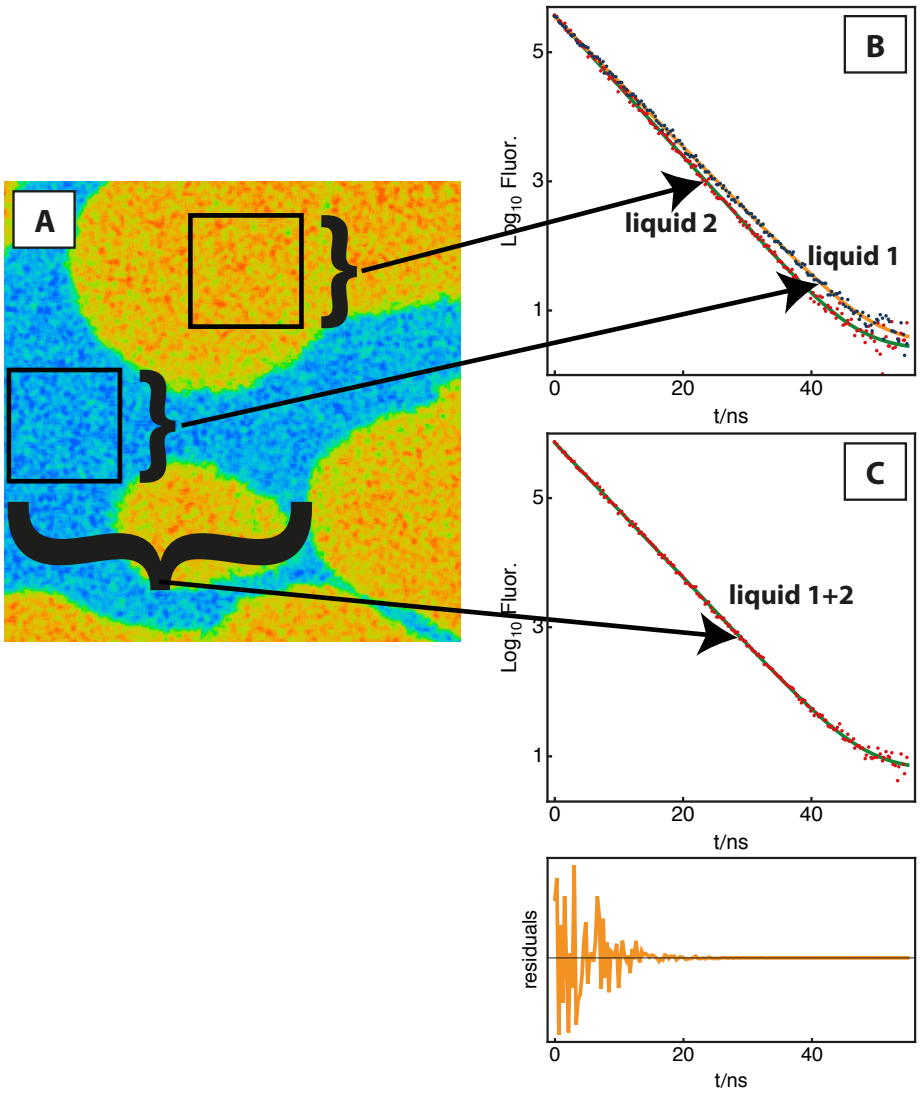

Figure 23. *Very similar fluorescence decay times, unresolvable by bulk measurements, can be easily resolved by FLIM. (**A**) Representative image obtained during the NG-type LLT from liquid 1 (blue) to liquid 2 (yellow) in TPP. (**B**) Simulated exponential decay traces with decay times of 4.0 and 4.3 ns. (**C**) The sum of the two traces fitted with a single exponential decay function.*

2.6.5 Linkam microscope stage THMS600

Apart from the dark field imaging, the remaining experiments described in this thesis were carried out using the Linkam heating and freezing stage THMS600 (Figure 24). This stage replaced a standard microscope stage on all three microscopes used. Its main advantages were the accurate temperature control and the moisture-free experimental environment.

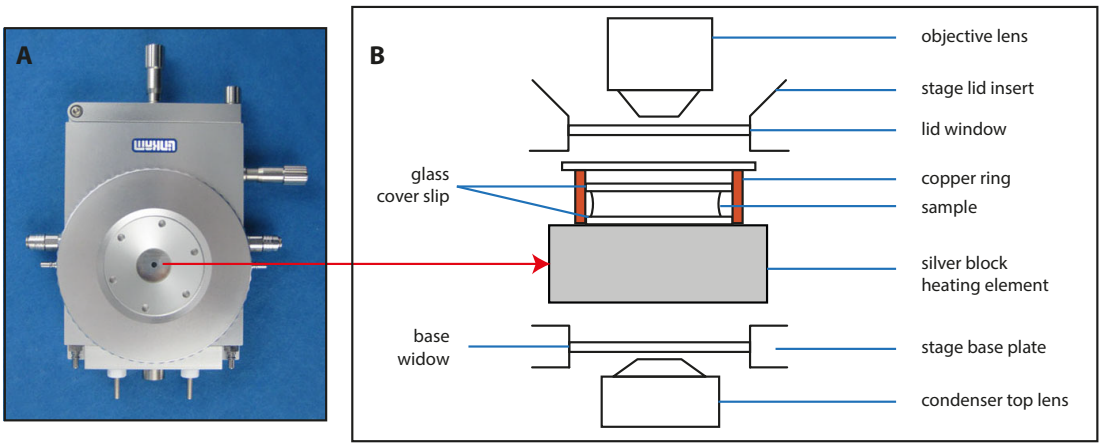

Figure 24. *Linkam heating and freezing stage THMS600. (**A**) Top view. (**B**) Position of a sample in the Linkam stage.*

Three different sample-loading protocols were employed depending on volatility and moisture-sensitivity of the investigated liquid. In case of all experiments carried on triphenyl phosphite (TPP), a drop of liquid was sandwiched between two disposable ø 16 mm glass cover slips placed inside a copper ring covered by a ø 19 mm glass cover slip (Figure 24). The sample thickness was controlled by using ø 11.58±0.19 µm monodisperse particle standards (Whitehouse Scientific). Typical temperature cycle for the experiments on TPP in shown in Figure 25. Before the experiment was performed, the sample chamber needed to be purged for about 20 minutes to eliminate condensation. When the purging was complete, a sample was cooled to the selected temperature at a rate of 10 K/min. To ensure that any residual moisture was not affecting data collection, all samples were cooled at a slower rate of 2 K/min in the range between 278 K and 268 K. This enabled any residual moisture present inside the sample chamber to condense on the coolest parts of the chamber *i.e.*, the cooling tubes.

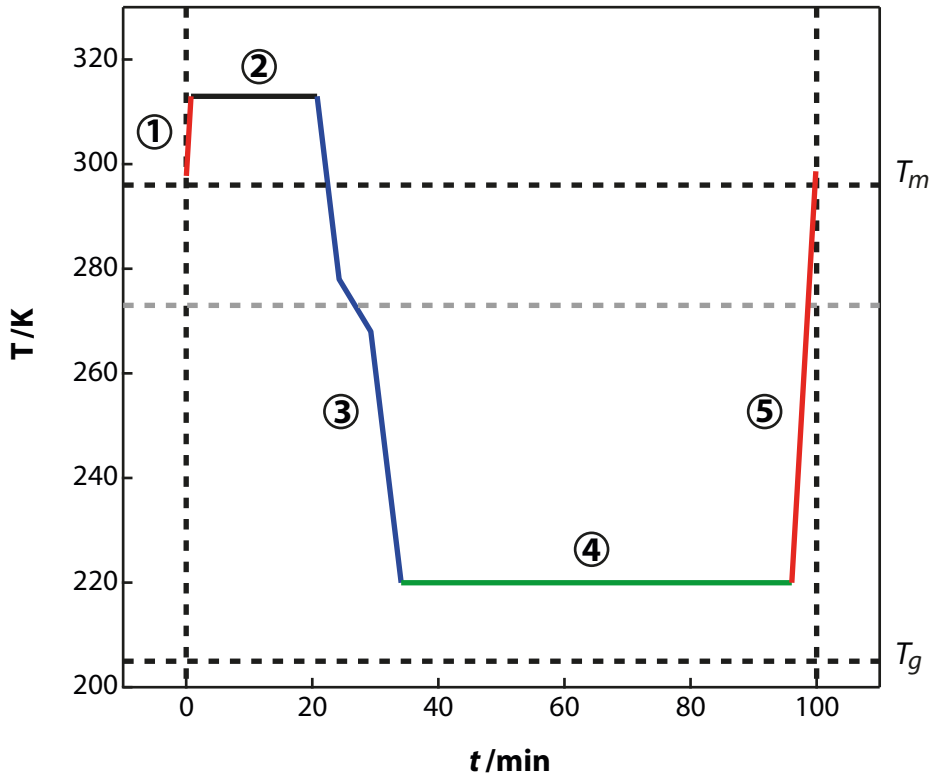

Figure 25. *Typical temperature cycle for experiments performed on TPP. (**1**) Heating to the purging temperature; (**2**) Purging; (**3**) Cooling to the selected LLT temperature; (**4**) LLT - data collection; (**5**) Heating to the room temperature, above the melting temperature of TPP (T_m = 296 K). All experiments were performed at temperatures above the glass transition temperature of TPP (T_g ~ 205 K).*

For experiments on *n*-butanol, the empty sample chamber was first purged for about 20 minutes and cooled down to about 243 K. The stage was then placed in the DIY low-temperature glove box (Figure 26) at a temperature of about 253 K. As in case of TPP, a drop of liquid was sandwiched between two disposable ø 16 mm glass cover slips placed inside a copper ring covered by a ø 19 mm glass cover slip (Figure 24). The sample thickness was controlled by using ø 11.58±0.19 μm monodisperse particle standards (Whitehouse Scientific). Once the sample was loaded, the stage was removed from the glove box and connected to the Linkam controllers and cooled down to the required temperature.

Highly volatile and hygroscopic liquids, such as 1,2-dichloroethylene, carbon disulphide, and solutions of nitrobenzene in hexane, required the use of a THMSQ quartz crucible, which allowed loading larger volume samples. The empty sample chamber was first purged for about 20 minutes and cooled down to about 243 K. The stage was placed

in the DIY low-temperature glove box at a temperature of about 253 K. The sample was loaded from a bottle, stored previously in the freezer. The crucible was covered with a ø 19 mm glass cover slip. Once the sample was in the crucible, the stage was removed from the glove box and connected to the Linkam controllers and quickly cooled down to required temperature (*e.g.*, 243 K for trans-1,2-dichloroethylene) to make sure that the temperature would not rise uncontrollably. Afterwards the cooling stage was positioned on the microscope.

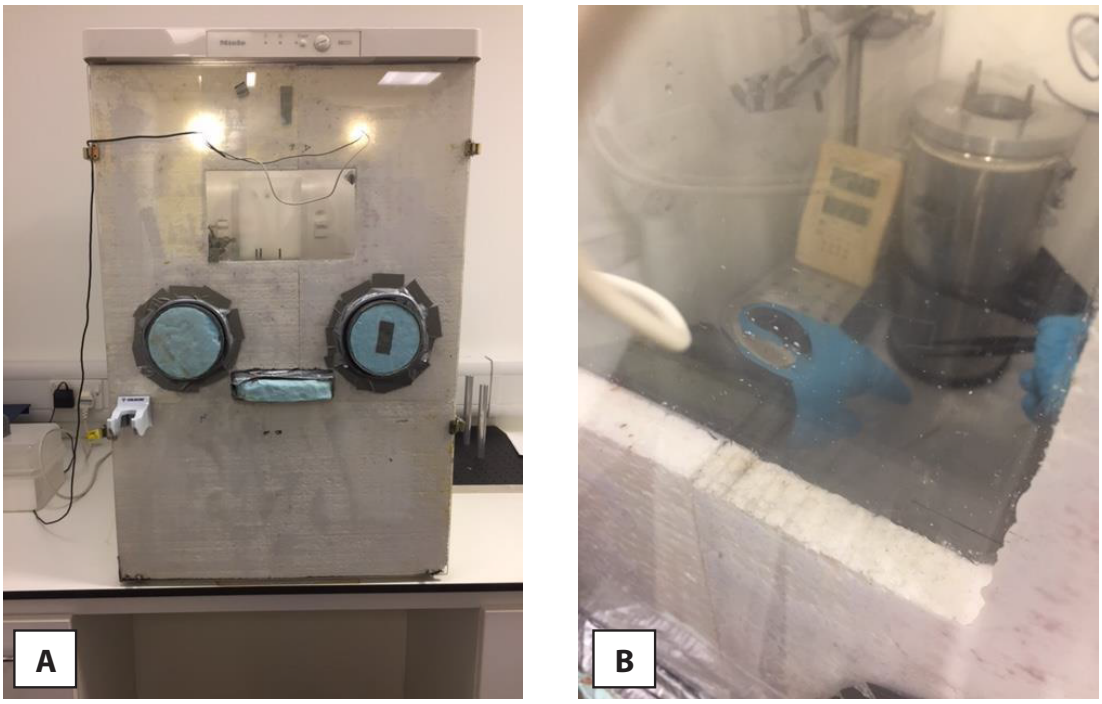

Figure 26. *DIY low-temperature glove box used to handle hygroscopic samples made by Dr David Turton. (**A**) Front view shows that the freezer doors was replaced by an insulated front panel with holes for arms and any object that needed to be put inside it. (**B**) Inside the glove box.*

2.6.6 Materials

2.6.6.1 Chapter 3

Nitrobenzene (>99.9%) and hexane (99.2%, <0.001% water by Karl Fisher coulometry) were purchased from Sigma Aldrich and used as supplied. Experiments were carried out on solutions with 0.1%, 1%, and 10% nitrobenzene in hexane by volume.

The experiments on *trans*-1,2-dichloroethylene (99.6%), purchased from Sigma Aldrich, were carried out on solutions with two concentrations of 80 or 458 ppm of water as determined by Karl Fisher coulometry. The first solution was *trans*-1,2-dichloroethylene used as supplied. The second solution was prepared by saturating *trans*-1,2-dichloroethylene with water at room temperature.

Cis-1,2-dichloroethylene (97%) and carbon disulfide (99.9%) were purchased from Sigma Aldrich and used as supplied.

2.6.6.2 Chapter 4

Triphenyl phosphite (TPP), coumarin 153 (C153) and perylene were purchased from Sigma Aldrich and used as supplied. The concentration of all solutions used in fluorescence microscopy experiments was ~10^{-5} M. At concentrations up to 10^{-4} M, we could experimentally rule out aggregation of the dye molecules used in TPP.

The protocol of sample loading is described in Section 2.6.5. After loading, a sample was quenched and held at a selected temperature.

The thermodynamically stable crystalline state (crystal 1), required for some experiments, was prepared by rapid supercooling of liquid 1 to about 230 K following by slow heating to about 280 K. The temperature was then lowered to a desired value and measurements performed.

2.6.6.3 Chapter 5

The experiments described in this chapter were carried out on anhydrous *n*-butanol (99.95% pure, 0.001% water content as determined by Karl Fischer titration), coumarin 153 (C153) and perylene purchased from Sigma Aldrich and used as supplied. The concentration of all solutions used in fluorescence microscopy experiments was ~10^{-5} M.

The protocol of sample loading is described in Section 2.6.5. After loading, a sample was quenched and held at a selected temperature.

In some experiments liquid 1 was quenched to 136 K to initiate nucleation and held at this temperature until the droplets of liquid 2 reached a desired size. The temperature was then raised slowly to 173 K to transform the remaining liquid 1 into crystalline phase through cold crystallization.

3

Crystal Templating through Liquid-Liquid Phase Separation

The physical chemistry of crystal nucleation is of great fundamental and practical importance, yet still poorly understood. Controlled induction of crystallisation remains one of the grand interdisciplinary challenges on the border between chemistry, physics and chemical engineering.

Here we use bright field microscopy, dark field imaging and confocal Raman microscopy to study crystal nucleation in the presence of liquid-liquid phase separation using solutions of two liquids of small molecules. We show that under highly nonequilibrium conditions of spinodal decomposition, water crystallises into long thin asymmetric wires, structurally indistinguishable from hexagonal ice. It is a highly unexpected phenomenon, as the only known wire-like form of ice requires a physical template and a fungal activity for its formation. The observations of this template-less "Haareis" (hair ice) formed as a result of liquid-liquid phase separation from mixtures of water and non-polar liquids strongly suggest that such conditions may be used to control crystal growth.

3.1 Introduction

Crystallisation always involves nucleation, a first-order phase transition resulting in the formation of solid particles. The understanding of the mechanisms behind phase separation and crystal nucleation is of great fundamental and practical importance yet is still rather limited. The existing classical and non-classical nucleation theories were described in Section 1.3.

In the classical approach to crystallisation, a substance is dissolved in a solvent to form a solution and thereafter cooled to a certain concentration-dependent temperature at which the solution becomes supersaturated and metastable. This can in principle result in crystal nucleation (Figure 27). On further cooling, at even lower temperature, the solution becomes unstable and homogeneous crystal nucleation occurs.

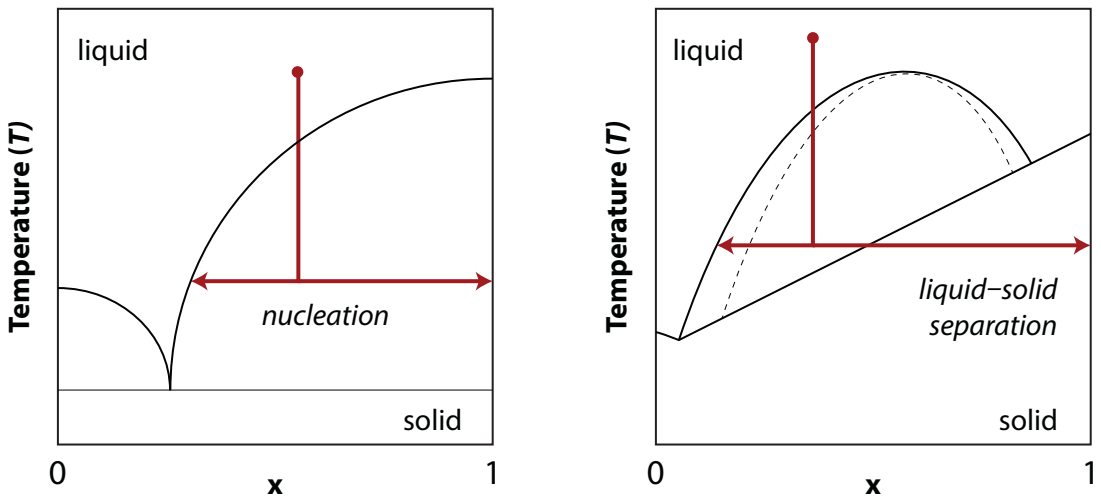

Figure 27. *Binary solid-liquid phase diagrams. (**left**) A system composed of two well-mixing substances will exhibit a eutectic point. Cooling of such mixture will result in nucleation of a solid phase. (**right**) Cooling of a mixture of two poorly mixing substances will give rise to liquid-liquid demixing, which in particular cases, can be followed by crystallisation of one of the substances. Dashed line is the spinodal.*

When a solution is prepared from two liquids that do not interact favourably, usually at high temperature entropy favours the mixed state. When the system is cooled to the temperature at which the spinodal is crossed, the system becomes unstable and liquid-liquid phase separation (demixing) occurs (Figure 27). At the spinodal boundary,

the barrier for phase separation disappears and decomposition happens spontaneously, assuming nucleation was avoided up to this point.[97]

In the 1990s, Frenkel introduced the concept of the enhancement of crystal nucleation due to the presence of a metastable liquid–liquid critical point. It is considered well known that the crossing of a free energy barrier limits the rate of crystal nucleation. Frankel's numerical simulations have shown that the presence of large density fluctuations at either side of the critical temperature T_c and critical concentration drastically changed the free-energy landscape and lowered the nucleation barrier. This resulted in the increase of the nucleation rate by a factor 10^{13}. The most common method of increasing of the nucleation rate is to prepare a more saturated solution, however by doing so the thermodynamic driving force for crystallisation is also enhanced leading to rapidly growing ill defined amorphous or polycrystalline objects.[131-133] The reduced crystal nucleation barrier near T_c should, in theory, allow for a selective increase in the crystal nucleation rate by *e.g.* adjusting the solvent conditions and by doing so controlling the location of the liquid-liquid critical point.[134] According to Frenkel a critical point would enhance the probability of the occurrence of nucleation (either classical or non-classical) by inducing concentration fluctuations leading to formation of droplets of so-called "dense fluid".[106, 135-137] Nowadays, this concept is widely used in chemical engineering to describe crystal nucleation of small molecules where the formation of this "dense fluid" is referred to as "oiling out".[131, 138] However, Frenkel's concept was developed based on numerical simulations of homogeneous nucleation of globular proteins with short-range attractive interactions.[134] Hence the direct application of this theory for suspensions of mesoscopic objects to small molecules in solution is unlikely to be straightforward as the interaction strengths are very different.[139, 140]

Here we will take a systematic approach and study crystal nucleation in the presence of (a critical point for) liquid–liquid phase separation using liquids of small molecules and will demonstrate that high driving force does not necessarily lead to ill-defined crystalline forms. In order to test the Frenkel's concept of crystal nucleation, two systems (a "solute" liquid and a "solvent" liquid) were chosen in which the solute-rich fraction after phase separation is most stable in its solid state (see Figure 27).

The first chosen system was the well-known mixture of nitrobenzene and hexane. The calculated temperature-composition phase diagram for this system is shown in Figure 28. Due to significant polarity difference between nitrobenzene and hexane, this system requires thermal energy to overcome the tendency to separate. It has an upper

consolute temperature, T_{UC} (or upper critical solution temperature) of 293.55 K at a critical nitrobenzene mole fraction of 0.4275. Above T_{UC} both component liquids are fully miscible in all proportions.

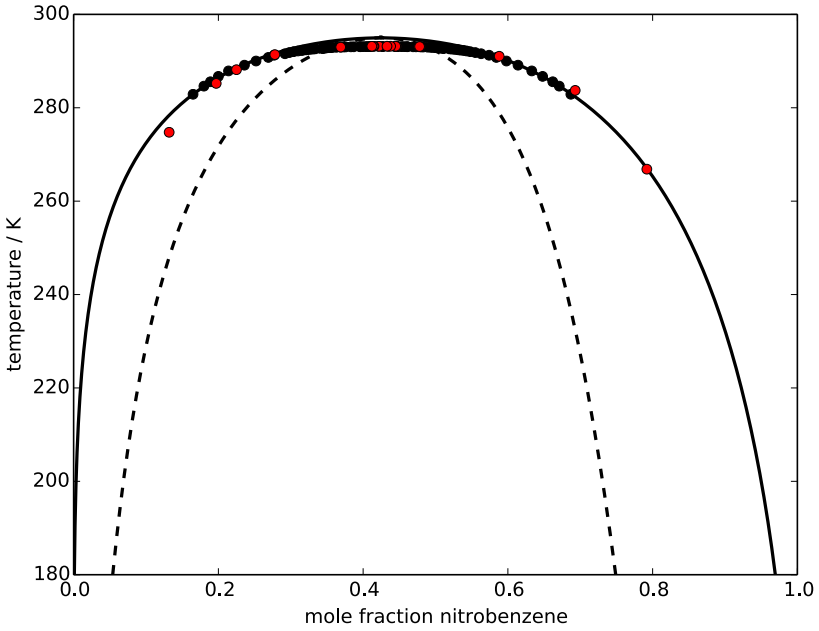

Figure 28. *The temperature-composition phase diagram for hexane and nitrobenzene calculated by our collaborator Leo Lue. Points represent previously reported experimental data.*[141] *Solid black line is the binodal and dashed line is the spinodal (estimated).*

The second chosen system was a mixture of 1,2-trans-dichloroethylene and water. 1,2-dichloroethylene (also called 1,2-dichloroethene or 1,2-DCE) has two geometric isomers, *cis*-DCE (a planar structure, a dipole moment of 1.9 D) and *trans*-DCE (a planar structure, no dipole moment). It is widely used in the plastics industry, dry cleaning and many other areas as a solvent for waxes, resins, polymers, fats, and lacquers.[142, 143, 52]

In 1981 Kawanishi *et al.* reported evidence for a liquid-liquid transition (LLT) and a novel liquid phase of *trans*-DCE at high pressure based on the results obtained with pulsed NMR and pressure-volume measurements.[144] A year later they published results for both DCE isomers concluding that only *trans*-DCE undergoes an LLT at atmospheric pressure at -16°C (257 K).[145] Zegrodnik and Hacura confirmed findings of Kawanishi for trans-DCE using the Raman spectroscopy suggesting that the liquid state order-disorder transition is involved.[146]

More recently, Merkel *et al.* reported that jumps observed in mid-infrared absorption spectra at 247 K indicate an occurrence of an LLT in *trans*-DCE. [147] This behaviour was ascribed to the local ordering of the molecular system due to the charge distributions of dimers formed. The results of measurements of specific heat capacity, X-ray diffraction, and non-linear dielectric effect spectroscopy, published by Rzoska *et al.*, also show evidence of an anomaly at the same temperature.[148]

However, Turton *et al.* reported that temperature-dependent optical Kerr-effect (OKE) spectra of both DCE isomers did not demonstrate any discontinuity. OKE is sensitive to the molecular interactions such as the low frequency rotations, translations, and vibration. Therefore it would be surprising if a change in structure of the liquid would not affect it. Despite the lack of evidence for an LLT, the report concluded with the observation of unexplained heterogeneities.[149]

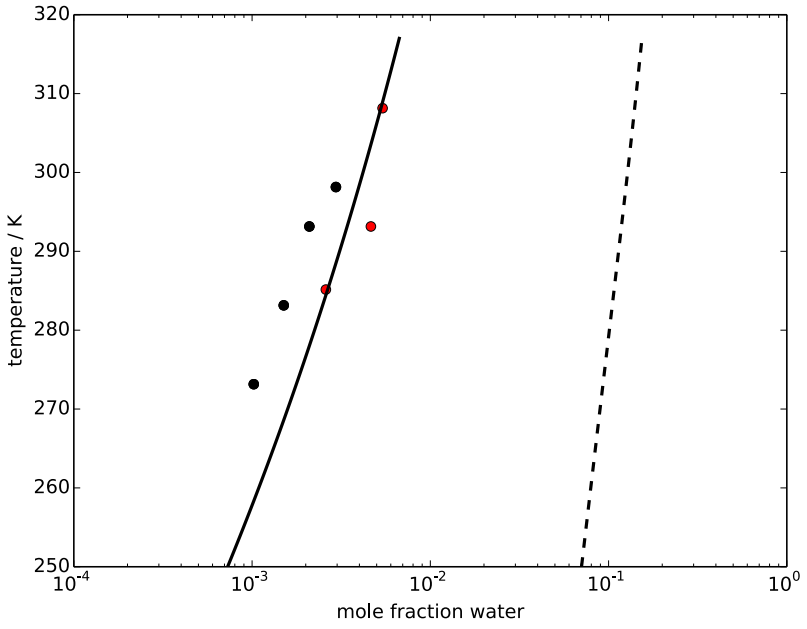

Figure 29. *The partial temperature-composition phase diagram for water and 1,2-trans-dichloroethylene calculated by our collaborator Leo Lue. Points represent previously reported experimental data.[141] Dashed line is the spinodal that was estimated based on limited solubility data.*

After extensive studies on *trans*-DCE, we identified the nature and origin of these heterogeneities as a novel form of hexagonal ice formed as a result of liquid-liquid separation from a mixture of *trans*-DCE with trace amounts of water. Our findings were

followed by systematic studies on this system described in the next section. The upper consolute temperature and critical mole fraction for this system in not known but the binodal and spinodal are estimated to be steep functions of the water mole fraction (Figure 29).

3.2 Results

The systematic studies of two poorly mixing binary systems, namely nitrobenzene-hexane and water-*trans*-1.2-dichloroethylene (melting temperatures as per Table 1), were carried out. The chosen variables were concentration and the cooling rate, which enabled us to place the systems in a range of experimental conditions ranging from highly nonequilibrium states to full equilibrium.

Table 1. *Melting temperatures of studied organic liquids.*

	T_m (°C)	T_m (K)
nitrobenzene	5.7	278.7
hexane	-95	178
trans-1,2-dichloroetylene	-50	223
cis-1,2-dichloroetylene	-80	192
carbon disulfide	-111.6	161

3.2.1 Nitrobenzene-Hexane

The system studied first was a mixture of nitrobenzene in hexane. The experiments were carried out on samples with 0.1%, 1%, and 10% nitrobenzene in hexane by volume (v/v).

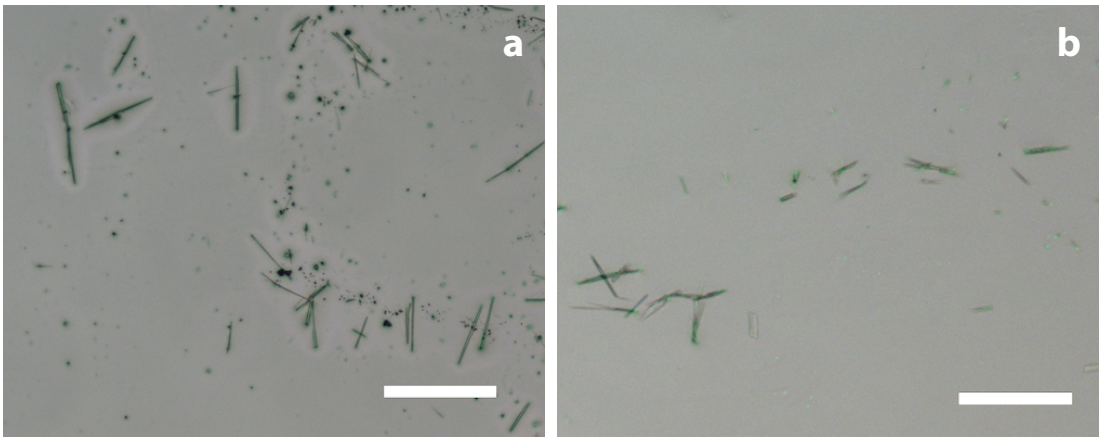

Figure 30. *Bright field microscopy images of nitrobenzene crystals formed as a result of liquid-liquid phase separation in 0.1% v/v solution of nitrobenzene in hexane. Phase separation was observed at 183 K. The solutions were cooled down at 0.5 K/min (**a**) and 10 K/min (**b**). Scale bar corresponds to 100 μm.*

Based on the phase diagram in Figure 28, the liquid-liquid phase separation for these solutions was predicted to occur at 184.0, 225.9, and 277.6 K respectively. The samples were cooled down to these temperatures at three different cooling rates of 0.5, 10 and 50 K/min.

As can be seen in Figure 30, the samples containing 0.1% v/v nitrobenzene produced very small needle-like crystals. The length of these crystals, formed at 0.5 K/min, ranged from 30-100 μm and 20-50 μm when the samples were cooled at 10 K/min. The 1% v/v nitrobenzene samples produced larger needle-shaped crystals at all three cooling rates. However, the samples containing 10% v/v nitrobenzene produced needle-like crystals only at the slowest cooling rate of 0.5 K/min. Figure 31 shows that at the cooling rate of 10 K/min, both small crystals and round amorphous shapes were observed. However, at the highest cooling speed of 50K/min, nitrobenzene crystallised into large amorphous shapes.

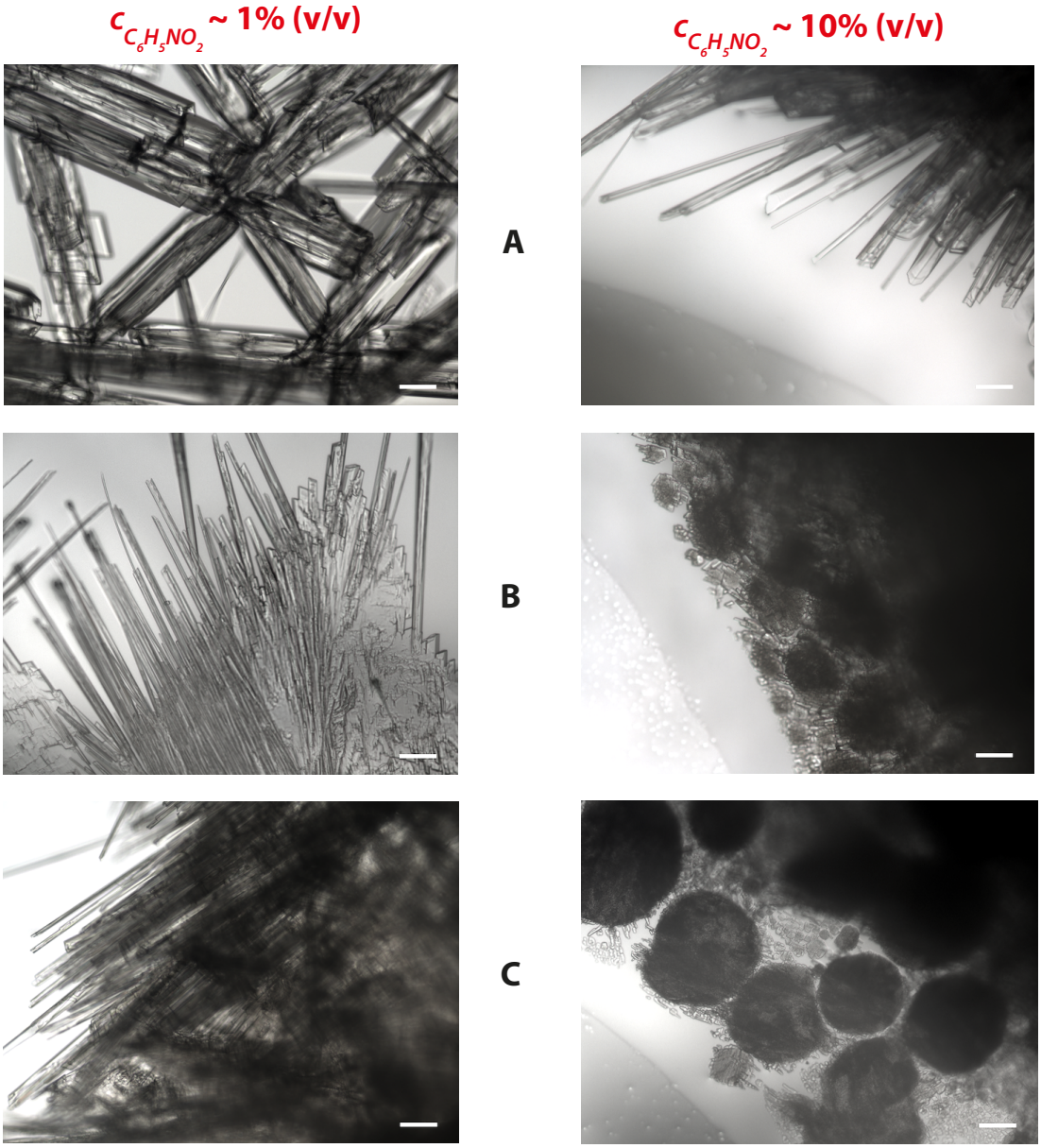

Figure 31. *Bright field microscopy images of nitrobenzene crystals formed as a result of liquid-liquid phase separation from hexane. The solutions of 1% v/v (left column) and 10% v/v (right column) nitrobenzene in hexane, with phase separation observed at 223 K and 253 K respectively, were cooled down at 0.5 K/min (**A**), 10 K/min (**B**) and 50 K/min (**C**). Scale bar corresponds to 100 μm.*

3.2.2 Water – Trans-1,2-Dichloroethylene

The second system studied was the mixture of water in *trans*-1,2-dichloroethylene (*trans*-DCE). These two liquids mix very poorly, however due to *trans*-DCE being hygroscopic, the presence of water traces is very difficult to avoid. The first concentration studied was the supplied *trans*-DCE containing 80-ppm of water with a predicted liquid-liquid equilibrium at 238 K (Figure 29). The second concentration studied was the highest concentration of water in *trans*-DCE at room temperature, *i.e.* 458 ppm. The water content in both solutions was determined by Karl Fischer coulometry.

Figure 32 shows dark field images of the effect that occurred in the bulk sample. When the mixture of water and *trans*-DCE was cooled to about 5-10 degrees above the melting temperature of *trans*-DCE (see Table 1), the nucleation and growth of water fluff, carried by the convection current, was observed. As the temperature of the solution was reaching the equilibrium, they were gradually adhering to the walls of the cuvette. A closer look revealed that numerous micro-scale agglomerations were attached to the quartz wall, while a few macro-scale agglomerations nucleated on the curved liquid-gas interface.

The microscopic studies revealed that the crystal formation patterns, as a function of cooling rate, were very similar to those observed in the nitrobenzene-hexane mixture (Figure 33). High cooling rate (50 K/min) resulted in formation of round polycrystalline structures. At low cooling rate (0.5 K/min), only crystalline structures were observed, whilst the intermediate cooling speed (10 K/min) resulted in a mixture of both types of morphology.

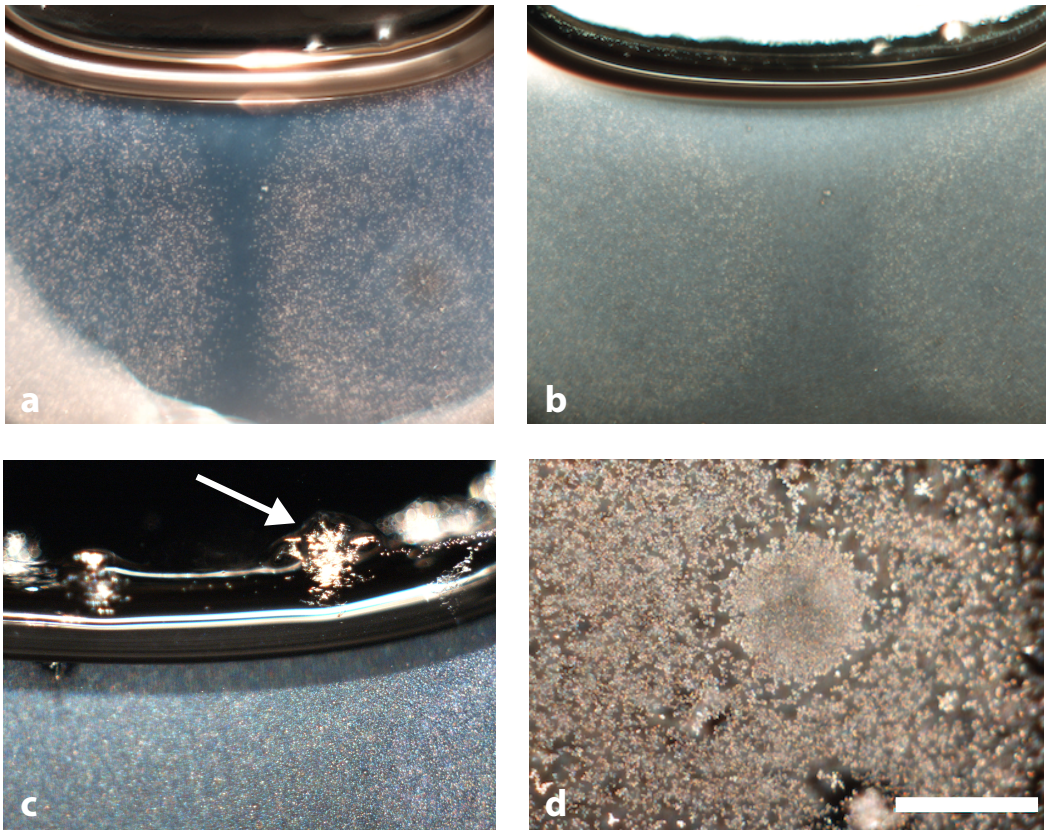

Figure 32. *Dark field images of water crystals formed in trans-DCE cooled to 218 K. (**a**) Water fluff was seen floating in supercooled liquid as the temperature was reaching equilibrium. (**b** and **d**) After a few minutes water fluff started adhering to the walls of the cuvette. (**c**) Large agglomerations of water fluff formed on the curved gas-liquid interface. Scale bar corresponds to 1000 μm.*

However, the appearance of water crystalline structures formed as a result of liquid-liquid separation from *trans*-DCE was highly unusual (see Figure 35). These structures grew as very long thin curved wires, occasionally splitting producing an array of side branches pointing in a single direction and forming asymmetric brush-like features as can be seen on the series of images in Figure 34. At the lower cooling rates, these wires entangled into meso- or even macro-scale balls looking like "fluff". Typical thickness of the wires was 2 μm but the range of sizes varied from 1 to almost 4 μm. The largest balls of water fluff seemed to grow near the curved liquid-gas interface and these were visible to the naked eye (see Figure 33b).

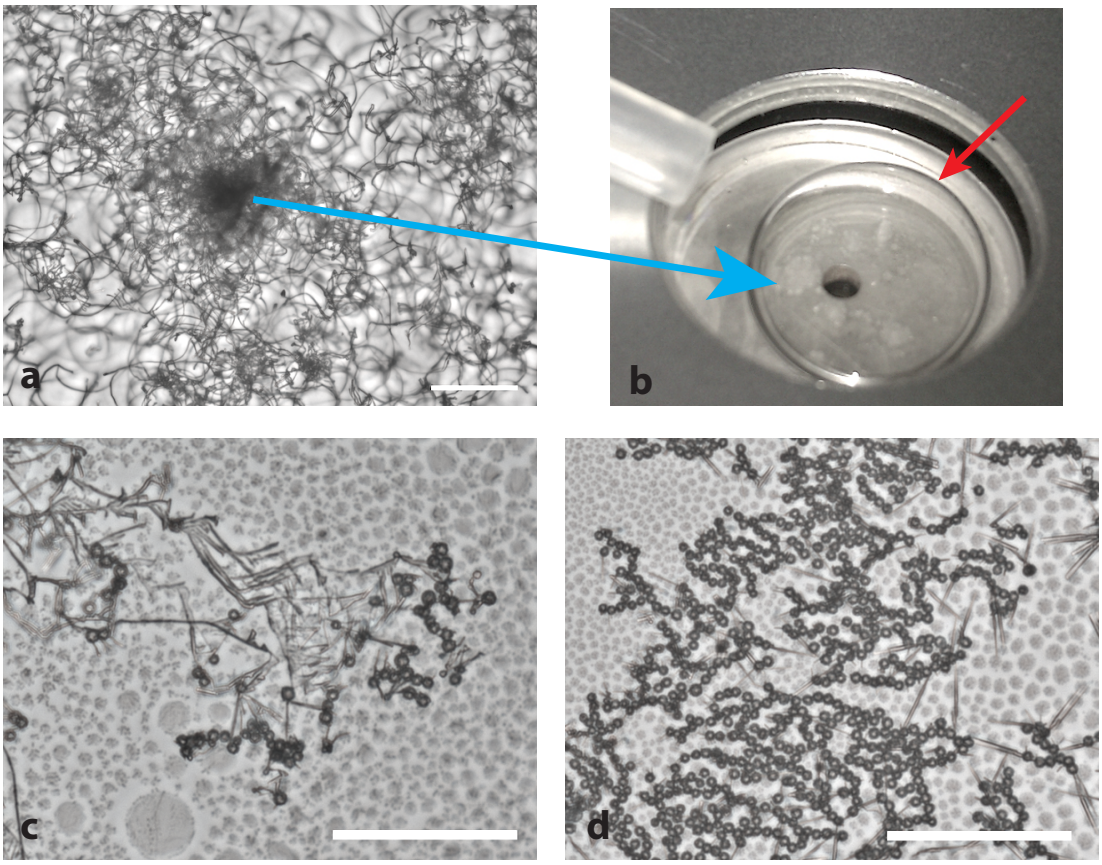

Figure 33. *Bright field microscopy images of water crystals formed during liquid-liquid phase separation from trans-DCE containing 458-ppm water. Different cooling rates resulted in different morphology of nucleating ice crystals. (**a**) Long asymmetric wires entangled into ball-like agglomerations were formed at about 255 K at the cooling rate of 0.5 K/min. (**b**) Top view through the cooling stage window. Blue arrow points at large agglomerations of wires visible with the naked eye. Red arrow points at liquid-gas interface. (**c**) A mixture of asymmetric wires and round structures was observed when the mixture was cooled to 233 K at 10 K/min. (**d**) The cooling rate of 50 K/min resulted in round structures nucleating at about 233 K. Scale bar corresponds to 100 μm.*

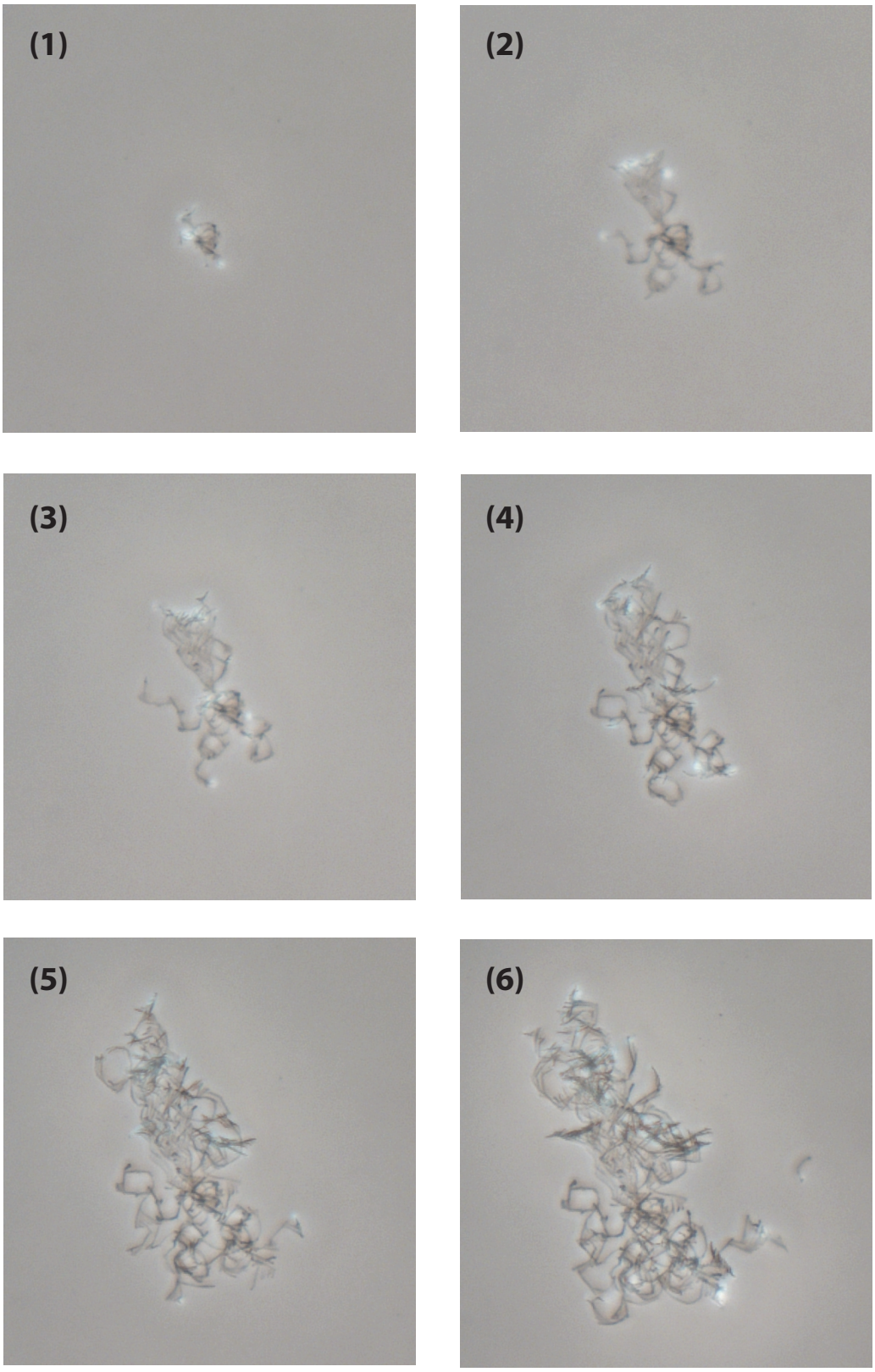

Figure 34. *Bright field microscopy images of water fluff nucleating and growing in trans-DCE cooled to 228 K at 15 K/min. It took about 1 min for this structure to be fully formed.*

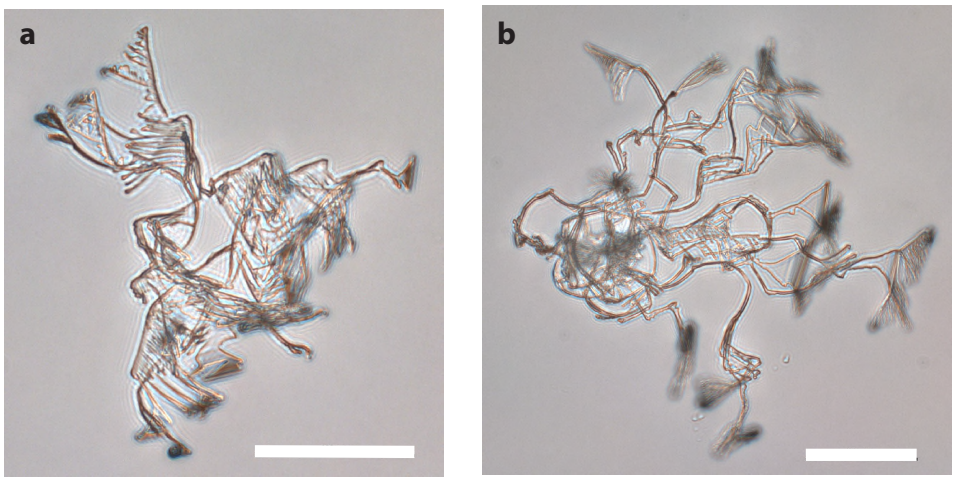

Figure 35. *Bright field microscopy images showing unusual appearance of water crystals formed in trans-DCE at 233 K. Scale bar corresponds to 100 µm.*

Despite the presence of water fluff, *trans*-DCE could be supercooled to about 20 degrees below the melting temperature. Crystallisation was rapid which strongly suggests that the present water fluff did not initiate it. The fluff structures could be seen lodged in the crystalline phase of *trans*-DCE and once the crystalline phase was re-melted, they reappeared essentially unchanged (Figure 36).

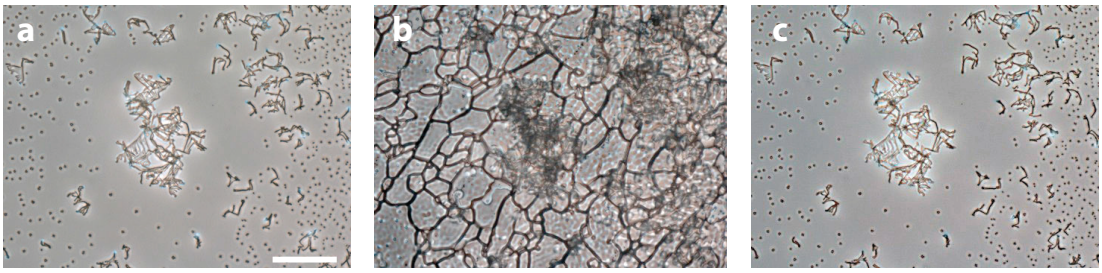

Figure 36. *Bright field microscopy images of fluff-like water crystals formed in supercooled trans-DCE at 213 K (**a**), embedded in crystalline phase of bulk liquid trans-DCE (**b**) and after re-melting at 228 K (**c**). Scale bar corresponds to 100 µm.*

Structural investigations on the observed unusual water structures were carried out using confocal Raman microscopy. The attempts were made to take the Raman spectra of the wires immersed in liquid *trans*-DCE. Two approaches were employed - collecting the data from a point with estimated up to 50% of wires in the studied volume and collecting numerous spectra along a line scan.

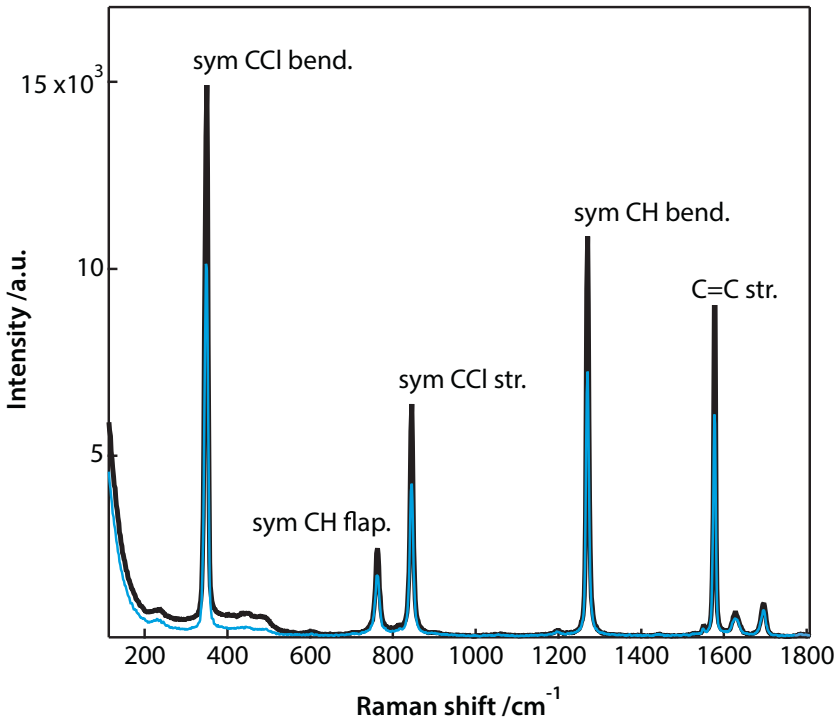

Figure 37. *Representative Raman spectra of liquid trans-DCE (black) and a selected spot were water fluff occupied estimated more than 50% of the studied volume (blue). Both spectra were recorded at 223 K.*

As can be seen in Figure 37 the Raman spectra of liquid *trans*-DCE and the selected spot containing fluff-like water crystals were practically indistinguishable. Figure 38 shows that despite the fact that majority of the sample volume was occupied by water fluff, the only observed changes in Raman spectra, as the line scan was performed, were the increase of the peak amplitudes and narrowing of the Raman bands of liquid *trans*-DCE. No additional peaks, which could be assigned to crystalline water, were observed. These results are not unexpected as water is a much weaker Raman scatterer than *trans*-DCE.

As both these approaches proved unsuccessful, Raman spectra of the wires were obtained after the extraction of liquid *trans*-DCE through vacuum evaporation at 228 K (Figure 14). Figure 39 shows the spectra in the region of the ice phonon band (150-350 cm^{-1}) and the OH-stretch region (2,800-3600 cm^{-1}). The Raman spectrum from 100 to 3,600 cm^{-1} was indistinguishable from that of hexagonal ice and did not show any activity in the CH-stretch region ruling out clathrate formation. Slight shifts (~5 cm^{-1}) in the phonon band were observed, which are attributable to size effects.

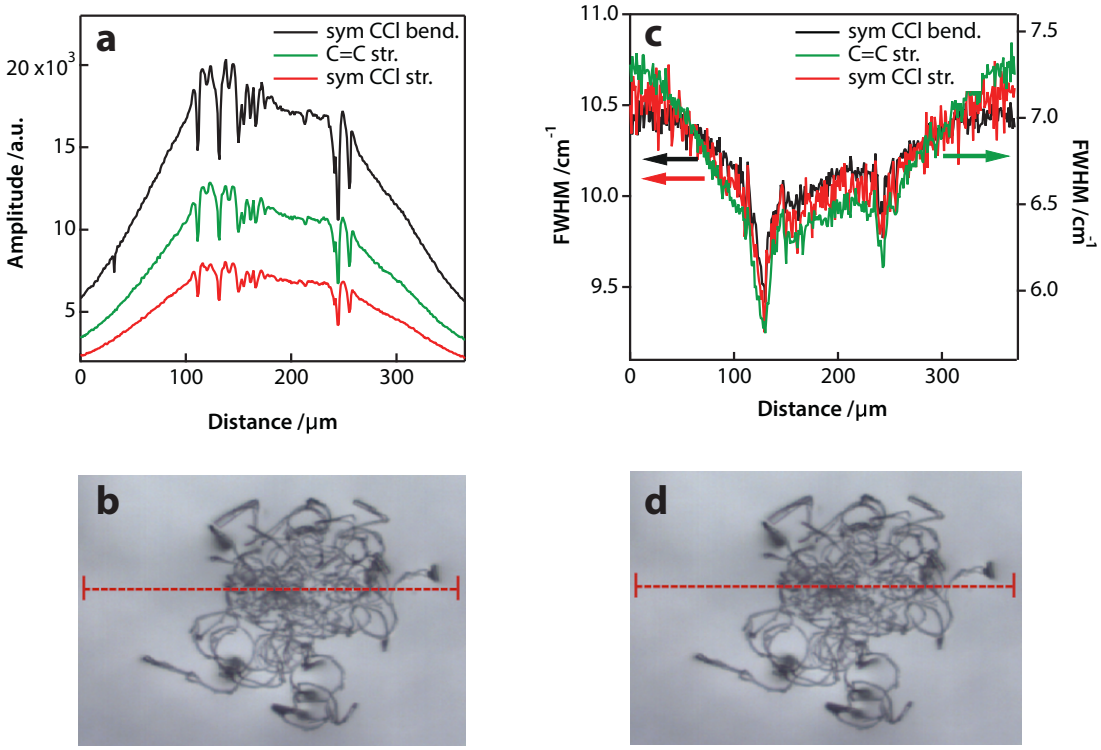

Figure 38. *Analysis of Raman scattering intensity (**a**) and FWHM (**c**) of selected Raman lines along the line scan across a fluff-like water crystal formed in trans-DCE at 223 K. The scan was performed along the dash red line shown on the microscopy images (**b** and **d**). This approach did not enable the detection of water crystals immersed in liquid trans-DCE.*

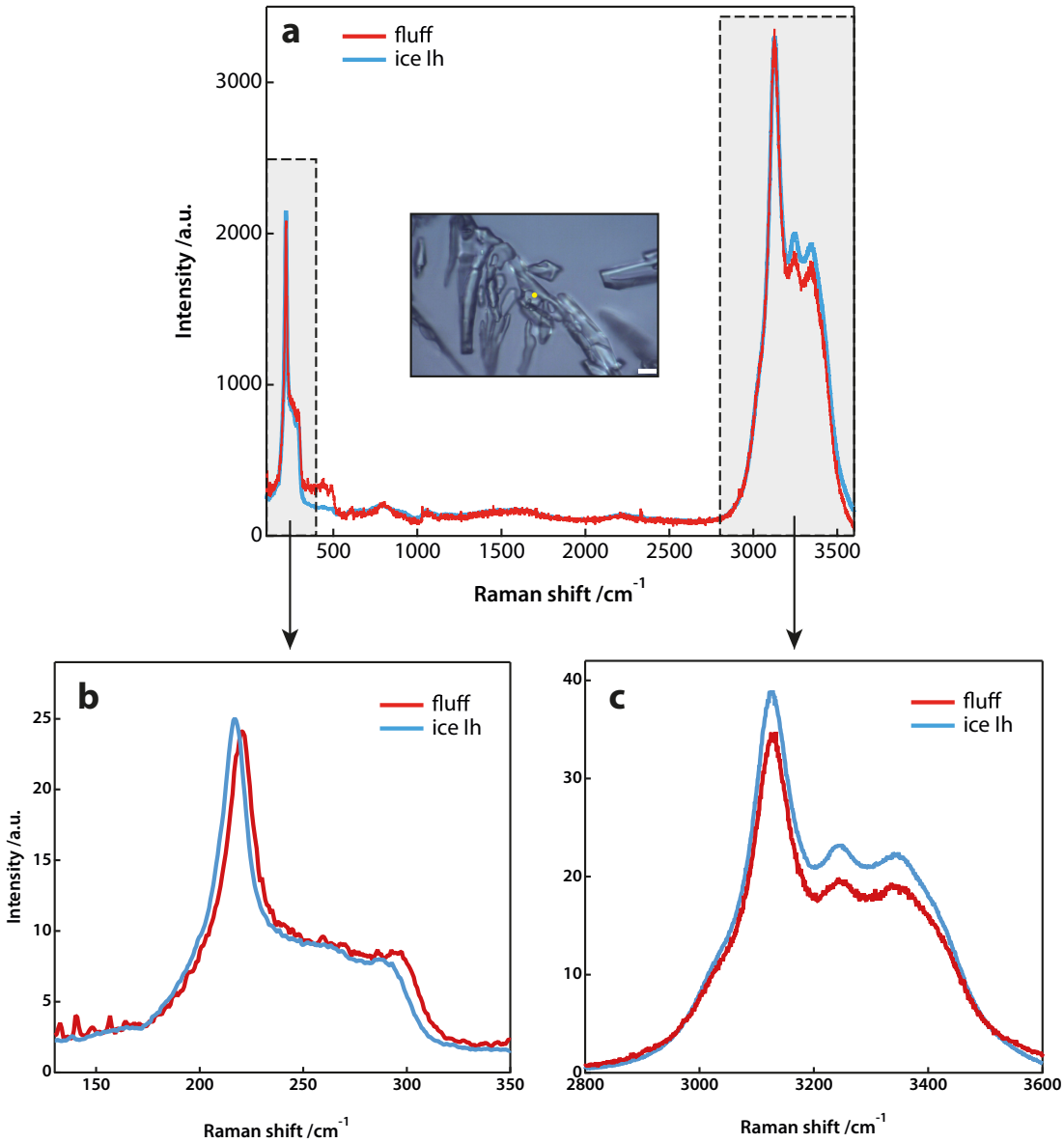

Figure 39. *Raman spectra of water crystals formed in trans-DCE. The spectra were recorded at 228 K after the removal of liquid trans-DCE was extracted. The measured relative intensity of hexagonal ice spectrum was almost twice as strong as the relative intensity of water fluff spectrum. (**a**) Raman spectrum of water fluff was practically indistinguishable from the spectrum of hexagonal ice. Insert in the top graph shows a microscopy image of the point (marked with the yellow dot) at which the spectrum of water fluff was taken. Scale bar 10 µm. (**b**) Spectra of fluff and hexagonal ice in the region of the ice phonon band. (**c**) Spectra of fluff and hexagonal ice in the OH-stretch region.*

3.2.3 Other systems

To investigate whether fluff-like water crystals were uniquely formed as a result of phase separation of water from *trans*-DCE, two other systems consisted of water and a nonpolar liquid were selected.

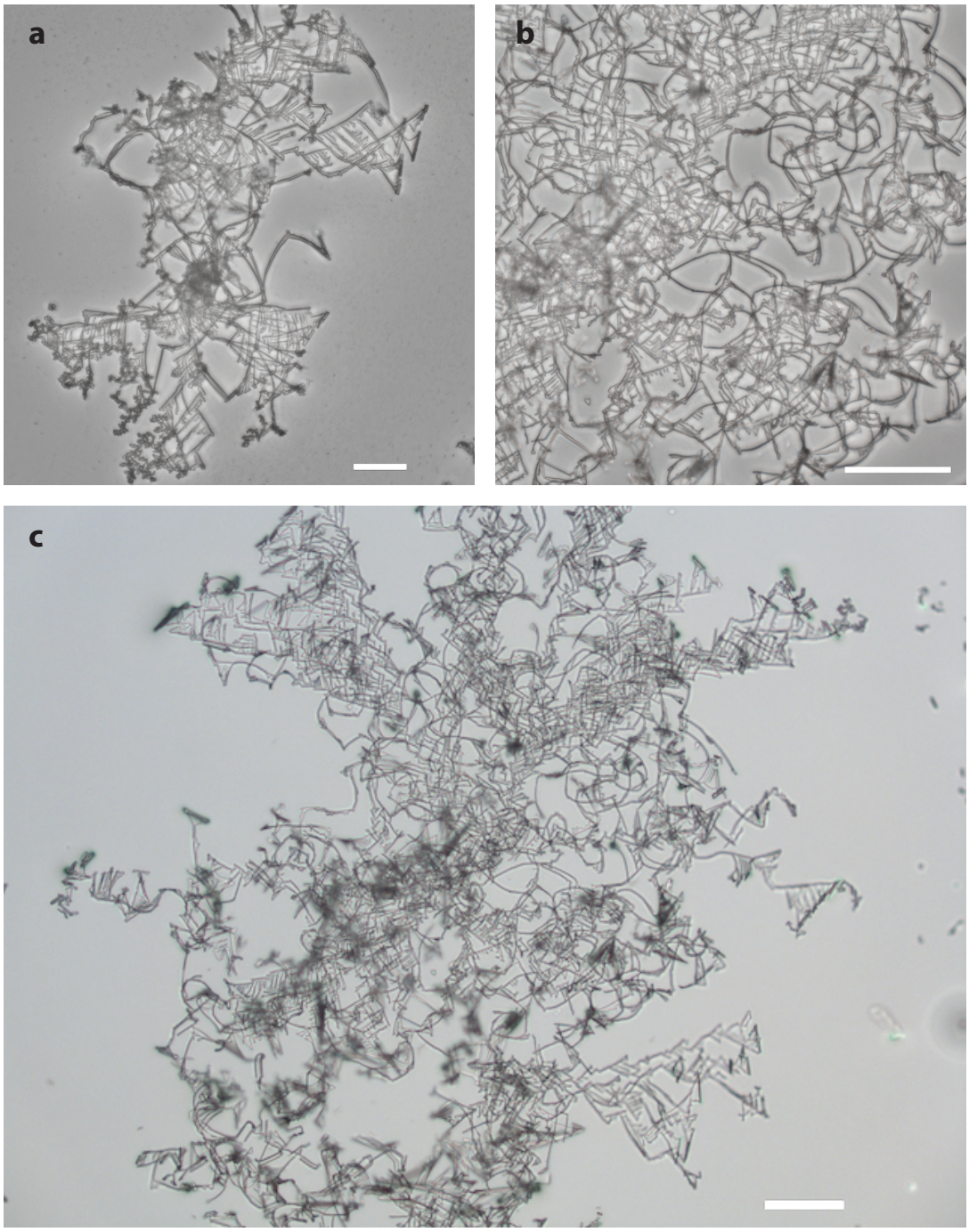

Figure 40. *Bright field microscopy images of fluff-like water crystals observed in cis-DCE after cooling the mixture to 193 K (**a**) and to 247 K (**b**, **c**) at 15 K/min. Scale bar 100 µm.*

Figure 40 shows the images obtained after cooling a mixture of *cis*-1,2-dichloroethylene (*cis*-DCE) and water to two temperatures above T_m of *cis*-DCE. It can be seen in that a similar phenomenon to that in *trans*-DCE was observed and it resulted in formation of large agglomerations of asymmetric wires of crystalline water.

Figure 41 shows the result of the experiment on the mixture of water and carbon disulfide (CS_2). In this case, no asymmetric splitting was observed, however crystalline water structures formed as a result of phase separation from this solvent, formed large agglomerations of curved wires, similar to that of *trans*-DCE.

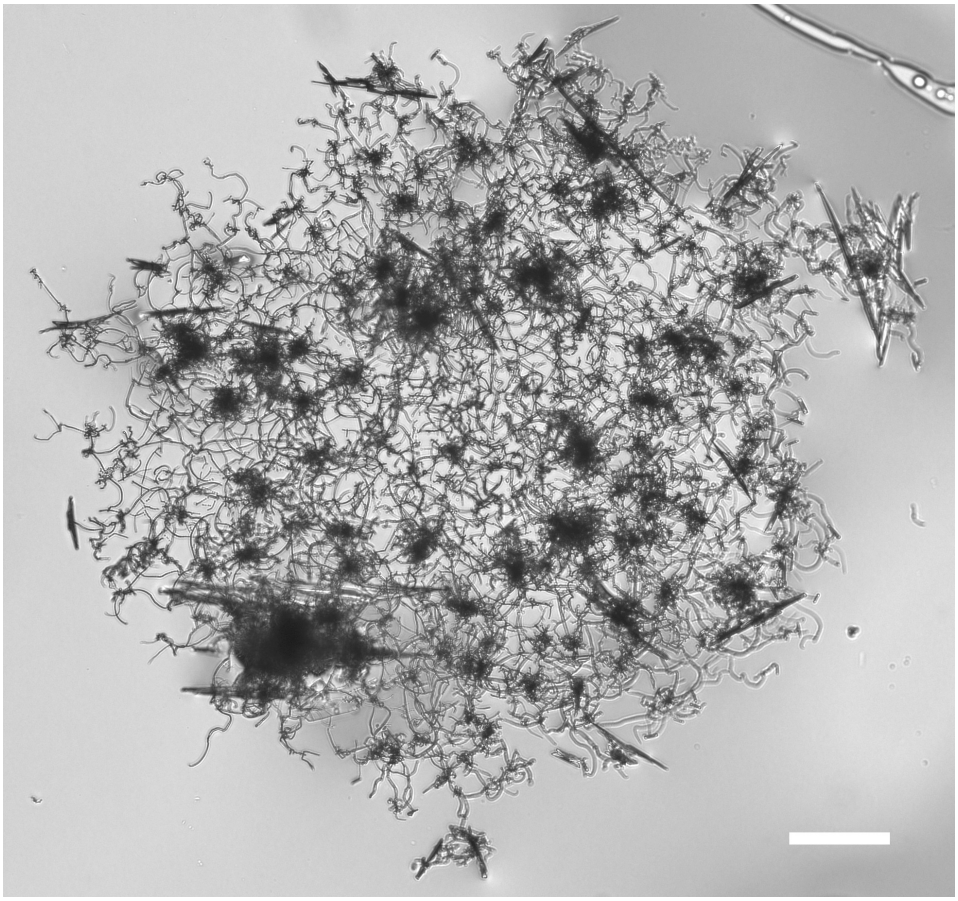

Figure 41. *Bright field microscopy images of fluff-like water crystals observed in CS_2 after cooling the mixture to about 258 K at 0.5 K/min. The concentration of water was about 15% by volume. Scale bar 50 μm.*

3.3 Discussion

The response of the mixture of nitrobenzene in hexane to different cooling rates was not as expected. All experimental temperatures were above the melting temperature of hexane (T_m = 178 K) and it remained in the liquid state at all times during our experiments. As the mixture was cooled below the liquid-liquid binodal, the nitrobenzene-rich fraction was unstable with respect to crystallisation of nitrobenzene (T_m = 278 K) and phase separated. The slowest cooling speed of 0.5 K/min created favourable conditions for nucleation of nitrobenzene-rich droplets followed by crystallisation and further growth of nitrobenzene crystals. However, the higher cooling rates allowed the system to remain metastable for long enough to cross the spinodal, which resulted in phase separation taking place globally leading to uncontrolled crystallisation of nitrobenzene and formation of round polycrystalline structures (Figure 31).

The chosen systems were studied experimentally in highly nonequilibrium conditions. There have been many previous experiments in which crystallisation in deeply supersaturated solutions were studied. It is well known that high driving force for nucleation results in ill defined amorphous or polycrystalline objects.[131-133] This was certainly the case with the nitrobenzene-hexane system pushed towards the spinodal of the liquid-liquid phase separation. It is almost certain that reports of "oiling out" [131, 138] are all related to the crossing of such spinodals, although the spinodal can be below the liquid–solid separation line in some cases. However, we found that in mixtures of poorly mixing liquids, *i.e.*, water in *trans*-DCE, water in *cis*-DCE and water in CS_2, crossing of the spinodal resulted in the formation of highly organised asymmetric wires without the use of any physical templates.

The observations of asymmetric structures of water fluff (*e.g.* in Figure 35 and Figure 40) were highly unexpected. The concentration of water in these systems was very low, in some mixtures on order of ppm. When ice crystals grow in an environment low in free water molecules (such as cold air), the limitation in the diffusional rate of these molecules results in the typical growth habit of the standard hexagonal form and creation of symmetric patterns. There are currently 121 known categories of snow crystal, ice crystal, and solid precipitation particles[150] but none of them is shaped like a wire or fluff. We observed, for the first time, novel fluff-like water crystals characterised by asymmetric branching and growth.

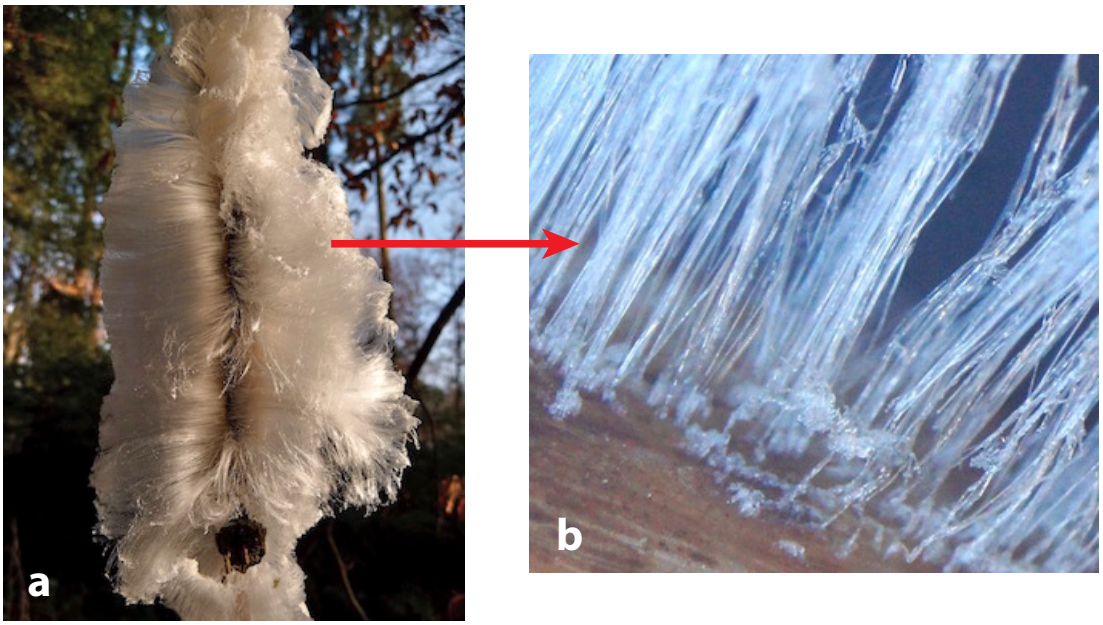

Figure 42. *Hair ice (also called ice wool) formed on a dead beechwood observed on 26 December 2009 in Moosseedorf, hair length up to 10 cm (**a**). The enlarged image showing individual ice hairs, image width 3.2 mm (**b**).*[151]

The only known wire-like form of water ice is called hair ice, ice wool or *Haareis*. It is a very unusual and little-known form of ice, which grows on the surface of unfrozen dead wood of certain broad-leaf trees. It requires calm, humid conditions and air temperature slightly below 0° C. The ice hairs are long, smooth and form beautiful structures such as waves and curls (Figure 42). This phenomenon has been first noted about a century ago, however its origin was very poorly understood until recently when Hofmann and co-workers carried out more in-depth studies taking into consideration biology, chemistry and physics of hair ice formation. Water, from which hair ice is formed, is contained within the wood. This porous substrate lowers the melting point and when the air temperature is sufficiently low, water freezes on the surface of the wood and ice segregation starts to extract additional water from the wood, leading to its dehydration. It transpired that a presence of a winter-active fungus was crucial for the occurrence of this phenomenon, however its actual effect is still a mystery. It appeared that the fungus did not influence the rate and the amount of formed ice, however it affected its shape, as when absent, the formed ice was crusty and stuck to the wood surface. If the air temperature remained close to the melting point, hair ice can retained its shape for hours or even days, possibly due to a recrystallization inhibitor, linked again to the presence of

the fungus. The mouth of the wood rays, where the hairs were formed, acted as a template shaping and directing growing hair ice.[151]

In case of our experiments, no physical template was used and there was no biological factors affecting the formation of water fluff (template-less "*Haareis*"). The employed experimental conditions, *i.e.*, cooling rates and temperatures, pushed the homogenous mixtures to become unstable leading to spinodal decomposition and phase separation of water from nonpolar liquids, at the same time creating highly nonequilibrium crystal-growth conditions.

As previously mentioned, some reports suggested the existence of a liquid-liquid transition (LLT) in *trans*-DCE.[152-157] We believe the conclusions in these reports to be incorrect and based on a misinterpretation of the spinodal-decomposition-induced formation of fluff-like water crystals. Our studies confirmed that these structures were the origin of light scattering observed by Turton and co-workers during their temperature-dependent optical Kerr-effect (OKE) studies on both DCE isomers.[158]

3.4 Conclusions

We carried out systematic experimental studies of crystal nucleation in two mixtures of small molecules in the presence of (a critical point for) liquid-liquid phase separation. We demonstrated that high driving force does not necessarily lead to the formation of uncontrolled polycrystalline structures.

For the first time, we observed novel asymmetric crystalline water wires (template-less "*Haareis*"). This asymmetric growth and branching is inconsistent with transport-limited growth. We were able to make these wires reproducibly without any physical template. We believe that such liquid phase-separation-induced crystal templating might be a general phenomenon with wider applicability than water ice.

We argue that previous studies on *trans*-DCE reporting the presence of liquid-liquid phase transition above its melting point were incorrect and based on a misinterpretation of the phase-separation-induced nucleation of fluff-like water structures.

4

Order Parameter of Liquid-Liquid Transition in Triphenyl Phosphite

Despite predictions of their widespread occurrence in molecular liquids[29], liquid-liquid transitions (LLTs) remain elusive and controversial phenomena. Their existence is still debated and practically all reports of polyamorphism were met with counterarguments, as the experimental verification of this phenomenon is very challenging.

One of the main research questions, which was unanswered until now, was what was the order parameter (a physical parameter) characterising LLTs. Here we present a novel approach to investigation of the LLT in TPP by combining fluorescence lifetime imaging (FLIM) and fluorescence microscopy with the use of environmentally sensitive fluorescent probes. Our results provide new evidence strongly supporting the existence of the LLT in TPP and show that its order parameter – local molecular packing associated with two known crystal polymorphs – gives rise to a change in polarity of the liquid. The LLT is associated with frustrated molecular clusters, explaining why this type of transition is so rarely observed in nature.

4.1 Introduction

As described in Section 1.1.2, the LLT in TPP (Figure 43A) takes place in the supercooled temperature region where the liquid is extremely viscous and metastable with respect to the crystalline state. This makes the nature of the observed transition debatable as some researchers argue that it is not a "true" LLT leading to another amorphous phase but an aborted crystallisation resulting in formation of a mixture of microcrystallites with a highly viscous non-transformed liquid.

As the LLT takes place between two amorphous liquid phases, any changes in structure or thermodynamic properties during the transition between these phases are expected to be subtle.[159] The order parameter (or 'reaction coordinate' of the transition) is largely an unknown but in order to predict, understand and control the LLTs, one needs to know what the order parameter refers to. There are no pertinent measurements of this important parameter but it is thought to be associated with π-stacking, packing, conformers or weak bonding.[160, 161]

Phase-contrast microscopy studies of the LLT in TPP revealed the existence of two distinctively different temperature-dependent patterns – nucleation and growth (NG) at higher temperatures and spinodal decomposition (SD) at lower temperatures. The change between these patterns was used as proof of a phase transition.[79] However, phase-contrast microscopy is limited to detection of (very small) changes in density, away from the average in the sample, and it does not provide absolute values of density, hence is not able to identify the order parameter of the LLT.

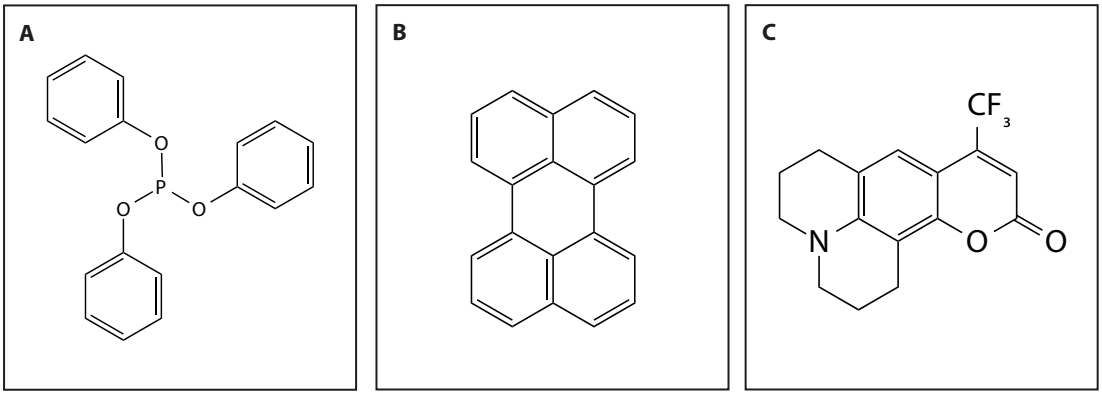

Figure 43. *The structure of triphenyl phosphite (**A**), perylene (**B**) and coumarin 153 (**C**).*

By combining the FLIM technique with selected fluorescence probes (or fluorophores) sensitive to particular properties of their environment, we expected to observe the LLT in TPP and identify its order parameter. FLIM is uniquely capable of distinguishing small differences in fluorescence lifetimes in inhomogeneous samples that would be indistinguishable in a bulk measurement and, unlike phase-contrast imaging, measures absolute values of the fluorescence lifetime. In order to accomplish our research goal, two fluorescent probes were employed in our studies, namely perylene and coumarin 153 (C153).

Perylene (Figure 43B) is a rigid, nonpolar and weakly interacting fluorescence probe and its excited-state lifetime is not expected to be affected by changes in the probe-solvent interaction. Due to extremely high viscosity of TPP in the experimental temperature range, it was expected that this probe would be only sensitive to the refractive index of its environment.

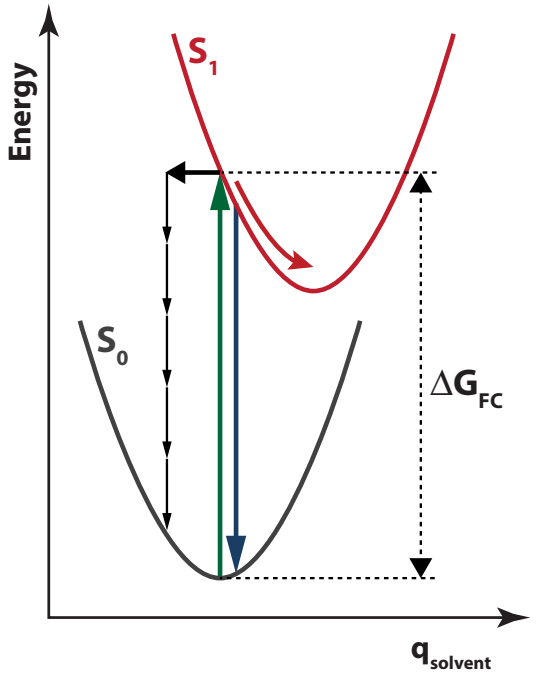

Figure 44. *Energy diagram illustrating relaxation of the C153 molecule after excitation in the first electronically excited state. The permanent electric dipole moment of C153 differs between the ground (S_o) and first (S_1) electronically excited state. The extremely high viscosity of supercooled TPP prevents solvent relaxation within the excited-state lifetime, resulting in internal conversion taking place from the unrelaxed excited state.*

One of the most common applications of C153 (Figure 43C) is the study of time-dependent solvation using the dynamic fluorescence Stokes shift measurement technique.[162-165] In our experimental temperature range, the viscosity of TPP was extremely high, ranging from 2.36×10^5 cP at 226 K to 8.57×10^6 cP at 213 K.[166] In such conditions, the solvent relaxation time is much longer than the excited-state lifetime of the fluorophore, hence the solvent is not able to adjust to the new excited-state dipole moment of C153 and fluorescence takes place from an excited state (Figure 44). However, a small Stokes shift can be observed due to a certain degree of intramolecular vibrational relaxation.

All samples were prepared at room temperature, above T_m of TPP, where solvent relaxation time was fast (sub-picosecond). This allowed the solvent (TPP) to adjust to the ground-state dipole moment of the C153 molecules before the samples were quenched to the temperatures at which the LLT took place on the timescale of hours. The electronic energy gap ($S_0 \rightarrow S_1$) in C153 is sensitive to the static dielectric constant (polarity) of the solvent. The absorption energy in the Franck-Condon region is then given by:[167, 168]

$$\Delta G_{FC} = \Delta U^0 + \frac{1}{2} B_S \left(\mu_g^2 - \mu_e^2 \right) + \frac{1}{2} B_{or} \left(\mu_g - \mu_e \right)^2 , \tag{9}$$

where ΔU^0 is the Franck-Condon absorption energy in vacuum, μ_g is the permanent dipole moment of the dye molecule in the ground state, μ_e is the permanent dipole moment of the dye molecule in the excited state, and in the Onsager cavity description:[167, 168]

$$B_\infty = \frac{2}{4\pi\varepsilon_0 r^3} \frac{\varepsilon_\infty - 1}{2\varepsilon_\infty + 1}, \quad B_S = \frac{2}{4\pi\varepsilon_0 r^3} \frac{\varepsilon_S - 1}{2\varepsilon_S + 1}, \quad B_{or} = B_S - B_\infty , \tag{10}$$

where r is the radius of the Onsager cavity, ε_0 is the permittivity of vacuum, ε_∞ is the infinite frequency dielectric constant, and ε_S is the static dielectric constant. In case of C153 these parameters are as follows: μ_g = 6.6 D, $\mu_e \approx$ 11 D,[169] and r = 3.2 Å (estimate). For ε_∞ value, either the previously measured 3.4[170] or 2.5, the square of the visible refractive index, can be used, as the final outcome was very similar. The reported measured ε_S for liquid 1 in TPP is 4.73.[170] As the reported value of ε_S for liquid 2 is unreliable due to extremely long relaxation times (~100 s), it is assumed that it is relatively

close to that of liquid 1. The calculated change in the absorption energy in the Franck-Condon region in C153 is shown in Figure 45.

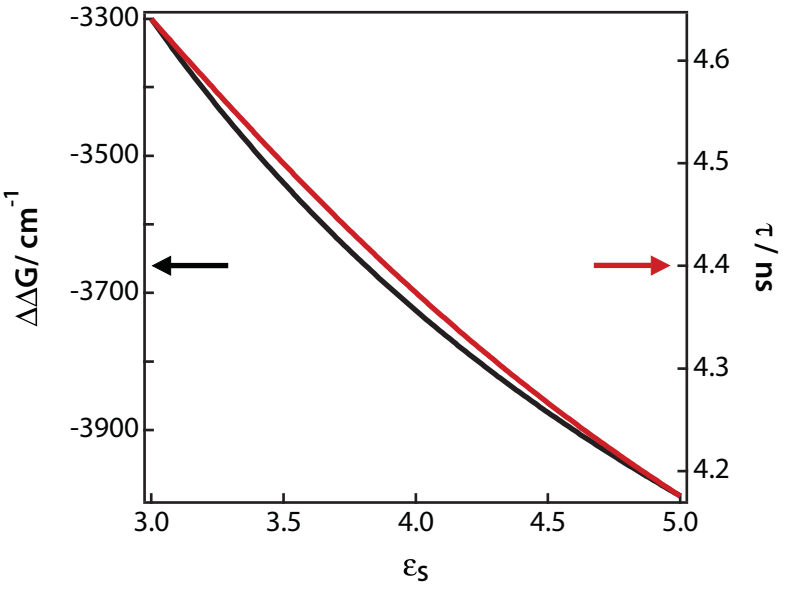

Figure 45. *Effect of TPP polarity on the energy gap and excited-state lifetime of C153. Equation (9) was used to calculate the effect of solvation on the absorption and unrelaxed fluorescence energy gap in C153 for a range of solvent dielectric constants (black curve). Equation* (11) *was used to predict the excited-state lifetime for C153, taking into consideration radiative and non-radiative decay (red curve).*

The radiative lifetime of C153 is 5.3 ns[171] but the observed lifetime is the inverse of the sum of the radiative rate and the rate of internal conversion. The rate of internal conversion is given approximately by the Jortner-Bixon expression:[168, 172]

$$k_{JB} = \frac{2\pi V^2}{\hbar\sqrt{4\pi\lambda_S k_S T}} e^{-S} \sum_{n=0}^{\infty} \frac{S^n}{n!} \exp\left\{-\left(\Delta G^0 - \lambda_S - n\hbar\omega\right)^2 / \left(4\lambda_S k_B T\right)\right\} \quad , \qquad (11)$$

where V is the internal conversion coupling constant, λ_S is the solvent reorganisation energy, S is the Huang-Rhys factor, ΔG^0 is the energy gap, ω is the angular frequency of a high-frequency accepting mode, and the sum runs over n quanta of this frequency mode.

It should be noted that in previously reported temperature-dependent fluorescence lifetime studies involving C153,[173, 174] the effect of temperature on the fluorescence transition-dipole moment had to be taken into account. The spectral shift in the

fluorescence spectrum was observed, which caused the transition dipole moment to change in proportion to

$$\frac{\int I(\nu)d\nu}{\int I(\nu)\nu^{-3}d\nu}. \tag{12}$$

However, in our experimental temperature range this effect has not been considered, as solvent relaxation in TPP is negligible on the fluorescence timescales and so are the Stokes shifts.

To calculate a reasonable non-radiative decay rate, the following values were used: V = 30 cm^{-1}, S = 0.85, and ω = 2800 cm^{-1} (corresponding to a typical CH-stretch vibrational mode). The solvent reorganization energy λ_S has been set to 3000 cm^{-1} and is considered to include the many (otherwise unaccounted for) lower frequency intramolecular modes as well as librations and β relaxation of the solvent (TPP). Figure 45 shows the excited-state lifetime of the probe as a function of the dielectric constant of the solvent. The calculated values are in good agreement with the measured values for C153 in TPP for ε_S = 3 ÷ 5. It can be safely assumed that for the experimental parameters relevant to our experiments, the excited-state lifetime scales linearly with the solvent polarity, expressed by the dielectric constant.

Taking the above into considerations, C153 was deemed to be a suitable and reliable polarity-sensitive probe for our experiments carried out on the LLT in TPP.

4.2 Results

The solutions of C153 or perylene in TPP (melting point T_m = 296 K) were quenched and subsequently held at selected temperatures in the range between 226 and 212 K.

The experimental set-up enabled for consecutive recording of phase-contrast images and FLIM maps. Recorded microscopy images and corresponding FLIM maps for selected representative temperatures are shown in Figure 46 and Figure 47. Upon cooling liquid TPP (liquid 1) transformed into another amorphous state (liquid 2) exhibiting two types of kinetics. These observations are consistent with previously reported phase-contrast studies.[79]

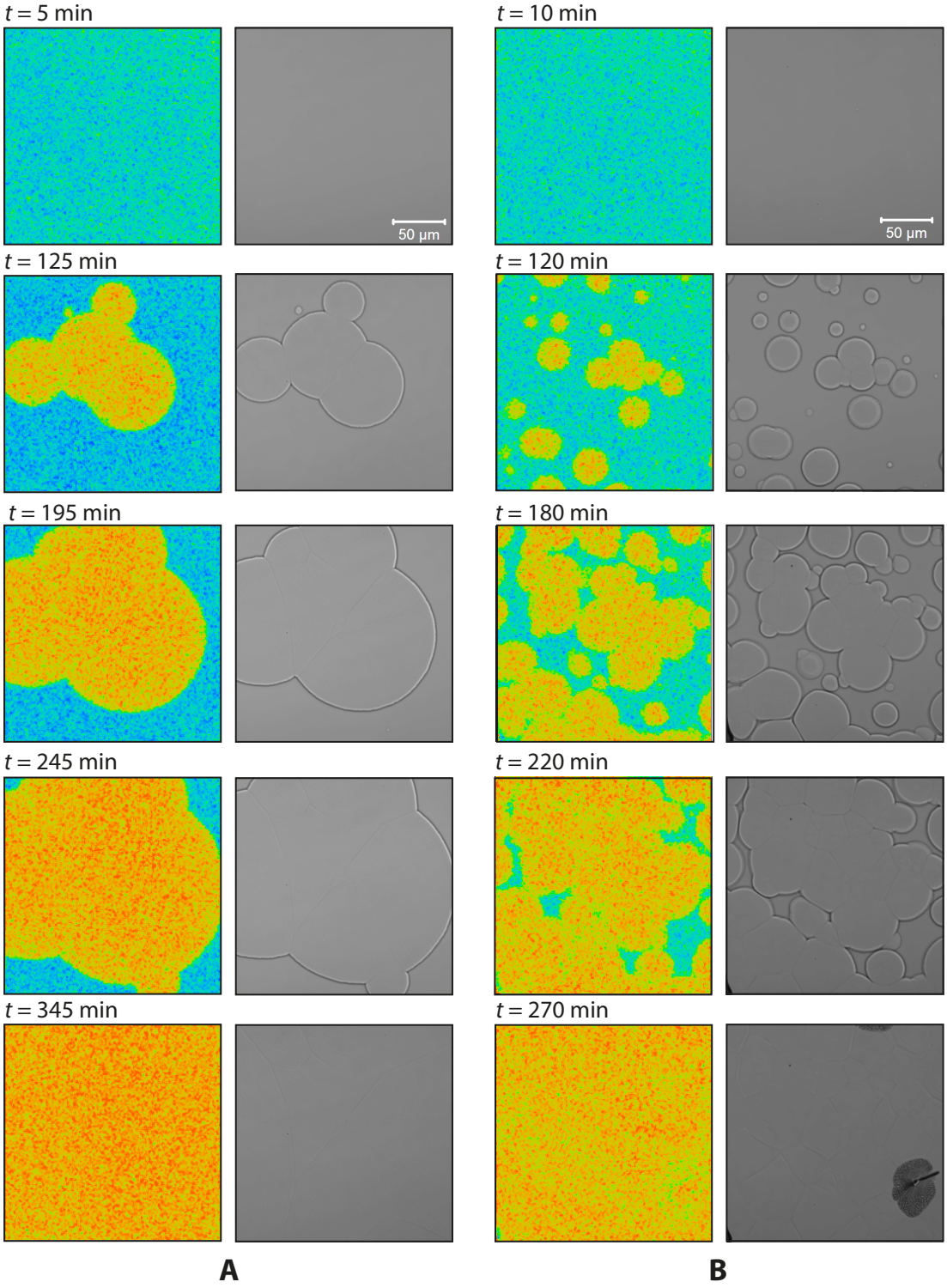

Figure 46. *Representative images of typical patterns associated with the NG-type LLT in TPP obtained by quenching to 223 K (**A**) and 220 K (**B**) for the indicated amount of time. The first and third columns show FLIM maps obtained using the probe C153 while the second and forth columns show the respective phase-contrast microscopy images (Zeiss set-up). FLIM scaling: 4.17 ns (red) to 4.52 (blue).*

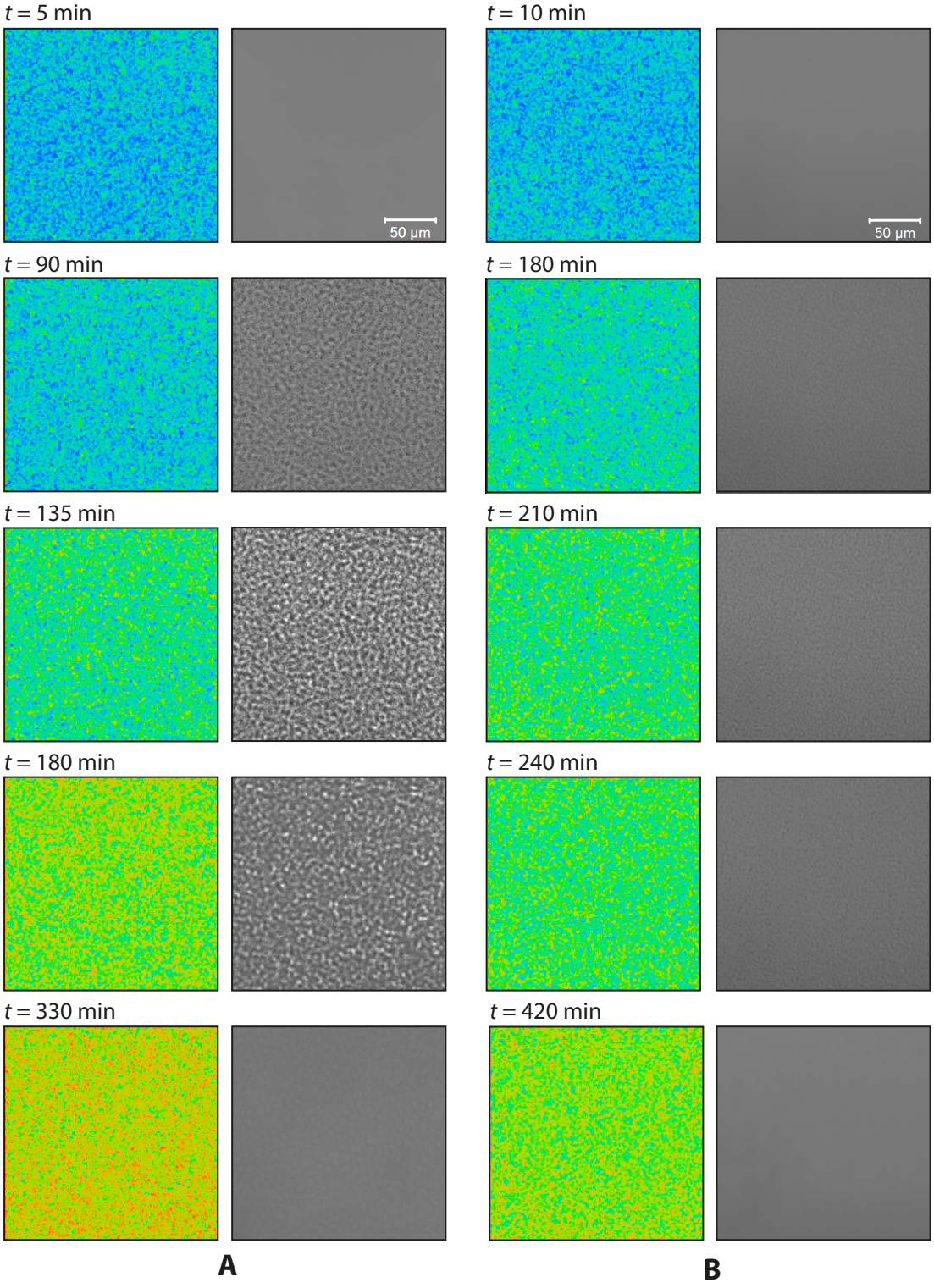

Figure 47. *Representative images of typical patterns associated with the SD-type LLT in TPP obtained by quenching to 215 K (**A**) and 213 K (**B**) for the indicated amount of time. The first and third columns show FLIM maps obtained using the probe C153 while the second and forth columns show the respective phase-contrast microscopy images (Zeiss set-up). FLIM scaling: 4.15 ns (red) to 4.42 (blue).*

The experiments carried out on TPP in the temperature range between 226 K and 215.5 K resulted in observation of liquid 2 nucleating in the form of spherical droplets in liquid I. The droplets grew with time until the entire system fully transformed into liquid 2 (NG-type kinetics).

When TPP was quenched to 226 K, the nucleation process was immediately followed by formation of crystallites embedded in liquid 2 droplets (see Figure 48a). The fluorescence lifetime of these crystalline regions (crystal 2) differed significantly from the lifetime of the thermodynamically stable crystalline state (crystal 1), acquired at the same quenching temperature, and at the same time was very similar to the lifetime observed in liquid 2 at a slightly lower temperature (see Figure 60).

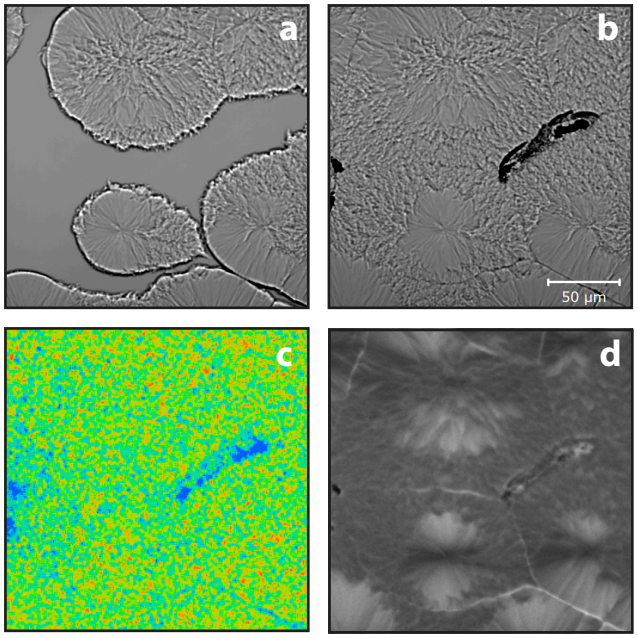

Figure 48. *A second crystalline phase of TPP formed at 226 K. All four images were taken at the same scan area. (**a**) DIC image at the approximate halfway point in the transition. Crystalline features are clearly visible inside and at the edges of the nucleating droplets of liquid 2. (**b**) DIC image after full transformation. (**c**) FLIM map obtained using the probe C153. Scaling: 4.1 (red) to 4.3 (blue). (**d**) Fluorescence intensity. Scaling: grey ~2,500/pixel, white ~3,300/pixel.*

The experiments carried out below 215.5 K (above the glass transition temperature of liquid 1 at ~205 K), showed the SD-type kinetics. After quenching of liquid 1, density fluctuations grew slowly, but continuously, until the system became homogeneous.[79]

The lower the temperature, the longer it took for the transformation to take place, *e.g.*, about 220 minutes at 220 K and over twice as long at 212 K.

Figure 49 shows typical patterns associated with the NG-type LLT and the SD-type LLT in TPP. FLIM maps, obtained using the probe C153, revealed that liquid 1 is characterised by shorter average lifetimes and longer average lifetimes are associated with liquid 2 in both types of transitions.

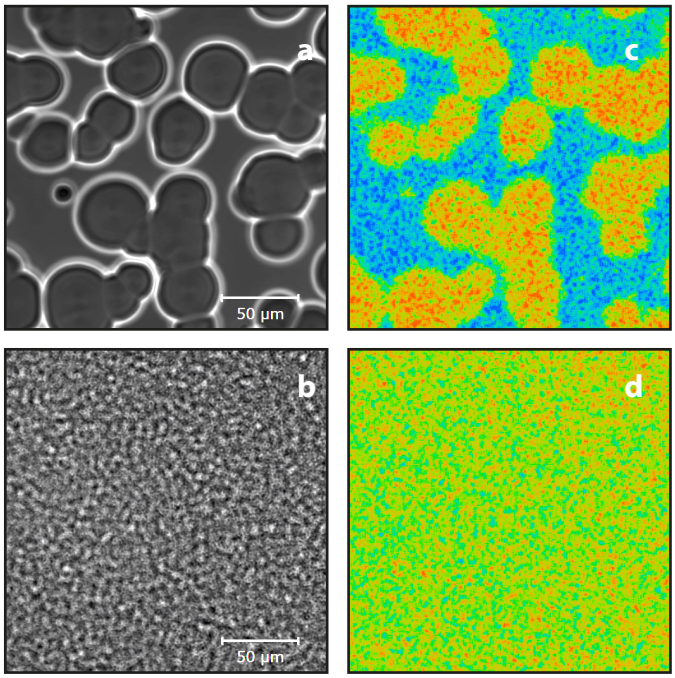

Figure 49. *Representative patterns associated with the LLT in TPP. Top-row images show the NG-type LLT observed in TPP held at 220 K after about 170 minutes from the quench. Bottom-row images show the SD-type LLT in TPP held at 213 K for about 325 minutes. (**a**, **b**) Phase-contrast microscopy images (Zeiss set-up). (**c**, **d**) FLIM maps obtained using the probe C153. Scaling: 4.21 ns (red) to 4.46 ns (blue).*

All FLIM maps obtained using C153 and perylene were converted into lifetime distributions as described in Section 2.6.3.

Figure 50 - Figure 52 show distributions obtained from FLIM maps recorded using the probe C153 at higher temperatures (226 – 215.5 K) at which TPP undergoes the NG-type transitions. At these temperatures, an initial distribution of lifetimes, associated with liquid 1, gradually transformed into a new distribution (liquid 2) characterised by a shorter average fluorescence lifetime.

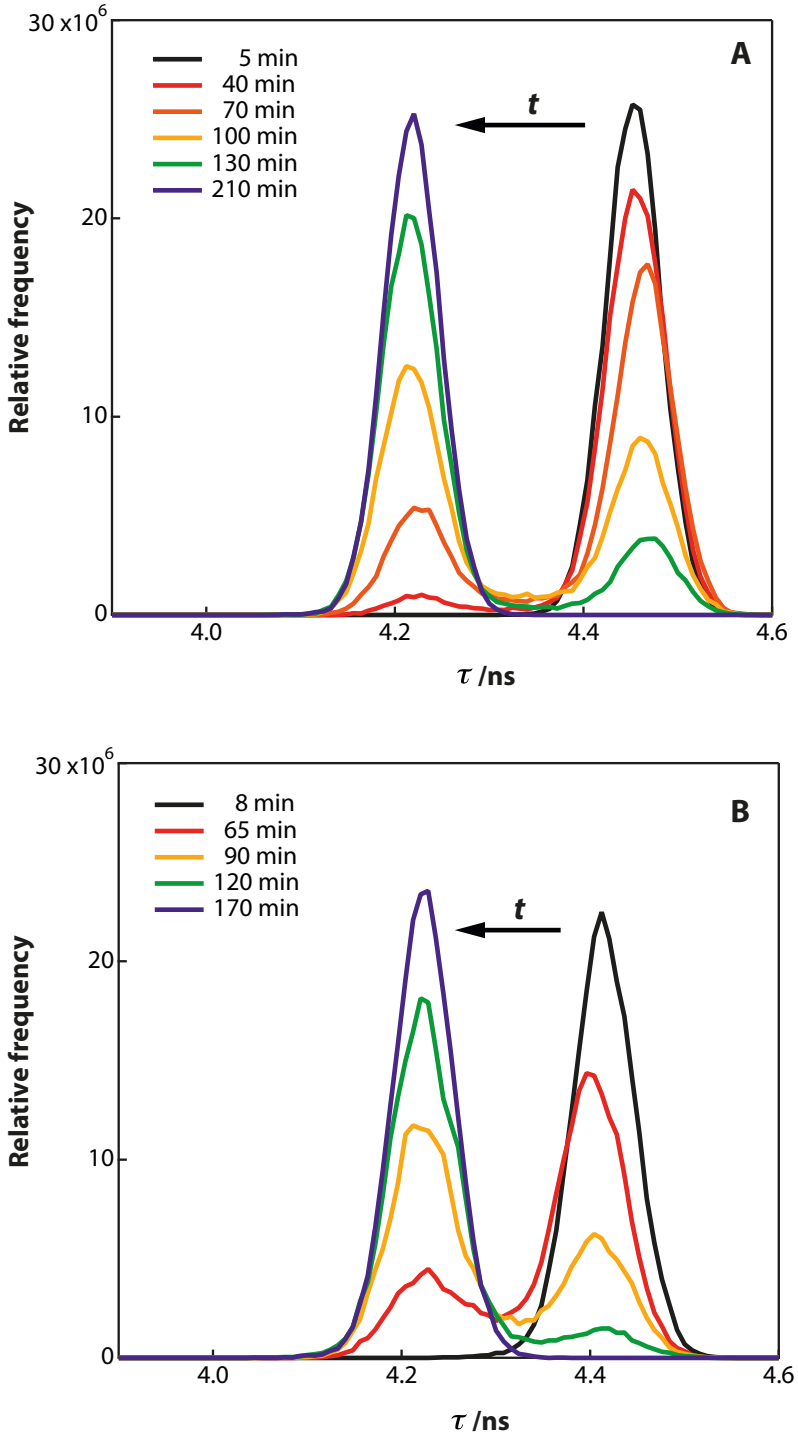

Figure 50. *Normalised fluorescence lifetime distributions of C153 in TPP quenched to 226 K (**A**) and 224.5 K (**B**). The colour coding and the arrows show the progression of the transition since the quench.*

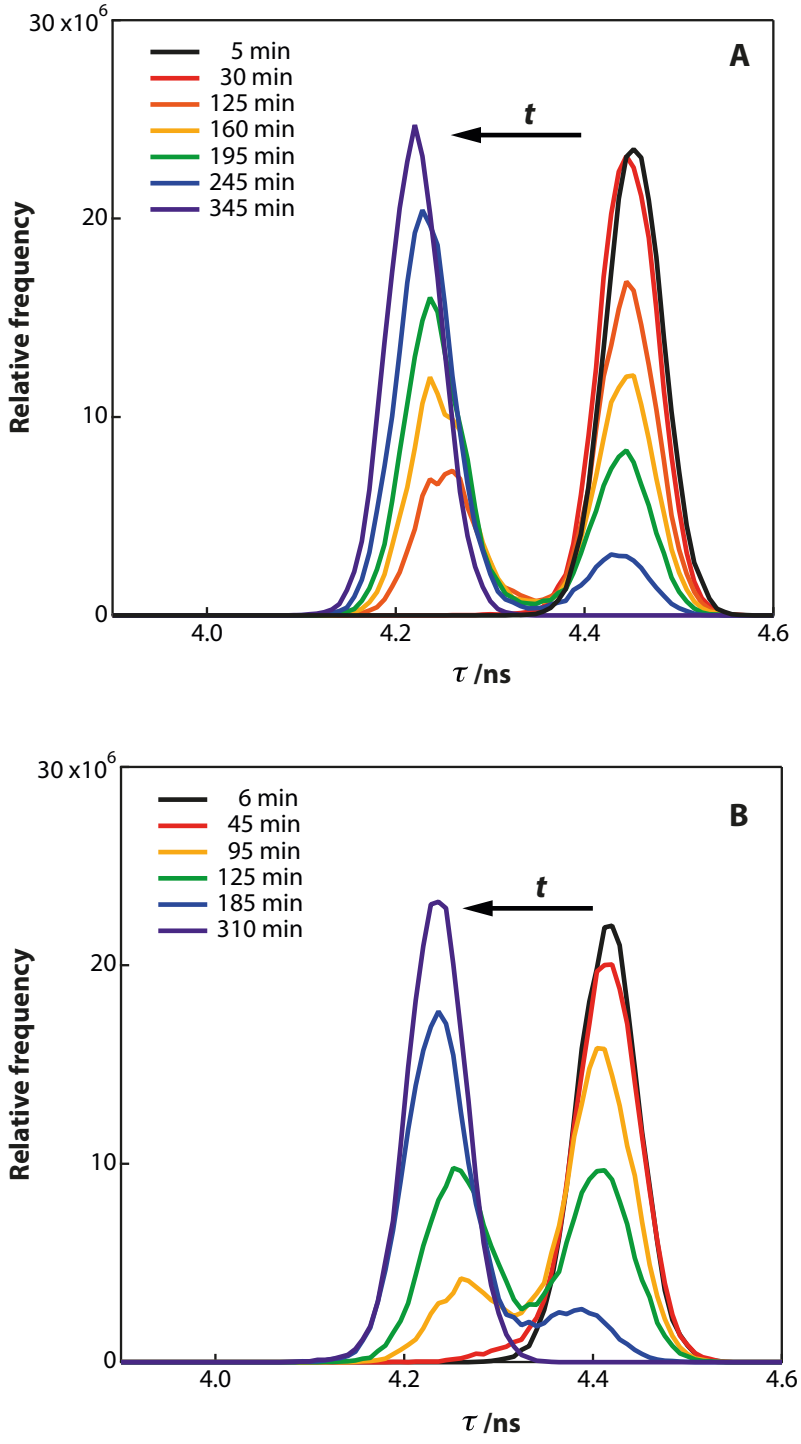

Figure 51. *Normalised fluorescence lifetime distributions of C153 in TPP quenched to 223 K (**A**) and 221.5 K (**B**). The colour coding and the arrows show the progression of the transition since the quench.*

It can be observed that, with exception of the transition at 218.5 K, all these FLIM maps show two distinct fluorescence lifetime distributions (two-state behaviour).

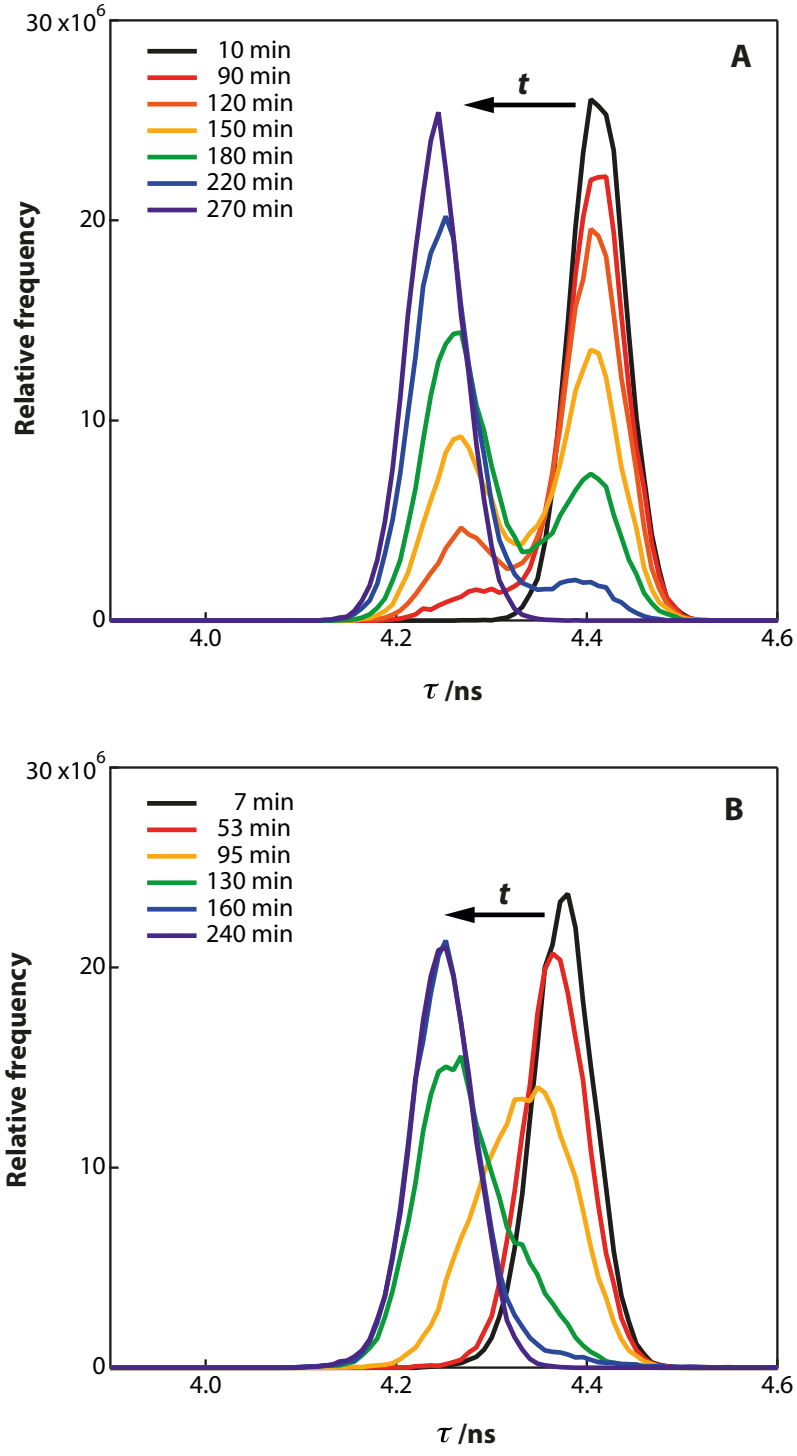

Figure 52. *Normalised fluorescence lifetime distributions of C153 in TPP quenched to 220 K (**A**) and 218.5 K (**B**). The colour coding and the arrows show the progression of the transition since the quench.*

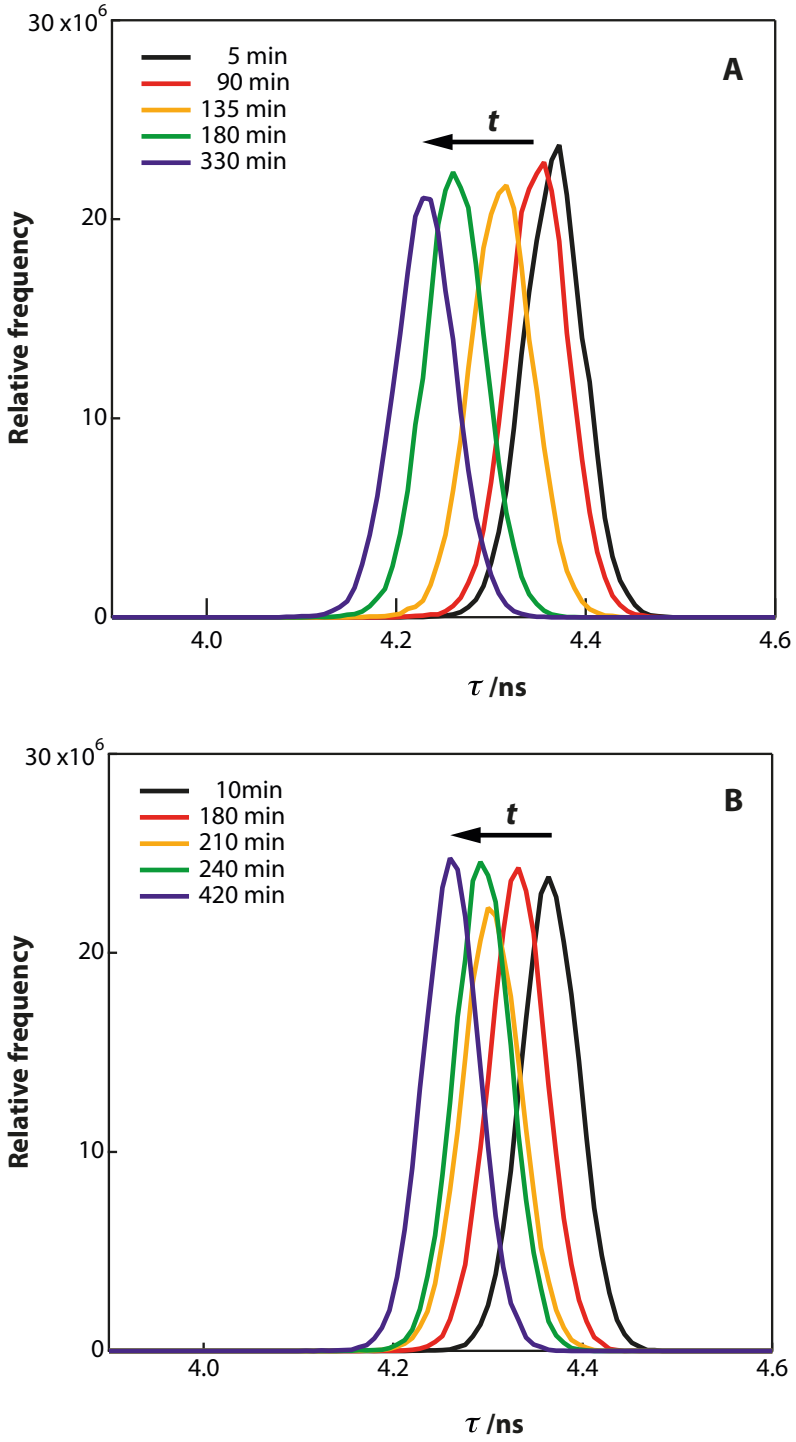

Figure 53. *Normalised fluorescence lifetime distributions of C153 in TPP quenched to 215 K (**A**) and 213 K (**B**). The colour coding and the arrows show the progression of the transition since the quench.*

Figure 53 and Figure 54 show distributions obtained from FLIM maps recorded using the probe C153 at lower temperatures (215 – 212 K) at which TPP undergoes the SD-type transitions. Unlike the two-state behaviour observed at higher temperatures, in the

SD-type transitions an initial distribution of lifetimes (liquid 1) gradually shifts towards shorter average fluorescence lifetime values (liquid 2). The correlation length of the fluctuations in the SD-type transitions[79] is ~ 1 μm and the fluctuations seen in phase-contrast images for this type of transition (*e.g.*, Figure 49b) are easily resolvable by FLIM.

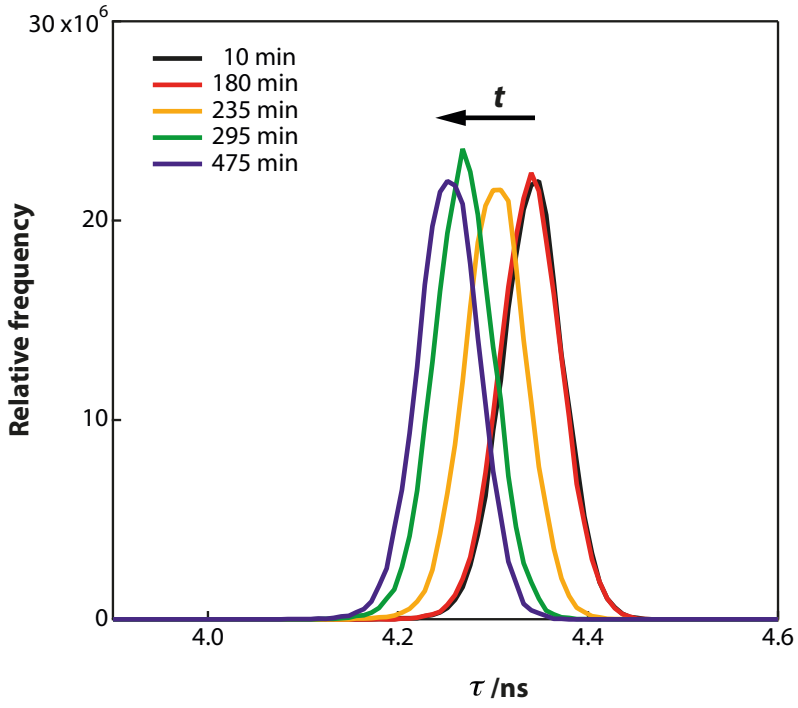

Figure 54. *Normalised fluorescence lifetime distributions of C153 in TPP quenched to 212 K. The colour coding and the arrows show the progression of the transition since the quench.*

Figure 55 shows the comparison between the lifetime distributions obtained using the probes C153 and perylene in TPP undergoing NG-type and SD-type LLT at three different temperatures.

It can be seen that in case of the NG-type transformation, the distributions obtained using the probe C153 were clearly distinct. The distributions obtained using perylene overlapped, however analysis showed the same two-state behaviour.

In case of SD-type transformation, there was only one distribution shifting gradually towards shorter average lifetime values as the transformation progressed.

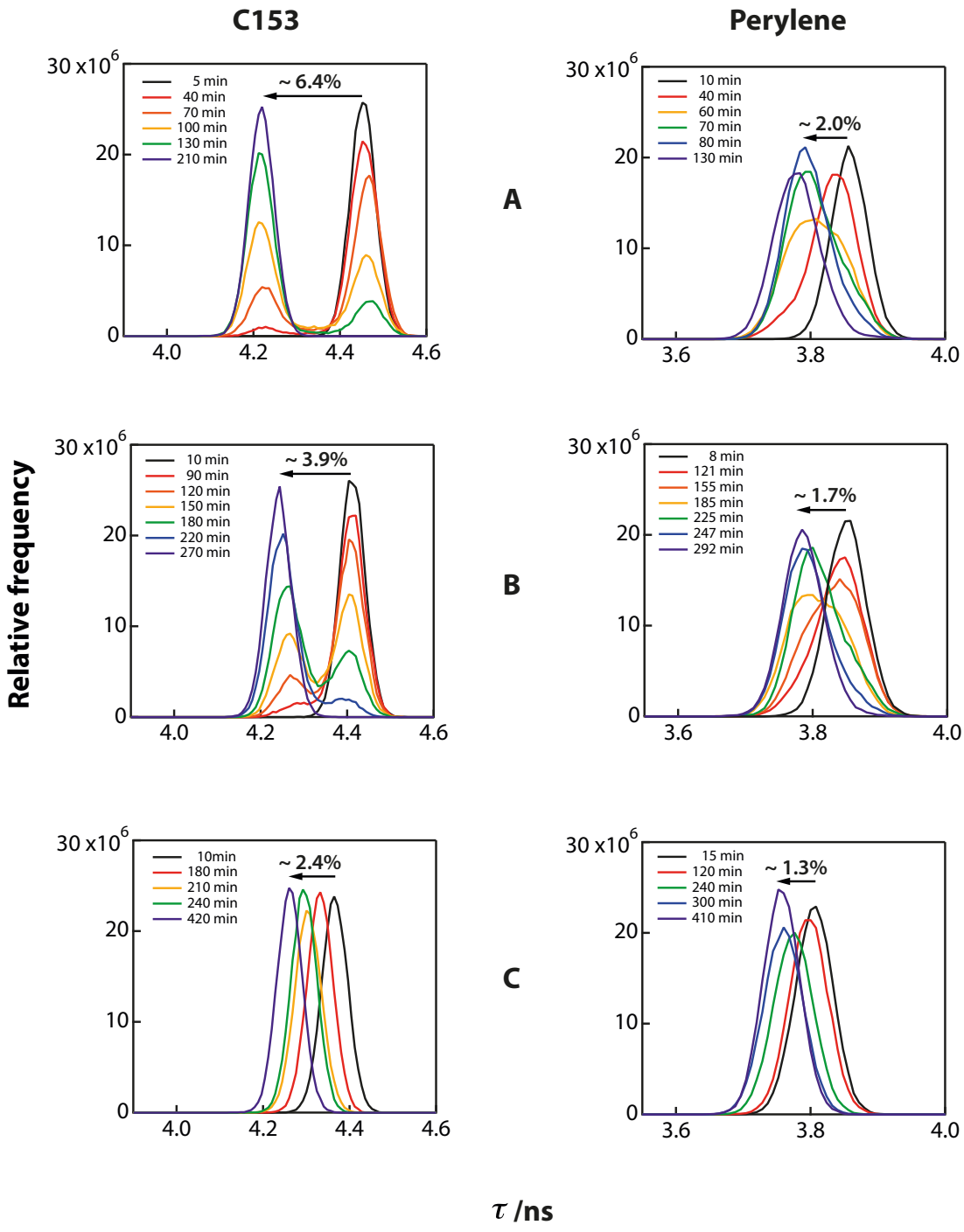

Figure 55. *Normalised fluorescence lifetime distributions of the probe C153 (left column) and perylene (right column) in TPP undergoing the NG-type LLT at 226 K (**A**) and 220 K (**B**) and the SD-type LLT at 213 K (**C**). Colour coding and the arrows indicate time progression since the selected temperature has been reached.*

To model the molecular scale fluctuations, the fluorescence lifetime distributions obtained at all experimental temperatures using the probe C153 were fitted to a Gaussian distribution. All initial (liquid 1) and final (liquid 2) lifetime distributions were fitted using one Gaussian distribution. The same applied to all lifetime distributions obtained for the SD-type transformation at 215 K, 213 K and 212 K.

All NG-type transformation data collected during the transition could only be satisfactorily fitted with two Gaussian distributions. These two distributions were characterised by distinct average fluorescence lifetimes.

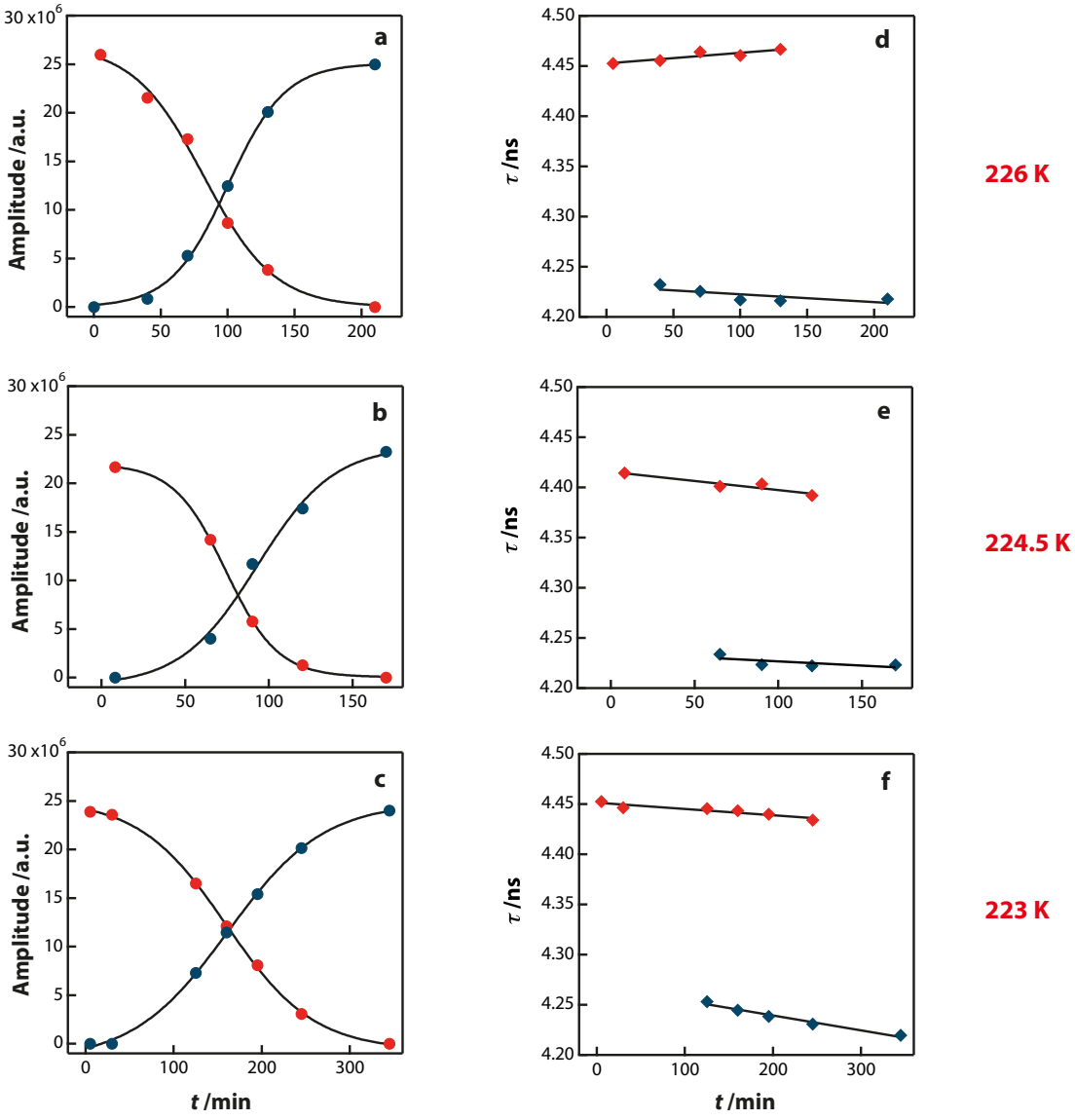

Figure 56. *Temporal change of the amplitude (left column) and the average fluorescence lifetime (right column) of the probe C153 in TPP obtained by Gaussian fitting to the lifetime distributions shown in Figure 50 and Figure 51.*

Figure 56 and Figure 57 show two fitting parameters: the temporal change of the amplitude and the average fluorescence lifetime of the probe C153 in TPP undergoing the NG-type transition. Figure 58 shows the same fitting parameters for the SD-type transformation.

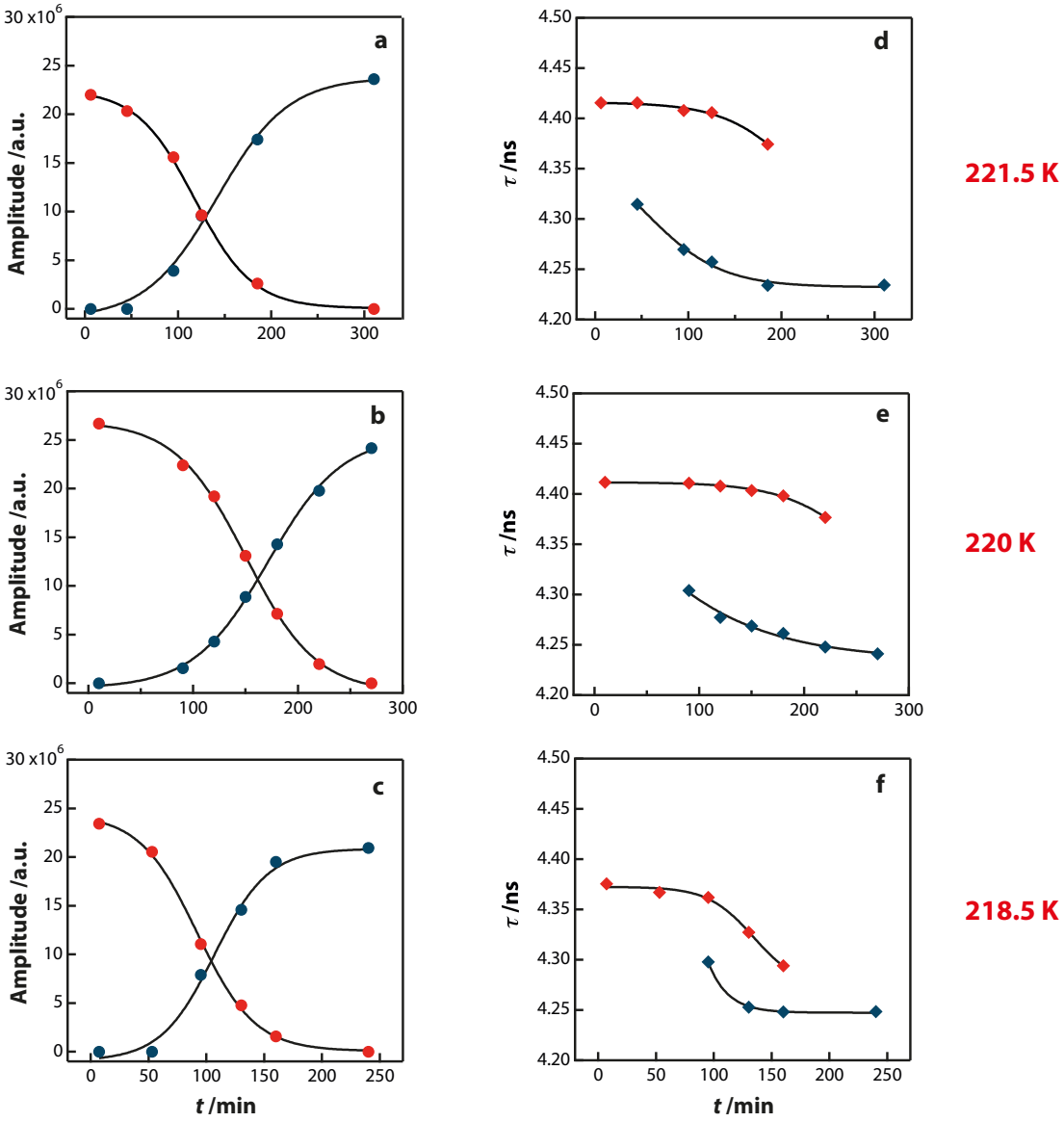

Figure 57. *Temporal change of the amplitude (left column) and the average fluorescence lifetime (right column) of the probe C153 in TPP obtained by Gaussian fitting to the lifetime distributions shown in Figure 51 and Figure 52.*

In the case of the NG-type LLT, the amplitude of the initial distribution (liquid 1) gradually decreased accompanied by the gradual increase of the amplitude of the new

distribution corresponding to liquid 2. During the SD-type LLT, the amplitude of the single distribution remained practically constant.

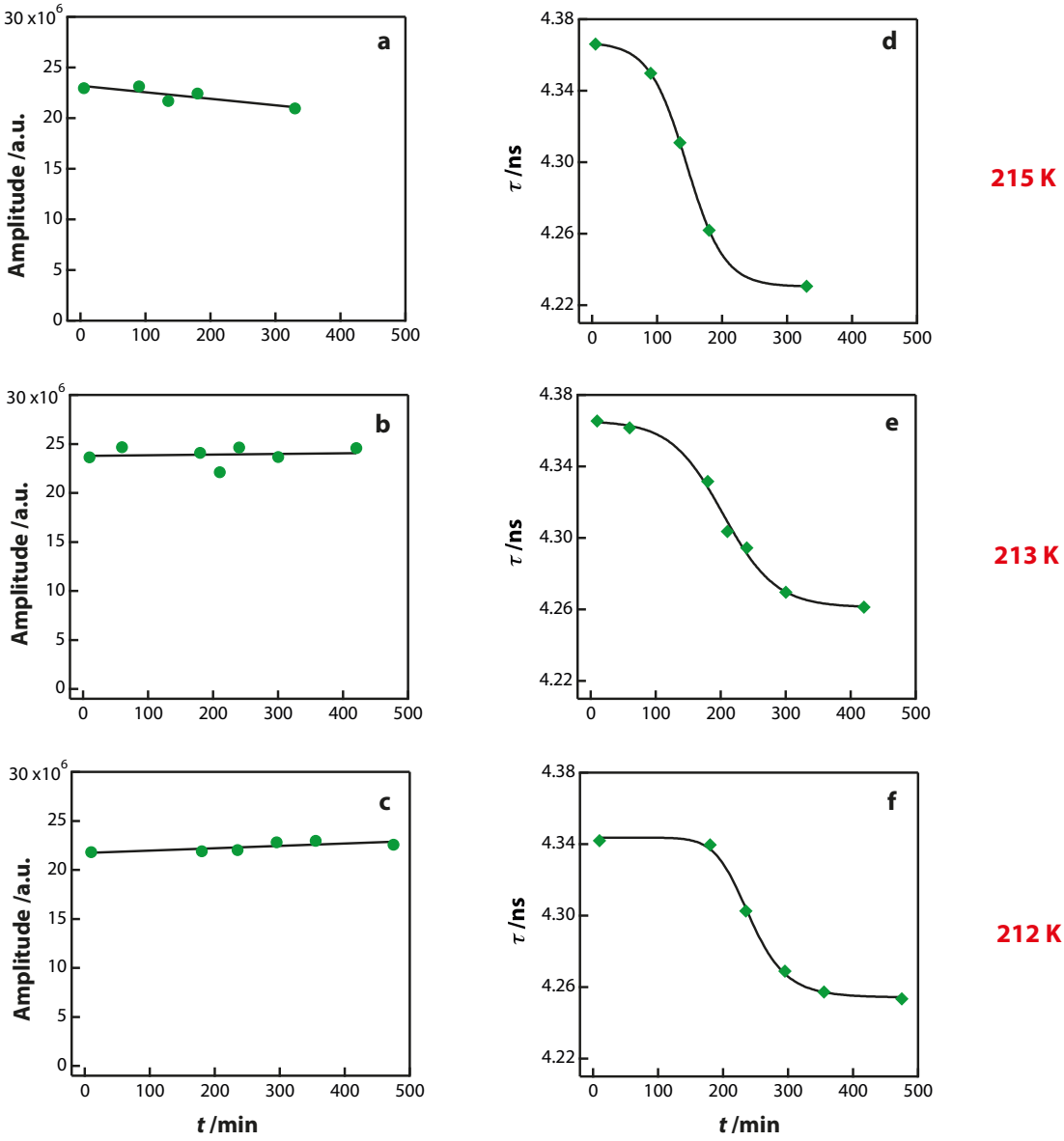

Figure 58. *Temporal change of the amplitude (left column) and the average fluorescence lifetime (right column) of the probe C153 in TPP obtained by Gaussian fitting to the lifetime distributions shown in Figure 53 and Figure 54.*

The average fluorescence lifetimes of two distributions seen in the NG-type LLT were nearly time-independent, while in the SD-type LLT the average fluorescence lifetime followed the sigmoid trend characteristic for this type of transition.

The observed change from a double-peaked distribution at higher temperatures (NG-type transition) to a single-peaked but shifting distribution at lower temperatures (SD-type transition) characterises phase transitions near a critical point.[29, 84]

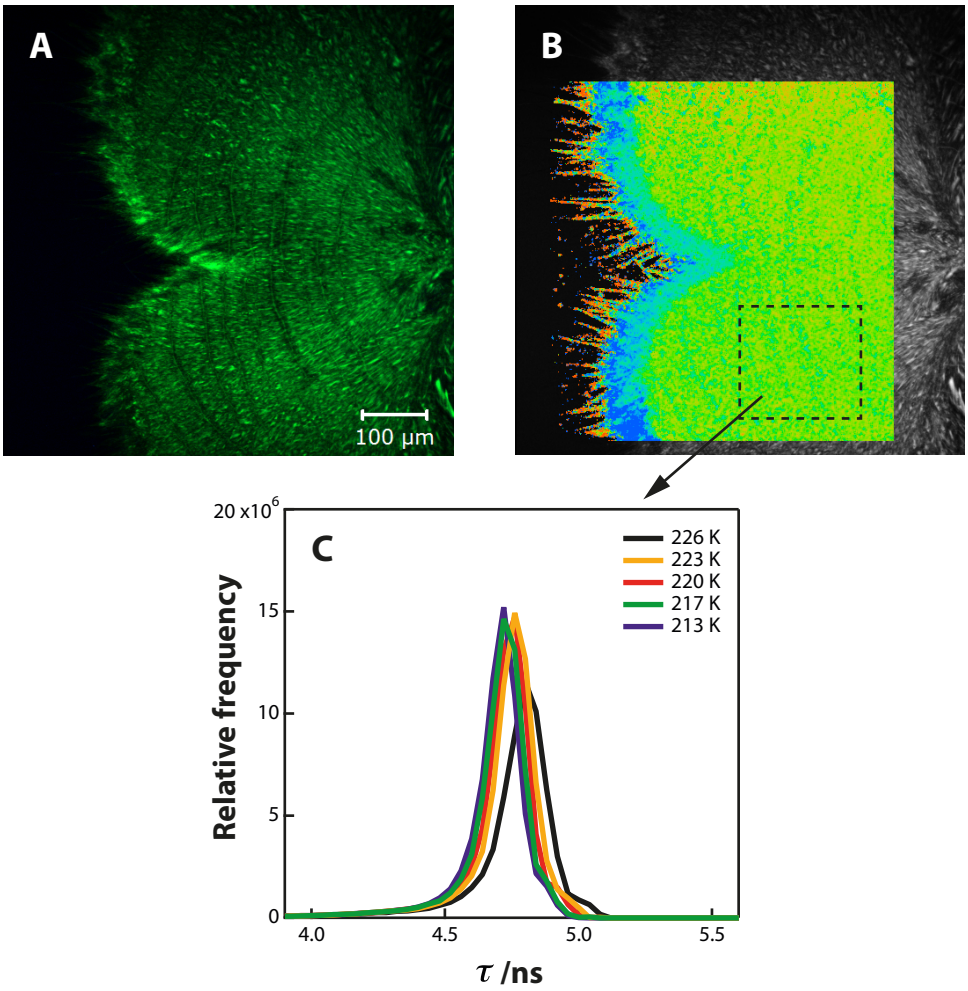

Figure 59. *C153 fully incorporated into crystal 1 of TPP at 220 K. (**A**) Fluorescence intensity. (**B**) Colour-coded FLIM map superimposed on the intensity image. FLIM scaling ranges from 4.0 (red) to 5.5 ns (blue). The black-coloured area in the left part of the images is air. (**C**) Normalised fluorescence lifetime distributions of the probe C153 in crystal 1 of TPP obtained from FLIM maps recorded from the area similar to this marked with a dashed square. Colour coding indicates temperatures at which the measurements were taken.*

As mentioned before, the nature of liquid 2 remains very controversial. Some researchers strongly pursue a theory that, rather than being a second liquid phase, liquid 2 is a metastable mixture of crystallites and highly viscous liquid.[67, 77] To explore this hypothesis, we carried out a series of experiments on the thermodynamically stable crystalline state (crystal 1) prepared, as described in Section 2.6.6.2, using the probe C153.

We found that C153 fully incorporated into the crystal lattice of TPP as fluorescence was observed throughout the crystal 1 (see Figure 59A). The FLIM map in Figure 59(b) shows that the fluorescence lifetime was constant across the whole scan area and it was longer than liquid 1 (4.7 – 4.8 ns), apart from the blue region at the edges of crystal 1 (~5.5 ns) where the probe was exposed to air.

The FLIM maps, acquired at selected temperatures, were converted into normalised fluorescence lifetime distributions, which were thereafter fitted to a single Gaussian distribution to determine the average fluorescence lifetime values for crystal 1.

The average fluorescence lifetimes of distributions associated with liquid 1 (obtained when the selected quench temperature was reached), liquid 2 (at the end of the experiment) and crystal 1 were plotted as a function of quenching temperature and shown in Figure 60.

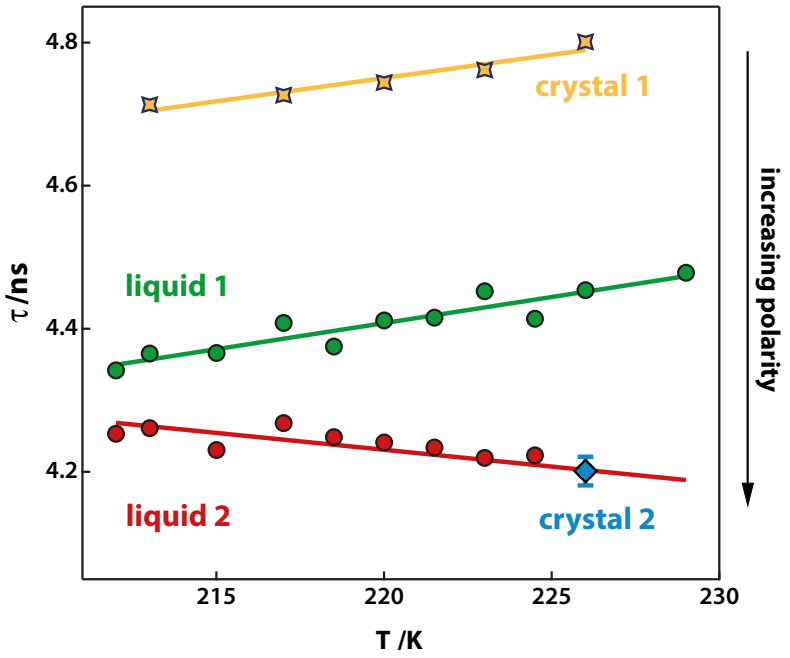

Figure 60. *Temperature dependence of the average fluorescence lifetime of the probe C153 in different phases of TPP – crystal 1, liquid 1, liquid 2 and crystal 2 (a blue diamond at 226 K). The error bar (±1σ), determined on the basis of three independent experimental results, is representative for all data points.*

The average fluorescence lifetime of liquid 1 and crystal 1 became shorter with the temperature decrease while the lifetime of liquid 2 showed the opposite trend.

4.3 Discussion

As mentioned before, due to its rigid structure and nonpolar weakly interacting character, the excited-state lifetime of perylene is not expected to be caused by the interaction with the solvent. The viscosity of TPP in our experimental temperature range is extremely high (10^6 – 10^7 cP),[166] resulting in exceedingly slow molecular diffusion. For that reason no changes in the rates of radiationless decay and no preferential partitioning[175] of the probe molecules over phases on the time scales of the experiments are expected. Taking the above into consideration, the relationship between the fluorescence lifetime and the physical parameters can be described by the Strickler-Berg formula (Equation 8), which predicts that the fluorescence lifetime is inversely proportional to the square of the refractive index ($\tau_0 \propto n^{-2}$). The observed change of the excited-state lifetime in perylene/TPP during the transition from liquid 1 to liquid 2 at 220 K was 1.7%. Hence, it can be estimated that the corresponding refractive index change was 0.9%, which is consistent with the reported estimated refractive indices of 1.634 and 1.655 respectively for liquid 1 and liquid 2 based on density measurements at 220 K.[82]

C153 is commonly used in fundamental studies exploring the influence of the environment's microviscosity and polarity on the fluorescent properties of a selected molecule.[176-179] As mentioned above, during our experiments the viscosity of TPP was extremely high, therefore viscosity, diffusion and dynamic solvation did not play a role during the ~ 4.5 ns lifetime of the excited state.

All C153/TPP samples were prepared at room temperature (where the solvent relaxation times are on the order of subpicoseconds) and thereafter quenched to the experimental temperatures. This protocol kept the probe solvated in the ground state for the duration of the experiments. In this case, non-radiative decay, known to be dominated by internal conversion from S_1 to S_0,[174] was controlled by the free-energy gap in the Franck–Condon region. This resulted in a fluorescence lifetime that was very nearly linearly dependent on the dielectric constant of the medium within the range of $\varepsilon_S = 3–5$ as discussed in Section 4.1.

Temperature-dependent changes in the probe C153 lifetime reflect changes in the static dielectric constant (or "polarity") of TPP, hence we conclude that the LLT in TPP is linked to a change in polarity. As can be expected, crystal 1 and liquid 1 become more

polar as the temperature decreases, however behaviour of liquid 2 is anomalous as it becomes less polar.

It has been suggested that liquid 2 (also called the glacial phase) is composed of untransformed supercooled liquid (liquid 1) and crystallites of the stable crystalline phase (crystal 1).[67, 77] In this case the fluorescence lifetime of the probe C153 in liquid 2 should have the value in between that of liquid 1 and crystal 1. However, this is not observed, as the lifetime of liquid 2 is shorter than the lifetime of liquid 1 and crystal 1.

When TTP was quenched and held at 226 K, the growing droplets of the new phase exhibited distinct crystalline appearance. The fluorescence lifetime of the probe C153 in this new phase was faster than the lifetime obtained at this temperature in the thermodynamically stable crystalline state (crystal 1). Its value was what would have been expected in liquid 2 by extrapolating the lower temperature data (see Figure 60). We identify this phase as a different crystalline phase of TPP - crystal 2 - characterised by molecular ordering resembling that of liquid 2. We further suggest that this molecular ordering frustrated the formation of crystal 1. This is consistent with X-ray data suggesting a "crystallite" size of about 30–50 Å[77] if this is interpreted as the size of a frustrated molecular cluster.[180] Due to the limitations of our experimental techniques, we are unable to determine whether crystal 2 nucleated directly from liquid 1 or rapidly from liquid 2 following an LLT from liquid 1. The latter explanation seems more logical and consistent with the LLT occurring in liquid Si and Ge.[32, 181, 182]

The thermodynamically stable crystals of TPP (crystal 1) can be easily obtained by cold crystallisation of liquid 1 described in Section 2.6.6.2. Crystal 1 has needle-like shape and a hexagonal crystal lattice in which each molecule assumes an approximately pyramidal shape.[183] However, Golovanov *et al.* reported that monoclinic prismatic crystals of TPP can be obtained from an ionic liquid, 1-butyl-3-methylimidazolium bromide, by rapid cooling of the solution.[183] These two polymorphic modifications differ in the crystal packing and the position of the phenoxy substituents, which in the monoclinic modification is twisted away from the base of the pyramid (see Figure 61). As the monoclinic polymorph has only been observed nucleating from a highly polar ionic liquid strongly suggests that its critical nucleus is more polar than that of the hexagonal polymorph. X-ray diffraction studies show orientational correlations between phenyl rings on adjacent TPP molecules in the supercooled liquid[184] consistent with local clusters similar, but not identical, to the monoclinic crystal. Similarly, NMR spectroscopy on TPP has suggested that liquid 2 is associated with parallel alignment of the molecules in clusters involving only a few

molecules.[185] This is consistent with a reduction seen by X-ray diffraction studies of the P–P distance on neighbouring molecules upon going from liquid 1 to 2 at 215 K.[180]

As can be seen in Figure 60, as the temperature increases, liquid 2 becomes more polar. This could be explained by two liquid phases of TPP having distinct and temperature-dependent fractions of the hexagonal- like and monoclinic-like local structures as described by the two-state model.[95] This model is similar to the proposed temperature-dependent fractions of a four-coordinated low-density liquid and less structured high-density liquid in liquid water. [32, 33, 186-190]

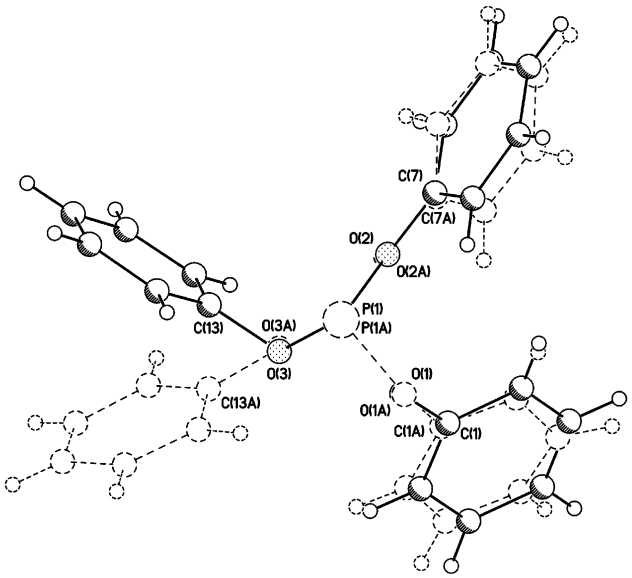

Figure 61. *Superimposed crystal polymorphs of TPP. Solid lines correspond to monoclinic modification, while dashed lines correspond to hexagonal polymorphic modification.* [183]

4.4 Conclusions

We observed and confirmed that depending on the temperature at which supercooled TPP is held, the initial phase being liquid 1, gradually transforms into a new phase – liquid 2 – either following the NG-type or SD-type kinetics. This change in behaviour is consistent with the previously reported phase-contrast microscopy studies.[84] It confirms and proves that the observed phenomenon is an LLT.

For the first time FLIM technique was applied to study the phenomenon of the LLT in TPP. Two florescent probes – coumarin 153 and perylene – were selected for this study based on their specific environmental sensitivity. We find that local molecular packing,

giving rise to a change in the polarity of the liquid, is the order parameter of the LLT in TPP. We conclude that this local molecular packing is associated with molecular packing seen in the two known crystal polymorphs and therefore the LLT in TPP is a phase transition between two liquid phases characterised by different degree of twisting of one of the phenoxy groups[183], not an "aborted crystallisation". These two liquid phases exhibit either more hexagonal or monoclinic local ordering effectively resembling corresponding crystal polymorphs.[191]

Our findings also explain why LLTs appear to be so rare despite predictions that they should be common in all molecular liquids.[3] If LLTs lead to liquid phases that, due to their frustrated configuration, effectively inhibit the formation of thermodynamically more stable crystal phases, then it implies that these phases have different local configuration. In case of TPP, liquid 2 is more polar than liquid 1 leading to visible macroscopic separation during transformation. This visible physical separation between two distinctively different liquid phases may be rare even if the above-mentioned predictions are correct.

5

A Liquid-Crystal Phase Frustrating Crystallisation

Locally favoured structures frustrating crystallisation are essential to link the phenomena of supercooling, formation of glasses and liquid-liquid transitions. Here we use various imaging and spectroscopic techniques, including phase-contrast microscopy, polarisation microscopy, confocal Raman microscopy and fluorescence lifetime imaging (FLIM), to show that the previously reported liquid-liquid transition (LLT) in supercooled *n*-butanol[29] is in fact a transition from an isotropic liquid to a rippled lamellar liquid crystal (LC) phase. LC phases are soft-matter systems thought as states "in-between" the liquid and the crystalline states. However, in case of *n*-butanol, an LC phase inhibits transformation to the thermodynamically most stable crystal state. Our results demonstrate a form of geometric frustration in which local interactions give rise to partially ordered states that are incompatible with the thermodynamically more stable crystalline states. This frustrated phase, being a template for similar type of liquid ordering, is likely to play an important role in supercooling and liquid-liquid transitions in other molecular liquids.

5.1 Introduction

A liquid should, in principle, crystallise on cooling. It is well known that this process may occur in a number of steps, which result in increased order. For example, on cooling an isotropic liquid may initially form a nematic LC characterised by a partial orientational ordering. Further cooling may lead to the formation of smectic LC phases introducing partial translational ordering. Supercooling of the isotropic liquid below the liquid-LC transition is irrelevant as due to structural similarity between the phases, the interfacial energy required to establish an interface between two phases, is very low.

As described in detail in Section1.1.3, supercooled *n*-butanol was reported to undergo an LLT occurring between two physically different phases – a supercooled liquid (liquid 1) and the apparently amorphous "glacial phase" (liquid 2).[29] As it was the case with TPP (Section 1.1.2), the existence of this type of transition in *n*-butanol is highly controversial and is dismissed by many as aborted crystallisation leading to a mixed state composed of supercooled liquid and crystallites.[87-89]

Here we present the results of our studies aimed at understanding the origin and nature of the apparently amorphous "glacial" state observed in supercooled *n*-butanol and experimental verification of the existence of the associated LLT using various imaging and spectroscopic experimental techniques.

5.2 Results

N-butanol (1-butanol) is a glass-forming liquid which has a melting temperature of T_m = 183.4 K and undergoes a glass transition at a glass-transition temperature of T_g = 118 K.[85] Figure 62 show typical patterns observed with phase contrast microscopy when *n*-butanol was quenched and annealed in the temperature range between 120 and 140 K (below T_m). The new phase nucleated in the form of spherical droplets, which continued to grow until the whole sample was transformed. With decreasing temperature, the number of nucleation sites increased rapidly as expected for a homogeneous nucleation process (Figure 47 and Figure 64). However, the growth rate of the nucleating droplets decreased with lowering temperature due to the increase in viscosity resulting from approaching the glass transition temperature. These observations were consistent with previous reports, which assigned them to a polyamorphic LLT.[29, 85]

On repeating of the experiment with the same sample, the droplets nucleated in random places showing that heterogeneous nucleation did not play a major role.

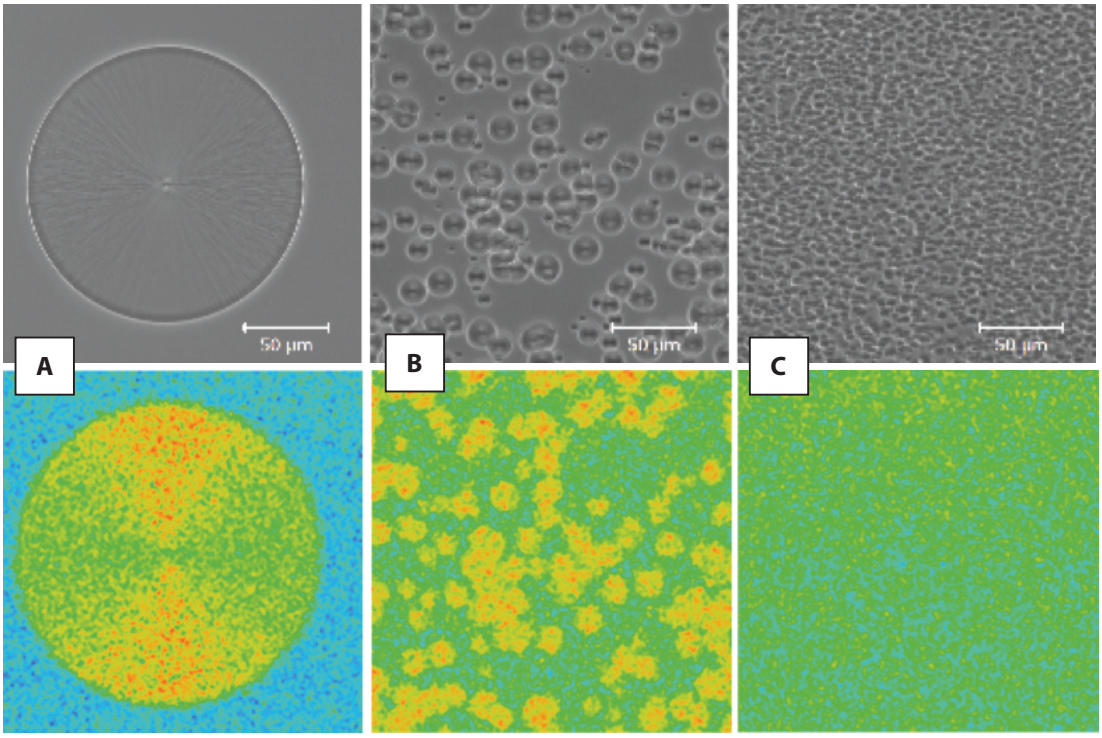

Figure 62. *Phase-contrast microscopy images (Zeiss set-up) (**top**) and FLIM maps obtained using the dye coumarin 153 (**bottom**) of the transition occurring in n-butanol quenched to (**A**) 140 K (56 minutes), (**B**) 130 K (80 minutes), and (**C**) 128 K (83 minutes). Both sets of data were taken at the approximate halfway point in the transformation. FLIM scaling from 4.70 ns (red) to 5.15 ns (blue).*

FLIM combined with two different environmentally sensitive fluorophores has offered invaluable insight into the LLT in TPP,[191] hence we decided to use it for *n*-butanol. FLIM experiments were carried out with two fluorescence probes – coumarin 153 (C153) and perylene. As mentioned in the previous chapters, perylene is a rigid, nonpolar weakly interacting probe and its excited-state lifetime depends merely on the local refractive index of the medium as described by the Strickler-Berg formula (Equation 8) which predicts that the fluorescence lifetime is inversely proportional to the square of the refractive index ($\tau_0 \propto n^{-2}$). On the other hand, the excited-state lifetime of C153 is strongly influenced by static and dynamic dielectric properties of the medium.[174, 191]

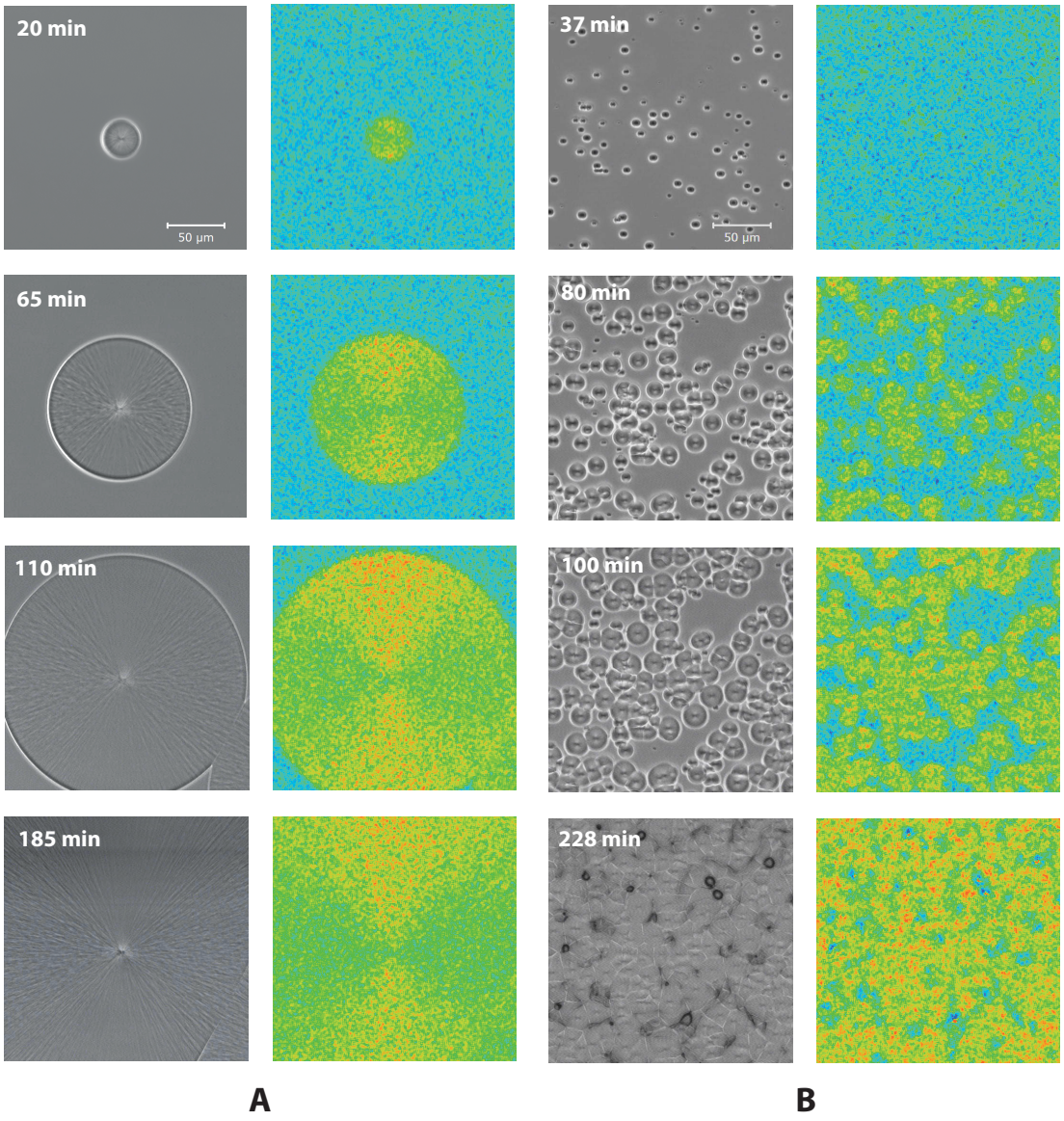

Figure 63. *Representative images of typical patterns observed after quenching of n-butanol to 138 K (**A**) and 130 K (**B**) for the indicated amount of time. The first and third columns show FLIM maps obtained using the probe C153, while the second and forth columns show the respective phase-contrast microscopy images (Zeiss set-up). FLIM scaling: 4.70 ns (red) to 5.15 (blue).*

Representative FLIM maps for two annealing temperatures (T_a) for C153 are shown in Figure 47 and for perylene in Figure 64. Representative normalised fluorescence lifetime distributions for both probes are shown in Figure 55. Contrary to our experiments carried out on TPP, no meaningful difference in behaviour of C153 and perylene was observed. The excited-state lifetime of both dyes decreased by about 3% on transformation from supercooled liquid to the new phase. This showed that there was no significant difference

in dielectric properties between these two phases and the decrease in lifetime was caused by an increase in density by about 4%.

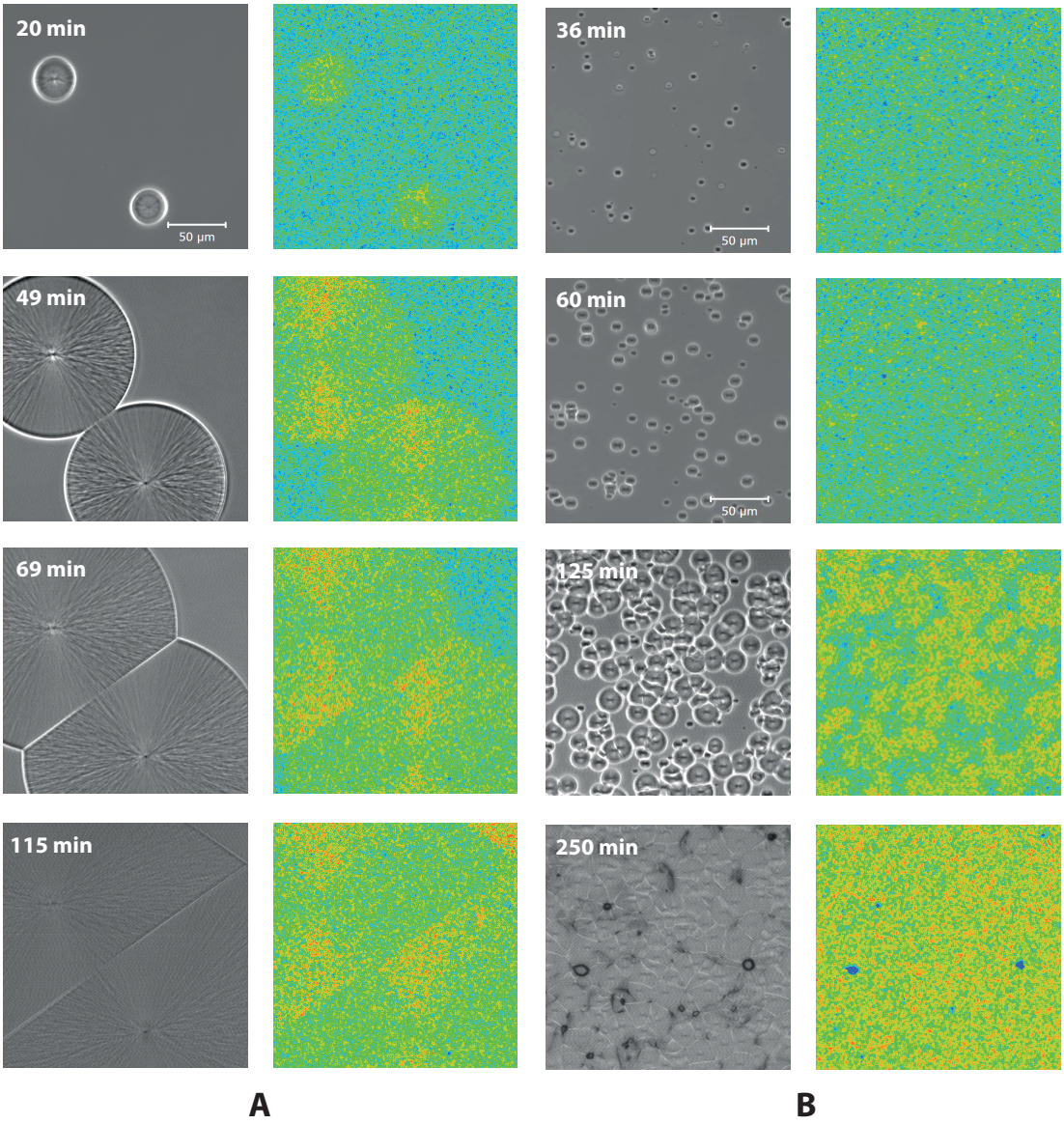

Figure 64. *Representative images of typical patterns observed after quenching of n-butanol to 140 K (**A**) and 130 K (**B**) for the indicated amount of time. The first and third columns show FLIM maps obtained using the probe perylene, while the second and forth columns show the respective phase-contrast microscopy images (Zeiss set-up). FLIM scaling: 4.15 ns (red) to 4.75 (blue).*

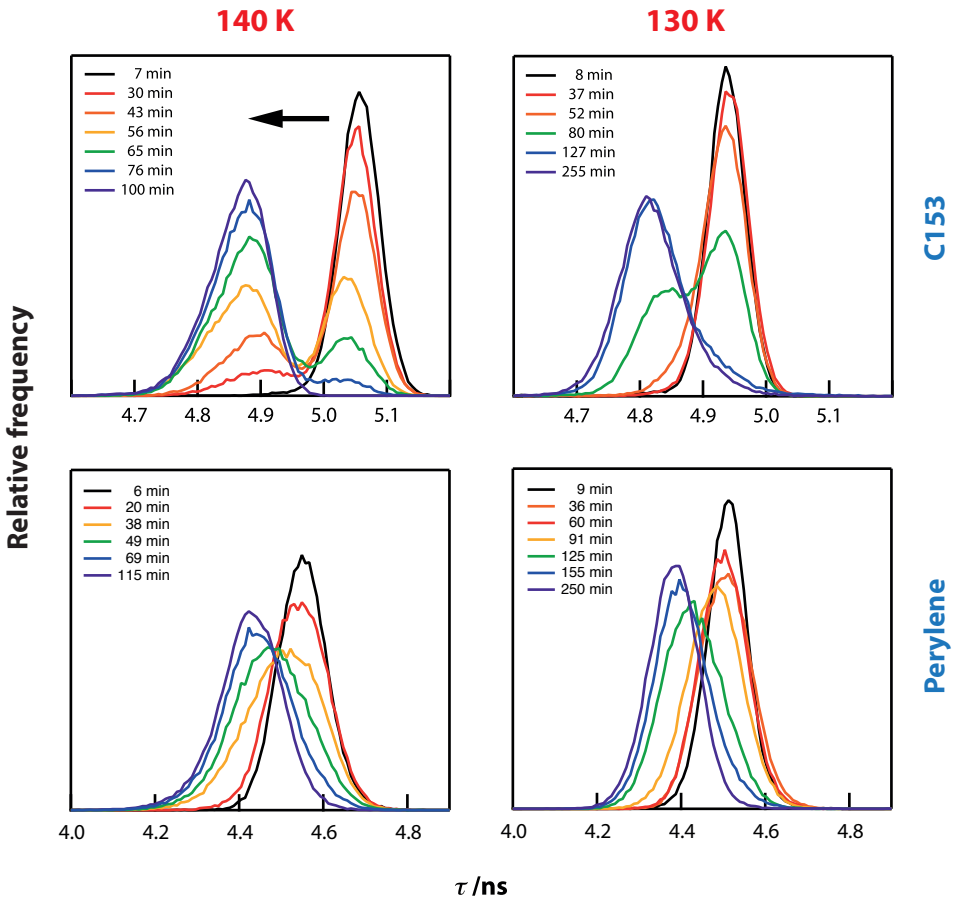

Figure 65. *Normalised fluorescence lifetime distributions of the probe C153 (**top row**) and perylene (**bottom row**) in n-butanol quenched to 140 K and 130 K. Colour coding and the arrow indicate time progression since the selected temperature has been reached.*

Careful examination of the FLIM maps revealed that the fluorescence lifetime exhibited an anisotropic distribution within the nucleating droplets. The same effect (Figure 67) was observed in a droplet of the new phase surrounded by the stable crystalline phase formed after slow increase of temperature to the value below T_m (cold crystallisation). The FLIM maps showed that the excited-state lifetime of C153 is longer in the horizontal direction inside the droplet (4.88 *vs.* 5.05). The stable crystal also displayed some anisotropy but it was much weaker than the one observed in the droplet of the new phase. It appeared that the fluorescence intensity inside the droplet was a function of angle with the highest intensity in the horizontal direction, perpendicular to the laser polarisation.

In case of randomly orientated dye molecules, the anisotropy of the fluorescence, *i.e.* the ratio of the maximum to the minimum fluorescence intensity, should be 1. Dye molecules in the liquid-crystalline phase partially align giving rise to an anisotropy in

the fluorescence. This alignment is modelled with an angular distribution function consisting of a non-aligned part given by $(2\pi)^{-1} P_0(\cos^2 \phi)$ where $P_n(x)$ is the n^{th} order Legendre polynomial and an aligned part $\pi^{-1} P_1(\cos^2 \phi)$ where ϕ is the angle of the molecular transition dipole moment with respect to the laboratory frame. As the excitation probability scales as $\cos^2 \theta$, where θ is the angle between the incoming laser polarisation and the molecular transition dipole moment, we found that the anisotropy in the fluorescence intensity inside the droplet was 2.1 (see Figure 66). This strongly suggested that half of the C153 molecules had random orientation, while the other half had defined alignment. This observation was consistent with a LC phase in which half of the molecules has perpendicular alignment to the local LC director.

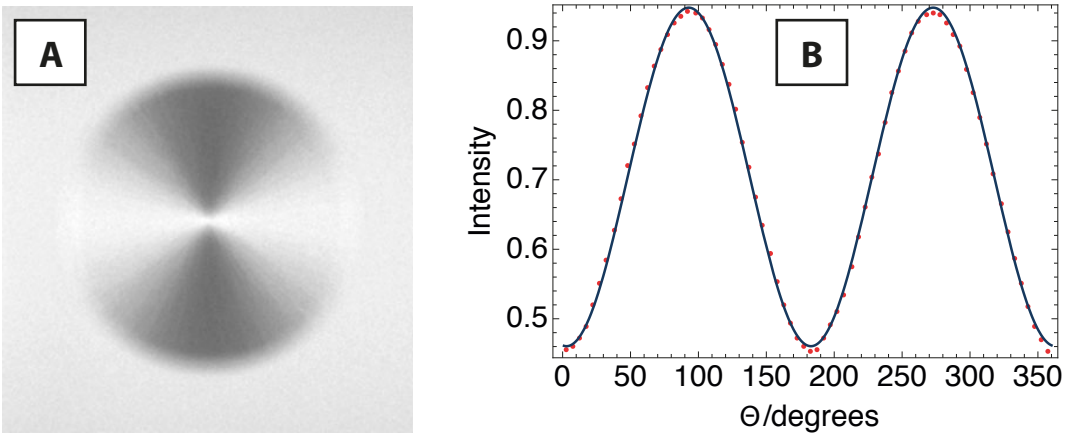

Figure 66. *Determination of the anisotropy of fluorescence. (**A**) Fluorescence intensity of a nucleated droplet in supercooled n-butanol. (**B**) Curve fit to a sin²-function showing that the maximum over minimum is 2.1.*

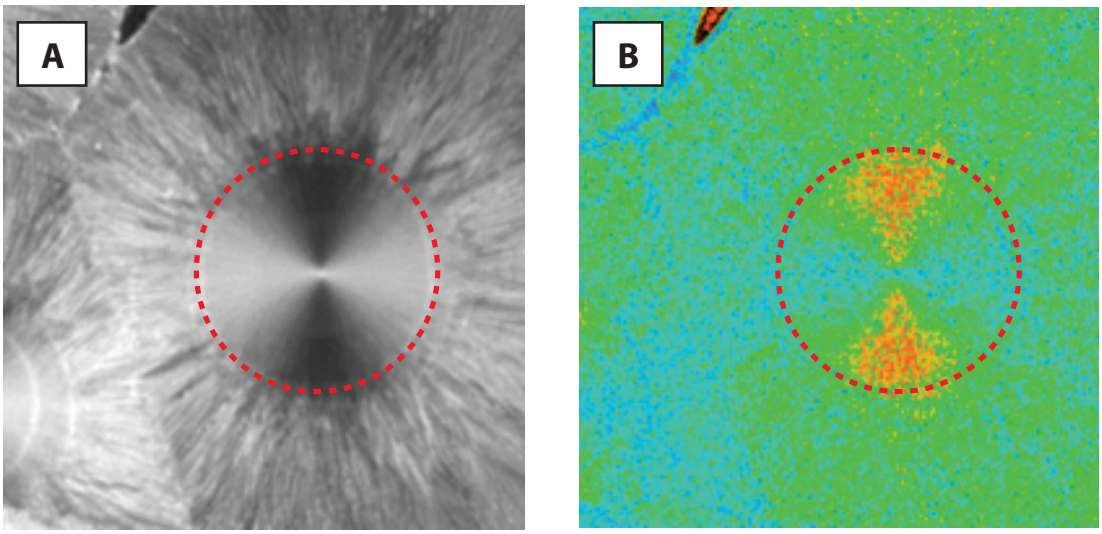

Figure 67. *FLIM data of a nucleated droplet (outline marked with a dashed circle) encased in the stable crystal at 136 K. (**A**) Fluorescence intensity and (**B**) FLIM map obtained using fluorescence fromC153. FLIM scaling from 4.30 ns (red) to 5.30 ns (blue).*

Figure 68 shows polarisation microscopy images obtained during the transformation to the new phase at a representative temperature of 136 K. It can be seen that the nucleating droplets exhibited high-contrast Maltese cross pattern associated with a highly ordered LC phase with a director pointing away from the centre of the droplets. This pattern could be seen at all investigated T_a in the temperature range from 140 to 128 K. These observations provided further evidence that this phenomenon is not a polyamorphic liquid-liquid transition but a transition between an isotropic supercooled liquid to a highly viscous LC phase, which is metastable at given T_a within accessible timescales (hours). When the LC droplets were allowed to grow to a certain size (*e.g.* Figure 68A) and the temperature was raised ($T_a<T<T_m$), the untransformed liquid crystallised with spherulitic growth away from the interface of the LC droplets (Figure 68C). The droplets resisted crystallisation and were not penetrated by the stable crystal. The Maltese cross pattern within the droplets weakened and small grains appeared near to their interface (Figure 68D).

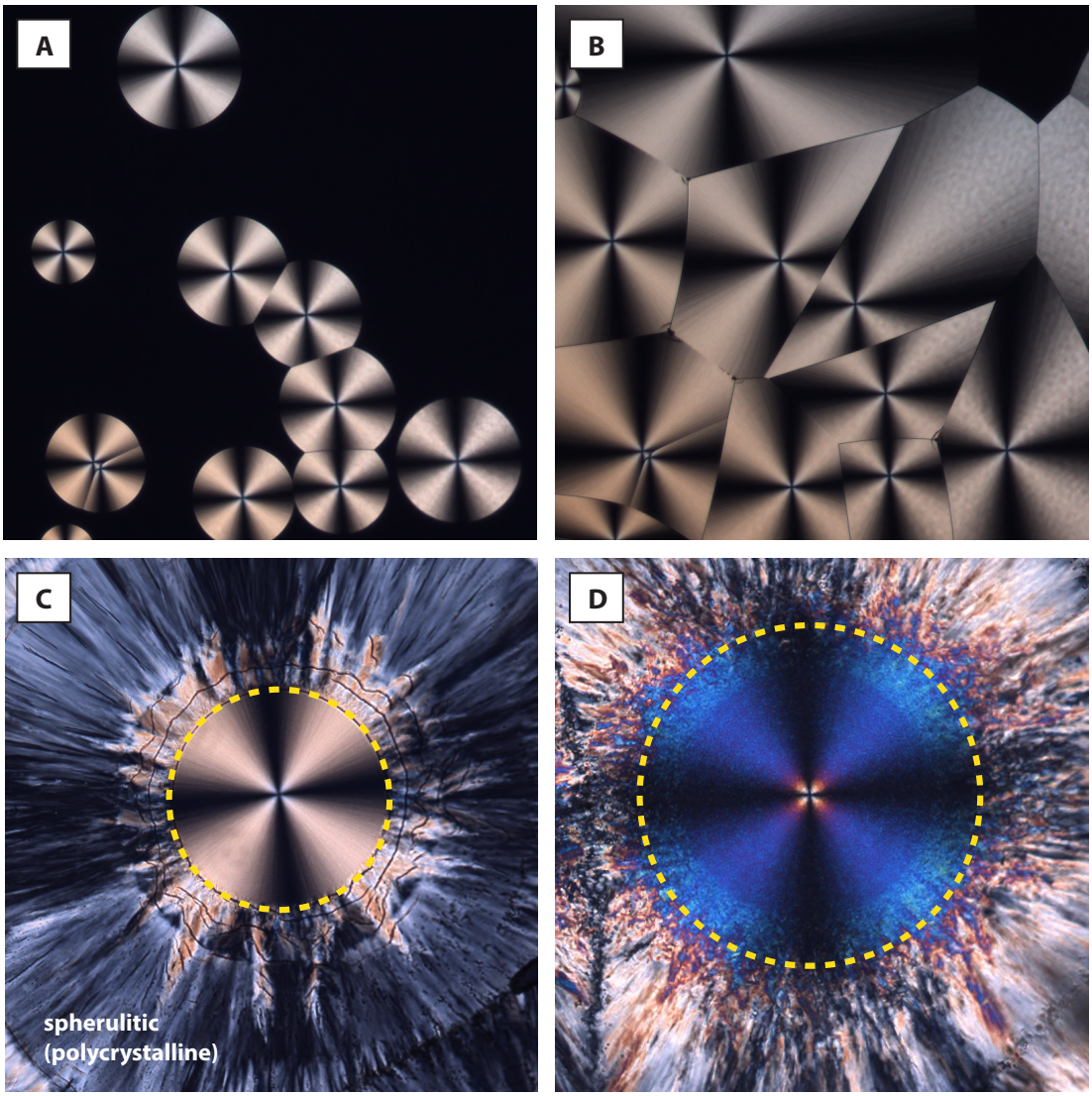

Figure 68. *Polarisation microscopy images of droplets formed in supercooled n-butanol show Maltese cross pattern consistent with liquid crystal (LC) ordering. N-butanol was quenched to 136 K and annealed for 80 min (**A**) and 250 min (**B**). The LC droplets (outlined with a dashed circle) resisted crystallisation despite being surrounded by polycrystalline spherulitic growth as the temperature was increased (**C**, **D**).*

Figure 71 show Raman spectra of all three investigated phases of *n*-butanol, namely the supercooled liquid, the stable crystal and the LC phase. For comparison all spectra were taken at 136 K. When *n*-butanol was cooled from room temperature, the OH-stretch band red shifted and narrowed indicating the formation of strong hydrogen bonds and local structure.[88] When supercooled liquid transformed into the LC phase, the Raman spectrum changed significantly: it resembled the stable crystalline phase but was nevertheless distinct. The OH-stretch bands in the crystal and

the LC phase were much narrower and blue-shifted in comparison to supercooled liquid (Figure 69). However, these bands in the LC phase were broader than the crystal, which implied greater disorder. The Raman spectrum of the low-frequency region (<200 cm^{-1}) of the stable crystal exhibited narrow phonon bands (Figure 71). The same region in the spectrum of the LC phase was broadened and more similar to that of a (structured) supercooled liquid. In the fingerprint region (200-1600 cm^{-1}), the Raman spectra of the LC phase and the stable crystal were very different. Additionally, many subtle changes were detected in the CH-stretch region (Figure 70).

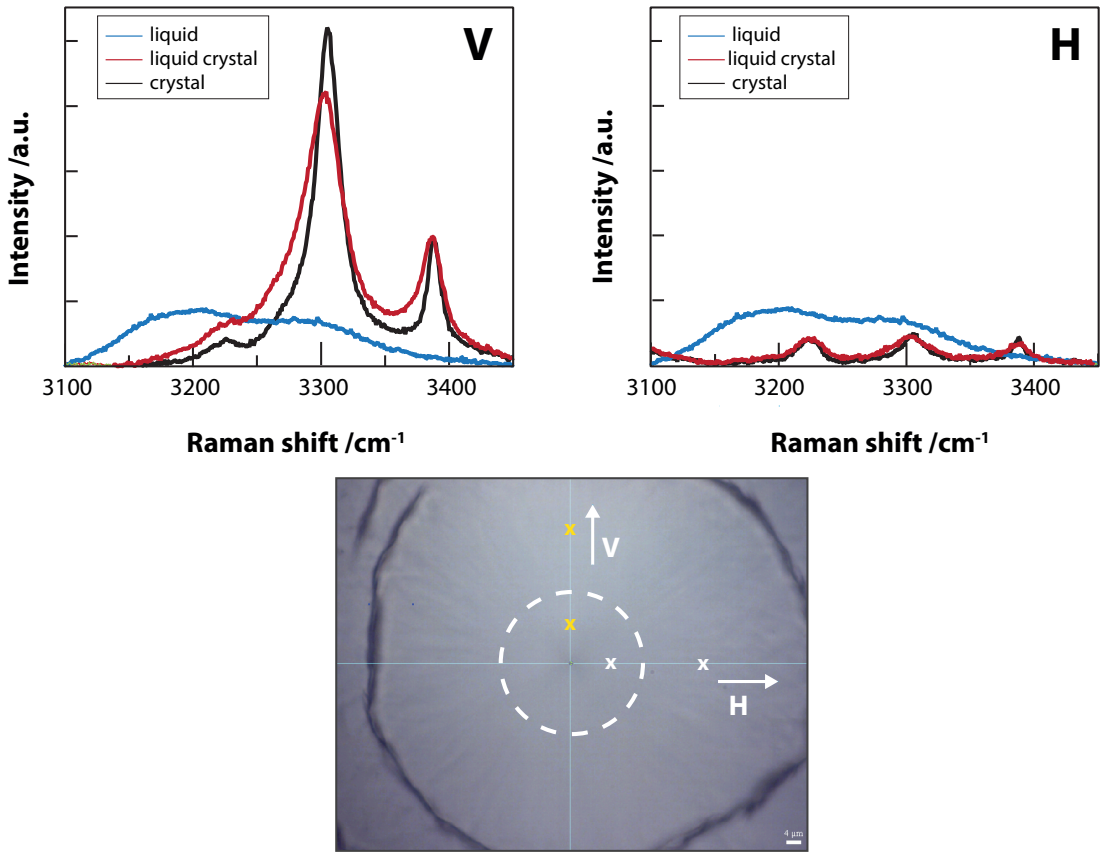

Figure 69. *Raman spectra in the OH-stretch region of three phases of n-butanol at 136 K. "V" corresponds to spectra taken vertically (yellow crosses) above the centre of an encased LC droplet, while "H" was taken horizontally displaced (white crosses) from the centre. Shown are the spectra of supercooled liquid, the stable crystal formed from untransformed supercooled liquid, and the LC phase. The nucleated droplet grew to the size indicated by the dashed circle and the temperature was raised allowing the remaining untransformed liquid to crystallise, followed by quenching to 136 K. Scale bar 4 μm.*

Analysis of the Raman spectra of the LC phase showed that they were distinct and could not be considered as a mixture of the spectra of supercooled liquid and the stable crystalline phases. Similarly to the fluorescence intensity, the Raman intensity showed an anisotropic distribution. It was particularly clear in case of the OH-stretch band, which was an order of magnitude stronger in the vertical direction parallel to the laser polarisation (Figure 69).

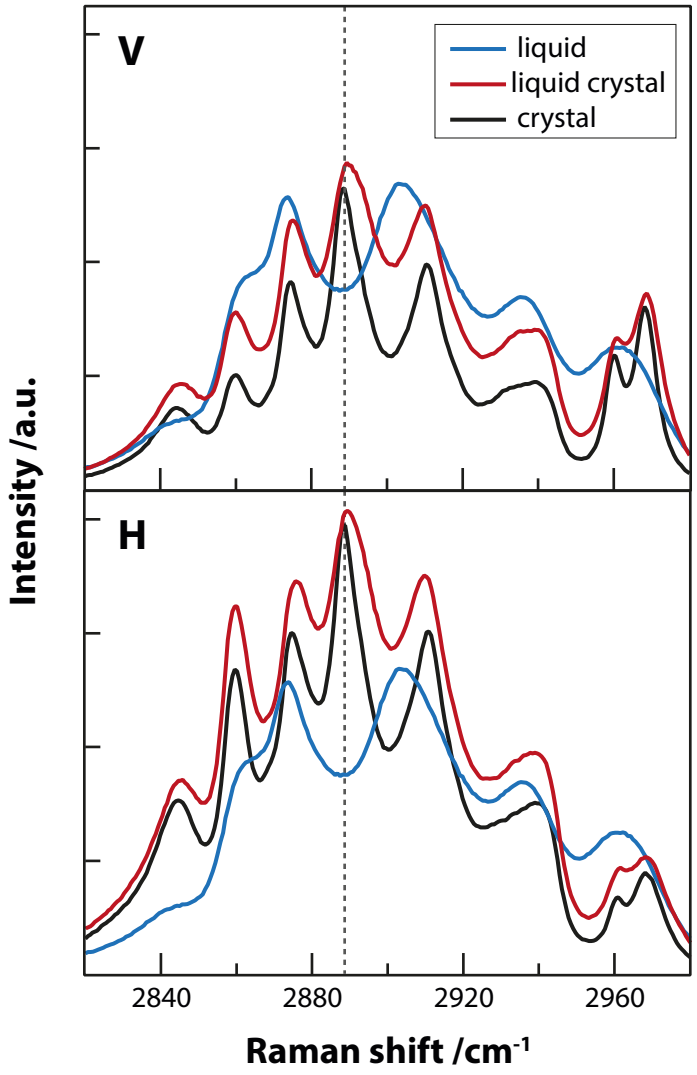

Figure 70. *Raman spectra of the CH-stretch region of three investigated phases of n-butanol recorded at 136 K. Labelling as in Figure 69.*

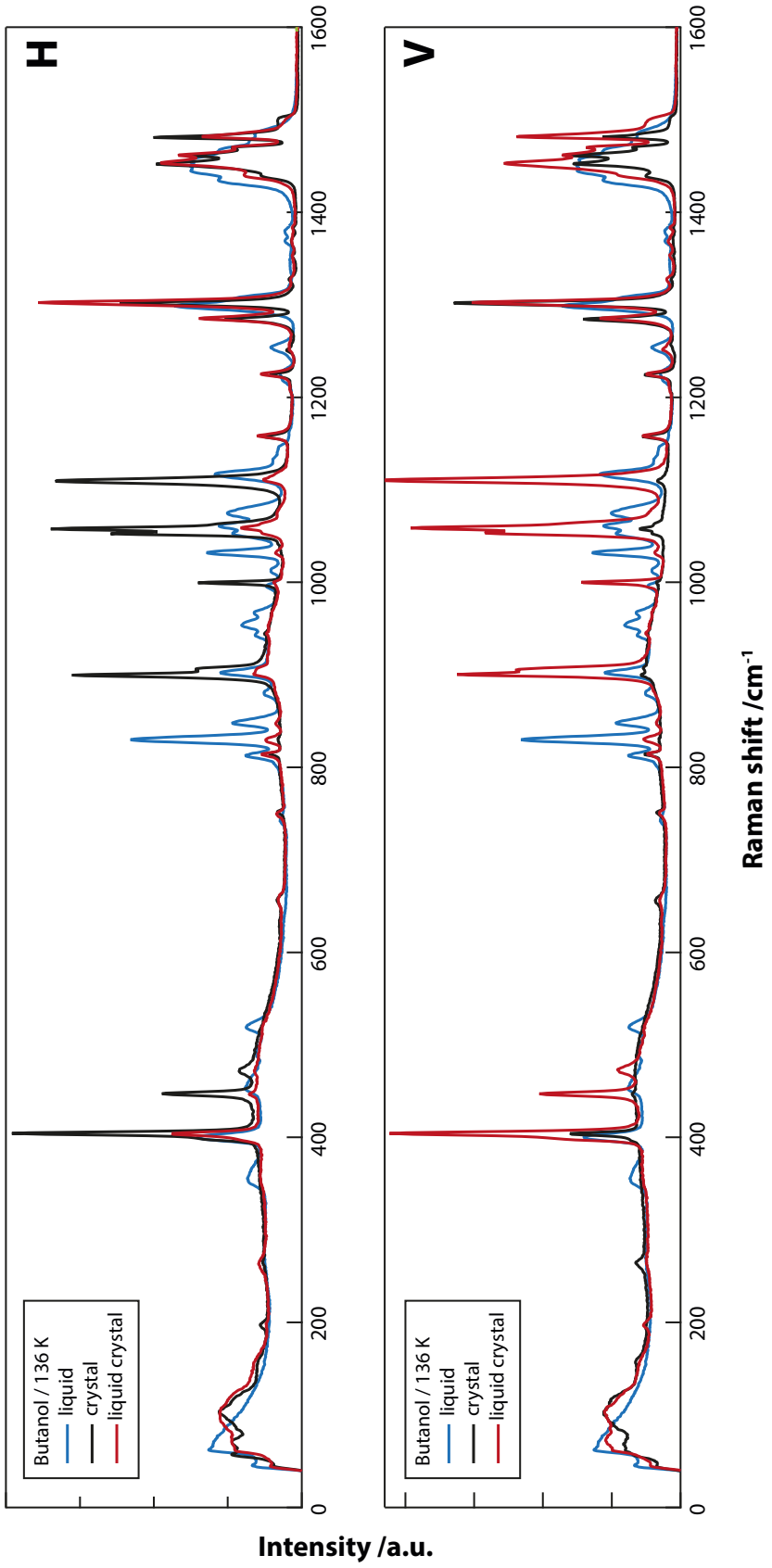

Figure 71. *Raman spectra of the fingerprint region of three investigated phases of n-butanol recorded at 136 K. Labelling as in Figure 69.*

5.3 Additional Data

This section presents additional data collected by other members of our research group within the framework of this project. These are included in this chapter to enable comprehensive discussion of the phenomenon observed in *n*-butanol and the conclusions proposed in our published report.

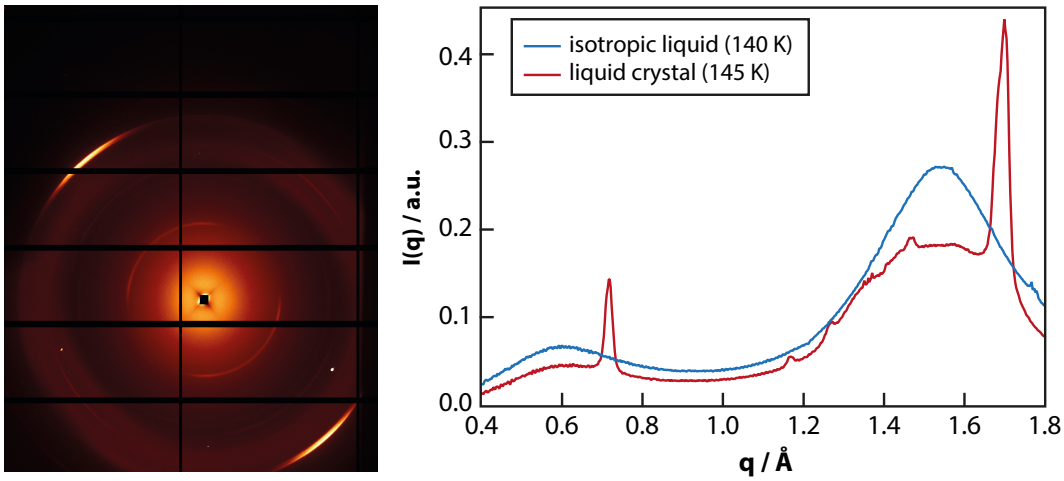

Figure 72. *Microfocus wide-angle x-ray scattering (WAXS) data of n-butanol at 145 K.* ***(left)*** *A WAXS diffraction pattern obtained from an area, approximately 10 μm in diameter, located to the left of the centre of a 400-μm-diameter LC droplet. The intense diffuse bands at the left top and right bottom correspond with a scattering vector* $q = 1.7\ Å^{-1}$. ***(right)*** *WAXS scattering intensity for isotropic liquid at 140 K and LC at 145 K (corresponding to the data in (**left**)).*[192]

Wide-angle x-ray scattering (WAXS) technique was used to probe the supra-molecular structure of the LC phase. The WAXS experiments were carried out using a 10-μm-diameter microfocus beam at the Diamond Light Source on an LC droplet, grown to the size of a few hundred micrometres, isotropic liquid and the crystalline phase. WAXS of isotropic liquid, collected at 140 K, displayed two diffuse bands at q = 0.6 and 1.55 $Å^{-1}$, consistent with previous reports.[87,88] WAXS of a nucleated droplet showed additional less diffused anisotropically scattered bands at q = 0.718 and 1.7 $Å^{-1}$, consistent with the LC phase. The widths of these bands were 0.017 and 0.037 $Å^{-1}$ respectively, corresponding to a coherent domain composed of about 90 molecules. A number of weak peaks, corresponding to (estimated) less than 1.8% contamination with the crystalline phase, were also observed in the WAXS data of the droplet (Figure 72). As the

microfocus beam was scanned around the droplet centre, the orientation of the anisotropic scattering rotated, consistent with the LC director pointed away from the centre.[192]

Further confocal Raman microscopy experiments were carried out on all three phases of *n*-butanol. As these experiments required long acquisition times, the transition dynamics had to be arrested. This was achieved by rapid (20 K/min) quenching to 140 K, followed by droplet growth to approximately 50 μm in diameter and subsequent rapid quenching to 110 K to arrest dynamics or a cold-crystallisation cycle. Such cycle consisted of heating to 173 K followed by a rapid quench to 110 K.[192]

The Raman spectrum presented in Figure 73(left) is practically identical to the one in Figure 69 and as such will not be discussed again. The OH-stretch spectrum around 3100 cm^{-1} was used to estimate the degree of contamination of the LC with isotropic liquid and it was found to be less than 2.8%. This was consistent with full conversion to a new phase.[192]

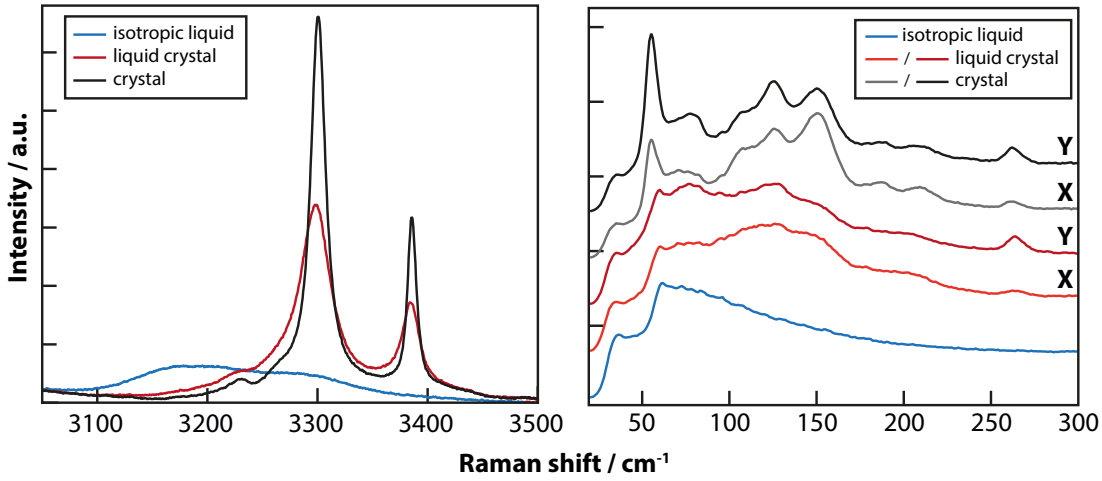

Figure 73. *Raman spectra of three phases of n-butanol. Spectrum of isotropic liquid was taken at 140 K, while the spectra of LC phase (formed at 140 K) and of crystal (formed via subsequent cold crystallisation) were obtained at 110 K. Raman spectra of LC and crystal were taken horizontally (X) or vertically (Y) displaced from the centre. (**left**) Raman spectra in the OH-stretch region taken vertically (Y) displaced from the centre. (**right**) Raman spectra in the low-frequency (phonon) region.*[192]

The changes observed in the low-frequency phonon region were much more subtle than the one which occurred in the OH-stretch region (Figure 73(right)). The spectrum of the isotropic liquid exhibited broad featureless bands in the range ~50–200 cm^{-1}

associated with libration modes at low frequency and hydrogen bond formation at higher frequency.[193] The spectra of the LC phase, recorded at 110 K, and the one recorded for the isotropic liquid at 140 K were very similar with the same hydrogen-bonding and librational modes.[194, 195] Additional structures observed in the LC spectrum in the 60–300 cm^{-1} range strongly suggested a degree of order. However, the order was not at the same level as in the stable crystal as characteristic sharp phonon bands seen in the crystal spectra were not present in the LC. The Raman spectrum of the same region of the droplet after cold crystallisation showed the development of strong phonon bands at 58, 105, and 120 cm^{-1}, associated with the stable crystal. The 58-cm^{-1} phonon band was used to estimate the amount of crystal contamination in the LC droplet prior to cold crystallisation. It was found to be less than 2%.[192]

Figure 74 displays Raman spectral maps of an LC droplet before and after cold crystallisation. It can be seen that the map of the phonon region of the LC droplet, formed at 140 K, showed no significant anisotropy. However, after cold crystallisation of the sample, the phonon region became highly anisotropic, demonstrating that the (nano) crystallites, that apparently formed, were aligned with (what was) the LC director.[192]

Contrary to the observations in the phonon region, the intensity of the OH-stretch Raman band within the LC droplet before cold crystallisation was highly anisotropic. This anisotropy was determined to be ~5,[192] *i.e.* the Raman intensity displaced from the centre of the droplet along y-axis was 5 times stronger than that along the x-axis. Theoretical modelling predicted a maximum Raman anisotropy for the stable crystal of 7.6,[192] consistent with the range of ~5-10 obtained via Raman microscopy experiments carried out on polycrystalline *n*-butanol. This strongly implied that the LC phase was highly ordered. The same sample after cold crystallisation displayed similar anisotropy within (~5) and outside the droplet where the spherulitic crystal growth was observed (also ~5).[192]

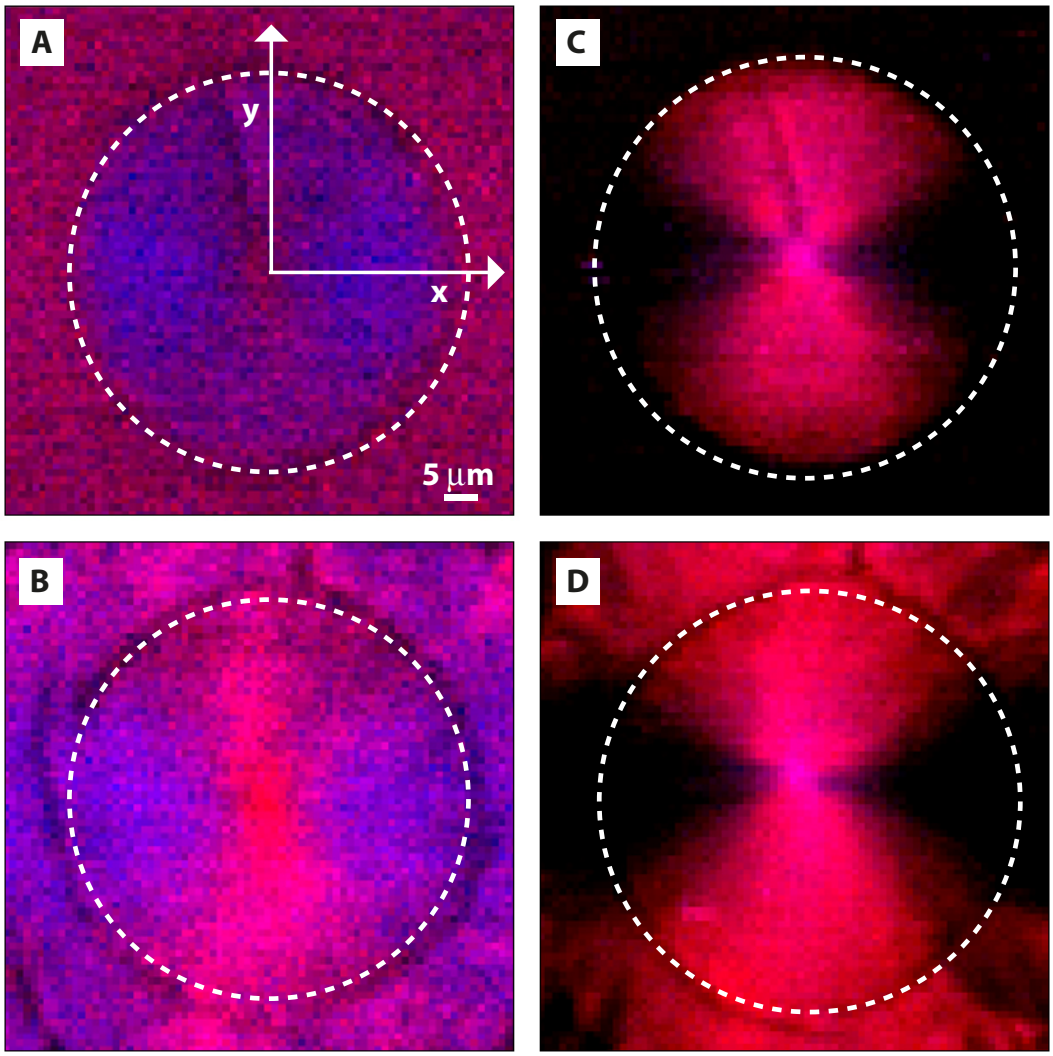

Figure 74. *Raman maps of a droplet nucleated in supercooled n-butanol recorded at 110 K. (**A**, **B**) Raman maps of the low-frequency phonon region (the 55–60 cm^{-1} range shown in red and the 115–130 cm^{-1} range shown in blue). (**C**, **D**) Raman maps of the OH-stretch region (the 3285–3305 cm^{-1} range shown in red and the 3370–3390 cm^{-1} region shown in blue). Maps **A** and **C** correspond to a LC droplet (outlined with a dashed circle) formed after quenching to 140 K, while maps **B** and **D** show the same sample after a cold-crystallisation cycle.*[192]

5.4 Discussion

Polarisation microscopy experiments carried out on the new phase formed in supercooled *n*-butanol strongly implied that it was an spherically symmetric LC. However, polarisation microscopy could not eliminate the possibility that the droplets were

spherulites, *i.e.* patterns consisting of radially oriented microcrystals arranged at noncrystallographic angles,[196] unresolvable by light microscopy.

The FLIM data of C153 and perylene indicated an increase in density by about 4% on transition from supercooled liquid to the LC. However, there was no significant difference in dielectric properties between these two phases. The smooth distribution of the fluorescence intensity in the LC phase showed that the dye was fully incorporated into it. On the other hand, the fluorescence intensity observed in the stable crystal was, as expected, highly variable with position due to the dye expulsion from the crystal lattice.

The observed fluorescence anisotropy inside the LC droplets strongly suggested that the alignment of the dye molecules was perpendicular to the director, as the transition dipole moment was aligned with the long axis of C153. The fluorescence lifetime of C153 was visibly shorter in the vertical direction where the laser preferentially excited dye molecules that were aligned parallel to the LC director. The shorter lifetime is known to be caused by the C153 molecules forming hydrogen bonds with *n*-butanol.[174] The lifetime shortening was not observed in the stable crystal, which supported our conclusion that the droplets were not spherulites or mixtures of crystallites and untransformed supercooled liquid.

The Raman investigations carried out on isotropic liquid showed the OH-stretch region was quite broad reflecting orientational disorder and the formation of up to 3 hydrogen bonds.[197] The physical picture of the isotropic liquid formed on the basis of computer simulations of *n*-octanol, small-angle x-ray scattering studies of *n*-alcohols, and dielectric-relaxation studies, is that it is composed of clusters with a polar hydrogen-bonded core and a nonpolar shell consisting of overlapping alkyl chains (Figure 75). On transforming to the LC phase, orientational disorder was significantly reduced which was reflected in the OH-stretch bands becoming more narrow and blue-shifted, resembling the Raman spectrum of the stable crystal and indicating the presence of only two hydrogen bonds (one donated and one accepted).

As mentioned previously, the OH-stretch Raman-scattering intensity around 3100 cm^{-1} was used to estimate that less than 2.8% of isotropic liquid remained after the transition strongly indicating its completeness within the accuracy of the experiment. The intensity of the main OH-stretch bands was highly anisotropic both in the droplet (before and after cold crystallisation) and in the spherulitic crystal growth outside the droplet. Previous studies found that in the stable crystal of *n*-butanol, the hydrogen-bond network forms infinite chains in the [100] direction.[87] This caused the OH bonds to be aligned

giving rise to a large anisotropy. If the new phase were an LC, the observed anisotropy would be consistent with the parallel alignment of the OH bond with the LC director. On the other hand, if the newly formed phase were a spherulite, then these observations would imply a complete conversion to a spherulitic polycrystalline phase.

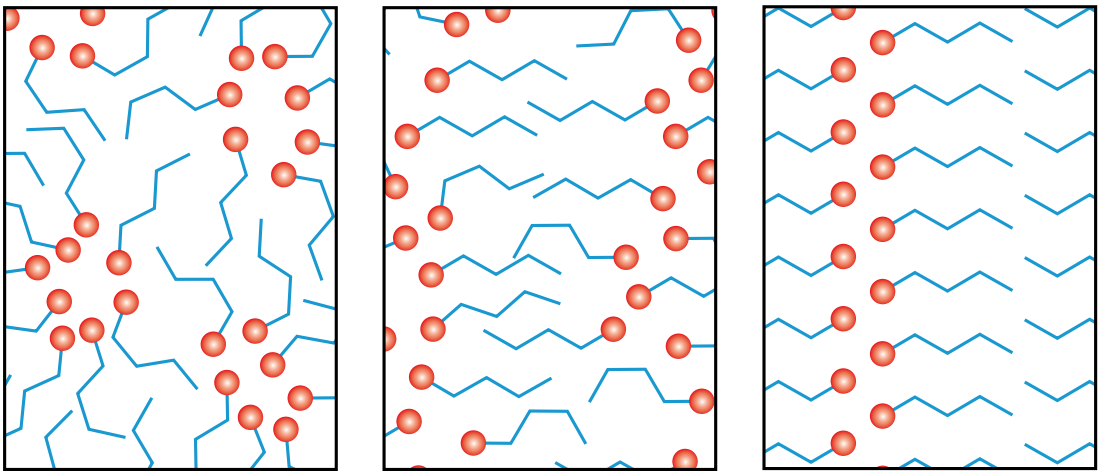

Figure 75. *Schematic illustration of the molecular structure of three investigated phases of n-butanol: the isotropic liquid (**A**), the rippled lamellar LC (**B**) and the stable crystal (**C**). Red spheres represent the OH groups.*

When a crystalline phase is formed, sharp phonon peaks are expected to be detected in the low-frequency Raman spectrum. That was the case with the spherulitic crystal growth formed around the droplets after cold crystallisation, which displayed strong phonon bands at 58 and 72 cm^{-1}. However, the same peaks measured inside the droplet before cold crystallisation, were very weak with estimated less than 2% contamination with crystals. This result was consistent with the WAXS data leading to an estimated 1.8% contamination with crystals.[192] After a cold crystallisation cycle, the phonon peaks inside the droplet were identical to those in the stable crystal. These observations were inconsistent with a full conversion to a spherulitic crystal and also inconsistent with an "arrested crystallisation" scenario. They were, however, consistent with a complete transition to an LC contaminated with less than 2% (nano) crystallites and very weak anisotropy in the phonon region in the nucleated droplet before cold crystallisation.

The WAXS data also demonstrated the formation of an LC phase. The diffraction peak at $q = 0.718$ $Å^{-1}$ correlates with the (001) x-ray scattering peak in the stable crystal and a Bragg separation of $d = 8.75$ Å, where d relates to q as $q = \frac{2\pi}{d}$. This distance corresponds

to the distance between hydrogen-bonded molecular planes in the stable crystal (see Figure 76A).[87] Also the diffraction peak at $q = 1.7$ Å^{-1} correlates with (012) x-ray scattering peak in the crystal and a Bragg separation of 3.7 Å. The (012) reflection is associated with nearest neighbour packing perpendicular to the long axis of *n*-butanol. Therefore these observations were inconsistent with the formation of a nematic LC phase or a spherulitic crystalline phase. They were, however, consistent with a rippled lamellar LC or gel phase. This conclusion was additionally supported by Raman spectra of the CH-stretch region showing that the alkyl chains in the LC were arranged in mixed gauche and trans conformations.[198]

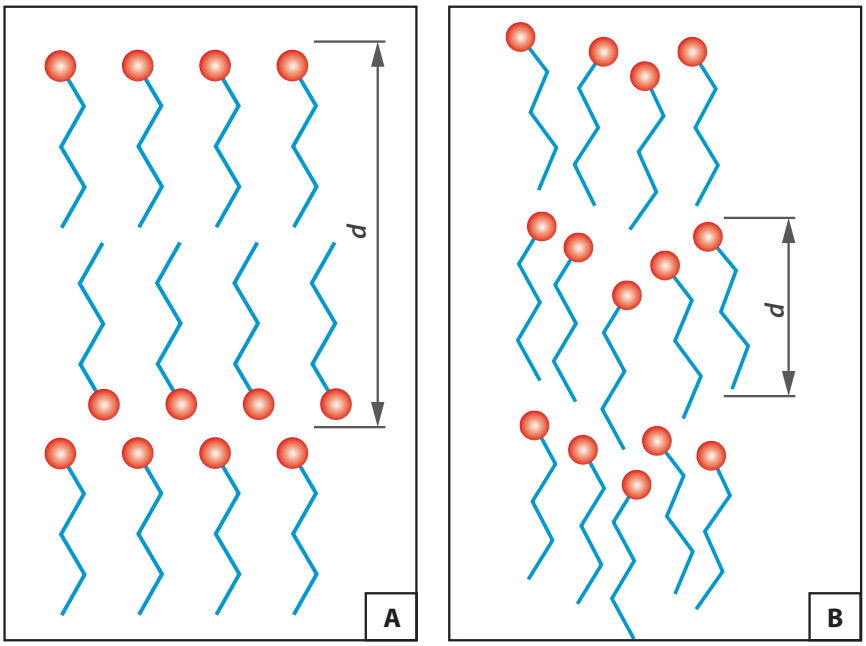

Figure 76. *Schematic illustration demonstrating that the new phase is not a nematic LC. (**A**) Known crystal structure; d (determined as 8.75 Å) indicates the distance between hydrogen-bonded molecular planes. (**B**) Nematic LC; it can bee seen that if molecules of the new phase where arranged in this way, d would be about half of the expected d value.*

We observed that on heating of the samples towards T_m, the untransformed supercooled liquid crystallised without affecting the LC droplets (Figure 68C). This further supported the conclusion that the LC phase was metastable and frustrated the formation of the stable crystal. These observations were not consistent with the LC being a metastable intermediate state on the pathway between the isotropic liquid and the stable crystal, postulated by Ostwald's rule of stages.

Brillouin scattering studies on *n*-butanol found crystalline-like acoustic phonon peaks in the new phase inconsistent with those observed in the crystal.[90, 91] These observations can be now reinterpreted as resulting from the partial ordering of the LC. Also, the recently reported disappearance of the Debye process combined with the survival of the liquid-like β-process during the transition[199] is consistent with the formation of the LC and the associated breakup of the hydrogen-bonded clusters in the isotropic liquid.

5.5 Conclusions

Our spectroscopic and imaging investigations of the phenomenon occurring in supercooled *n*-butanol, led us to conclude that it is not a polyamorphic LLT[29] between two isotropic phases but an isotropic liquid to LC transition. The LC phase in *n*-butanol is not "in between" the isotropic liquid and the crystal but it frustrates the formation of the (thermodynamically more stable) crystalline state.

We excluded the possibility of the formation of a mixed state composed of nanocrystallites and untransformed supercooled liquid or an "arrested crystallisation".[87-91] Our conclusion is supported by previously reported calorimetric measurements.[29, 90, 91, 200] They observed that on heating of the *n*-butanol glass at different speeds, two exothermic peaks were observed – one associated with the "glacial phase" and the one linked to the formation of the stable crystalline phase at 155 K.[91] The origin of the former peak can be now seen as the formation of a rippled lamellar LC phase.

The estimated temperature range for the observed transition is between 150 K and 120 K, located just above the T_g of *n*-butanol.[90] It is unusual for a liquid to LC transition to have such a large degree of supercooling (30 K) and it may lead to high viscosity of the LC phase and the sharp interfaces shown in Figure 68B. The Raman investigations show that the observed transition resembles crystallisation in terms of the number of hydrogen bonds being severed due to the breakup of liquid clusters and the large interfacial energy. This explains the unusually large supercooling and the formation of the LC as droplets rather than schlieren textures.

Previously reported structural investigations established that in the stable crystalline phase of *n*-butanol the molecules are stacked anti-parallel forming infinite chains of hydrogen bonds.[87] We find that in the LC phase the hydrogen-bonded chains are disordered (rippled) and their alkyl tails have a distribution of gauche and trans conformations (Figure 75).

Lastly, the reports of the formation of the mixed state composed of microcrystallites and untransformed liquid will be addressed.[87-89, 91, 200] We showed this conclusion to be incorrect and we explain the presence of microcrystallites at higher temperatures by the *n*-butanol molecules having sufficient kinetic energy to escape from the frustrated state and move towards thermodynamic equilibrium.

6

References

1. Angell, C., Formation of glasses from liquids and biopolymers. In *Science*, 1995; Vol. 267, pp 1924-1935.
2. Poole, P.; Grande, T.; Angell, C.; McMillan, P., Polymorphic phase transitions in liquids and glasses. In *Science*, 1997; Vol. 275, pp 322-323.
3. Tanaka, H., General view of a liquid-liquid phase transition. In *Phys Rev E*, 2000; Vol. 62, pp 6968-6976.
4. Tanaka, H., General view of a liquid-liquid phase transition. *Phys. Rev. E* 2000, *62* (5), 6968.
5. Mishima, O.; Calvert, L.; Whalley, E., 'Melting ice'I at 77 K and 10 kbar: a new method of making amorphous solids. In *Nature*, 1984; Vol. 310, pp 393-395.
6. Mishima, O.; Calvert, L.; Whalley, E., An apparently first-order transition between two amorphous phases of ice induced by pressure. In *Nature*, 1985; Vol. 314, pp 76-78.
7. Aasland, S.; McMillan, P., Density-driven liquid-liquid phase-separation in the system Al2O3-Y2O3. In *Nature*, 1994; Vol. 369, pp 633-636.
8. Skinner, L. B.; Barnes, A.; Salmon, P. S.; Crichton, W. A., Phase separation, crystallization and polyamorphism in the Y2O3-Al2O3 system. *J. Phys. Condens. Matter* 2008, *20*, 205103.
9. Deb, S. K.; Wilding, M.; Somayazulu, M.; McMillan, P. F., Pressure-induced amorphization and an amorphous-amorphous transition in densifed porous silicon. *Nature* 2001, *414*, 528-530.
10. McMillan, P. F., Polyamorphic transformations in liquids and glasses. *Journal of Materials Chemistry* 2004, *14* (10), 1506.
11. Wilding, M. C.; Wilson, M.; McMillan, P. F., Structural studies and polymorphism in amorphous solids and liquids at high pressure. *Chem Soc Rev* 2006, *35* (10), 964-86.
12. Sastry, S.; Austen Angell, C., Liquid-liquid phase transition in supercooled silicon. *Nat Mater* 2003, *2* (11), 739-43.

13. Meade, C.; Hemley, R. J.; Mao, H. K., High-pressure x-ray diffraction of SiO2 glass. *Phys Rev Lett* 1992, *69* (9), 1387-1390.
14. Zha, C.-s.; Hemley, R. J.; Mao, H.-k.; Duffy, T. S.; Meade, C., Acoustic velocities and refractive index of SiO2 glass to 57.5 GPa by Brillouin scattering. *Physical Review B* 1994, *50* (18), 13105-13112.
15. Katayama, Y.; Inamura, Y.; Mizutani, T.; Yamakata, M.; Utsumi, W.; Shimomura, O., Macroscopic separation of dense fluid phase and liquid phase of phosphorus. In *Science*, 2004; Vol. 306, pp 848-851.
16. Katayama, Y.; Mizutani, T.; Utsumi, W.; Shimomura, O.; Yamakata, M.; Funakoshi, K.-i., A first-order liquid-liquid phase transition in phosphorus. *Nature* 2000, *403*, 170-173.
17. Monaco, G.; Falconi, S.; Crichton, W. A.; Mezouar, M., Nature of the first-order phase transition in fluid phosphorus at high temperature and pressure. *Phys. Rev. Lett.* 2003, *90* (25), 255701.
18. Morishita, T., Liquid-liquid phase transitions of phosphorus via constant-pressure first-principles molecular dynamics simulations. *Phys Rev Lett* 2001, *87* (10), 105701.
19. Wolf, G. H.; Wang, S.; Herbst, C. A.; Durben, D. J.; Oliver, W. F.; Kang, Z. C.; Halvorson, K., Pressure induced collapse of the tetrahedral framework in crystalline and amorphous GeO2. *High Pressure Research: Application to Earth and Planetary Science* 1992, 503-517.
20. Itie, J. P.; Polian, A.; Calas, G.; Petiau, J.; Fontaine, A.; Tolentino, H., Pressure-induced coordination changes in crystalline and vitreous GeO2. *Phys Rev Lett* 1989, *63* (4), 398-401.
21. Bundy, F., Melting of graphite at very high pressure. In *J Chem Phys*, 1963; Vol. 38, pp 618-630.
22. Grumbach, M., Phase diagram of carbon at high pressures and temperatures. In *Phys Rev B*, 1996; Vol. 410, pp 145-155.
23. Togaya, M., Pressure dependences of the melting temperature of graphite and the electrical resistivity of liquid carbon. In *Phys. Rev. Lett.*, 1997; Vol. 79, pp 2474-2477.
24. Ghiringhelli, L. M.; Los, J. H.; Meijer, E. J.; Fasolino, A.; Frenkel, D., Modeling the phase diagram of carbon. *Phys Rev Lett* 2005, *94* (14), 145701.
25. Wang, X.; Scandolo, S.; Car, R., Carbon phase diagram from ab initio molecular dynamics. *Phys Rev Lett* 2005, *95* (18), 185701.
26. Skibinsky, A.; Buldyrev, S. V.; Franzese, G.; Malescio, G.; Stanley, H. E., Liquid-liquid phase transitions for soft-core attractive potentials. *Physical Review E* 2004, *69* (6).
27. Verso, F. L.; Tau, M.; Reatto, L., Star polymers: study of fluid-fluid transitions in a system with a repulsive ultrasoft-core. *J. Phys. Condens. Matter* 2003, *15*, 1505-1520.
28. Ha, A.; Cohen, I.; Zhao, X.; Lee, M.; Kivelson, D., Supercooled liquids and polyamorphism. In *J Phys Chem-Us*, 1996; Vol. 100, pp 1-4.
29. Kurita, R.; Tanaka, H., On the abundance and general nature of the liquid-liquid phase transition in molecular systems. In *J Phys-Condens Mat*, 2005; Vol. 17, pp L293-L302.
30. Poole, P.; Grande, T.; Angell, C.; McMillan, P., Polymorphic phase transitions in liquids and glasses. *Science* 1997, *275* (5298), 322-323.
31. Mishima, O.; Stanley, H. E., The relationship between liquid, supercooled and glassy water. *Nature* 1998, *396* (6709), 329-335.
32. Angell, C. A., Insights into phases of liquid water from study of its unusual glass-forming properties. In *Science*, 2008; Vol. 319, pp 582-587.
33. Mishima, O.; Stanley, H., The relationship between liquid, supercooled and glassy water. In *Nature*, 1998; Vol. 396, pp 329-335.
34. Debendetti, P. G., Supercooled and glassy water. *J. Phys. Condens. Matter* 2003, *15*, R1669-R1726.
35. Mishima, O., Polyamorphism in water. In *P Jpn Acad B-Phys*, 2010; Vol. 86, pp 165-175.

36. Tanaka, H., Thermodynamic anomaly and polyamorphism of water. In *Europhys Lett*, 2000; Vol. 50, pp 340-346.
37. Black, J., The Supposed Effect of Boiling upon Water, in Disposing It to Freeze More Readily, Ascertained by Experiments. By Joseph Black, M. D. Professor of Chemistry at Edinburgh, in a Letter to Sir John Pringle, Bart. P. R. S. *Philosophical Transactions of the Royal Society of London* 1775, *65* (0), 124-128.
38. Lamanna, R., Delmelle, M., Cannistraro , S., Role of hydrogen-bond cooperativity and free-volume fluctuations in the non-Arrhenius behavior of water self-diffusion: A continuity-of-states model. *Phys. Rev. E* 1994, *49*, 2841.
39. Cho, C. H., S. Singh, S., Robinson, G.W., *Phys. Rev. Lett.* 1996, *76*, 1651.
40. Dougherty, R. C., Howard, L.N., *J. Chem. Phys.* 1998, *109*, 7379.
41. Speedy, R.; Angell, C., Isothermal compressibility of supercooled water and evidence for a thermodynamic singularity at– 45 C. *J. Chem. Phys.* 1976, *65*, 851.
42. Mishima, O., Calvert, L.D., Whalley, E., *Nature* 1984, *310*, 393.
43. Mishima, O., Calvert, L.D. Whalley, E., *Nature* 1985, *314*, 76.
44. Kanno, H.; Tomikawa, K.; Mishima, O., Raman spectra of low-and high-density amorphous ices. In *Chem Phys Lett*, 1998; Vol. 293, pp 412-416.
45. Kolesnikov, A. I.; Li, J. C.; Ahmad, N. C.; Loong, C.-K.; Nipko, J.; Yocum, D.; Parker, S. F., Neutron spectroscopy of high-density amorphous ice. *Phys. B* 1999, *263-264*, 650-652.
46. Kolesnikov, A. I.; Sinitsyn, V. V.; Ponyatovsky, E. G.; Natkaniec, I.; Smirnov, L. S.; Li, J.-C., Neutron-scattering studies of ice prepared by different thermobaric treatments. *J. Phys. Chem B* 1997, *101*, 6082-6086.
47. Poole, P.; Sciortino, F.; Grande, T.; Stanley, H.; Angell, C., Effect of hydrogen-bonds on the thermodynamic behavior of liquid water. *Phys. Rev. Lett.* 1994, *73* (12), 1632-1635.
48. Stanley, H. E., Cruz, L., Harrington, S.T., Poole, P.H., Sastry, S., Sciortino, F., Starr, F.W., Zhang, R., *Physica A* 1997, *236*, 19-37.
49. Harrington, S.; Zhang, R.; Poole, P.; Sciortino, F.; Stanley, H., Liquid-liquid phase transition: Evidence from simulations. *Phys. Rev. Lett.* 1997, *78* (12), 2409-2412.
50. Tanaka, H., Simple physical explanation of the unusual thermodynamic behavior of liquid water. *Phys. Rev. Lett.* 1998, *80* (26), 5750-5753.
51. Tanaka, H., Simple physical model of liquid water. *J. Chem. Phys.* 2000, *112*, 799.
52. Liu, L.; Chen, S. H.; Faraone, A.; Yen, C. W.; Mou, C. Y., Pressure dependence of fragile-to-strong transition and a possible second critical point in
supercooled confined water. *Phys. Rev. Lett.* 2005, *95*, 117802.
53. Mallamace, F.; Branca, C.; Broccio, M.; Corsaro, C.; Gonzalez-Segredo, N.; Spooren, J.; Stanley, H. E.; Chen, S.-H., Transport properties of supercooled confined water. *Eur. Phys. J. Special Topics* 2008, *161* (1), 19-33.
54. Doster, W.; Busch, S.; Gaspar, A. M.; Appavou, M.-S.; Wuttke, J.; Scheer, H., Dynamical transition of protein-hydration water. *Phys. Rev. Lett.* 2010, *104*, 098101.
55. Mancinelli, R., The effect of confinement on water structure. *J. Phys. Condens. Matter* 2010, *22*, 404213.
56. Morineau, D.; Alba-Simionesco, C., Does molecular self-association survive in nanochannels? *J. Phys. Chem. Lett.* 2010, *1*, 1155-1159.
57. Findenegg, G. H.; Jähnert, S.; Akcakayiran, D.; Schreiber, A., Freezing and melting of water confined in silica nanopores. *ChemPhysChem* 2008, *9*, 2651-2659.
58. Demirjian, B.; Dosseh, G.; Chauty, A.; Ferrer, M.; Morineau, D.; Lawrence, C.; Takeda, K.; Kivelson, D.; Brown, S., Metastable solid phase at the crystalline-amorphous border: The glacial phase of triphenyl phosphite. In *J Phys Chem B*, 2001; Vol. 105, pp 2107-2116.
59. Cohen, I.; Ha, A.; Zhao, X.; Lee, M.; Fischer, T.; Strouse, M.; Kivelson, D., A low-temperature amorphous phase in a fragile glass-forming substance. *J Phys Chem-Us* 1996, *100* (20), 8518-8526.

60. Johari, G.; Ferrari, C., Calorimetric and dielectric investigations of the phase transformations and glass transition of triphenyl phosphite. In *J Phys Chem B*, 1997; Vol. 101, pp 10191-10197.
61. Wiedersich, J.; Kudlik, A.; Gottwald, J.; Benini, G.; Roggatz, I.; Rössler, E., On polyamorphism of triphenyl phosphite. In *The Journal of Physical Chemistry B*, 1997; Vol. 101, pp 5800-5803.
62. Dvinskikh, S.; Benini, G.; Senker, J.; Vogel, M.; Wiedersich, J.; Kudlik, A.; Rossler, E., Molecular motion in the two amorphous phases of triphenyl phosphite. In *J Phys Chem B*, 1999; Vol. 103, pp 1727-1737.
63. Mizukami, M.; Kobashi, K.; Hanaya, M.; Oguni, M., Presence of two freezing-in processes concerning alpha-glass transition in the new liquid phase of triphenyl phosphite and its consistency with "cluster structure" and "intracluster rearrangement for alpha process" models. In *J Phys Chem B*, 1999; Vol. 103, pp 4078-4088.
64. Terashima, Y.; Tsuchie, M.; Takeda, K.; Honda, M., Observation of equilibrium liquid–liquid transition in triphenyl phosphite. In *Chem Phys Lett*, 2013.
65. Hedoux, A.; Guinet, Y.; Descamps, M., Raman signature of polyamorphism in triphenyl phosphite. In *Phys Rev B*, 1998; Vol. 58, p 31.
66. Hedoux, A.; Hernandez, O.; Lefebvre, J.; Guinet, Y.; Descamps, M., Mesoscopic description of the glacial state in triphenyl phosphite from an x-ray diffraction experiment. In *Phys Rev B*, 1999; Vol. 60, p 9390.
67. Hédoux, A.; Guinet, Y.; Descamps, M.; Bénabou, A., Raman scattering investigation of the glaciation process in triphenyl phosphite. In *The Journal of Physical Chemistry B*, 2000; Vol. 104, pp 11774-11780.
68. Hédoux, A.; Derollez, P.; Guinet, Y.; Dianoux, A.; Descamps, M., Low-frequency vibrational excitations in the amorphous and crystalline states of triphenyl phosphite: A neutron and Raman scattering investigation. In *Phys Rev B*, 2001; Vol. 63, p 144202.
69. Hédoux, A.; Guinet, Y.; Descamps, M., Size dependence of the Raman spectra in an amorphous–nanocrystalline mixed phase: the glacial state of triphenyl phosphite. In *J Raman Spectrosc*, 2001; Vol. 32, pp 677-688.
70. Hedoux, A.; Denicourt, T.; Guinet, Y.; Carpentier, L.; Descamps, M., Conversion of the glacial state into the crystal in triphenyl phosphite. In *Solid State Commun*, 2002; Vol. 122, pp 373-378.
71. Hedoux, A.; Dore, J.; Guinet, Y.; Bellissent-Funel, M.; Prevost, D.; Descamps, M.; Grandjean, D., Analysis of the local order in the glacial state of triphenyl phosphite by neutron diffraction. In *Phys Chem Chem Phys*, 2002; Vol. 4, pp 5644-5648.
72. Hedoux, A.; Guinet, Y.; Descamps, M.; Hernandez, O.; Derollez, P.; Dianoux, A.; Foulon, M.; Lefebvre, J., A description of the frustration responsible for a polyamorphism situation in triphenyl phosphite. In *J Non-Cryst Solids*, 2002; Vol. 307, pp 637-643.
73. Hedoux, A.; Guinet, Y.; Foulon, M.; Descamps, M., Evidence for transient kinetics of nucleation as responsible for the isothermal transformation of supercooled liquid into the glacial state of triphenyl phosphite. In *J Chem Phys*, 2002; Vol. 116, pp 9374-9382.
74. Hernandez, O.; Hedoux, A.; Lefebvre, J.; Guinet, Y.; Descamps, M.; Papoular, R.; Masson, O., Ab initio structure determination of triphenyl phosphite by powder synchrotron X-ray diffraction. In *Journal of Applied Crystallography*, 2002; Vol. 35, pp 212-219.
75. Guinet, Y.; Denicourt, T.; Hedoux, A.; Descamps, M., The contribution of the Raman spectroscopy to the understanding of the polyamorphism situation in triphenyl phosphite. In *J Mol Struct*, 2003; Vol. 651, pp 507-517.

76. Derollez, P.; Hernandez, O.; Hedoux, A.; Guinet, Y.; Masson, O.; Lefebvre, J.; Descamps, A., Structural and microstructural description of the glacial state in triphenyl phosphite from powder synchrotron X-ray diffraction data and Raman scattering investigations. In *J Mol Struct*, 2004; Vol. 694, pp 131-138.
77. Hedoux, A.; Guinet, Y.; Derollez, P.; Hernandez, O.; Paccou, L.; Descamps, M., Microstructural investigations in the glacial state of triphenyl phosphite. In *J Non-Cryst Solids*, 2006; Vol. 352, pp 4994-5000.
78. Hernandez, O.; Boucekkine, A.; Hédoux, A., Density functional theory study of triphenyl phosphite: molecular flexibility and weak intermolecular hydrogen bonding. In *The Journal of Physical Chemistry A*, 2007; Vol. 111, pp 6952-6958.
79. Kurita, R.; Tanaka, H., Critical-like phenomena associated with liquid-liquid transition in a molecular liquid. In *Science*, 2004; Vol. 306, pp 845-848.
80. Tanaka, H.; Kurita, R.; Mataki, H., Liquid-liquid transition in the molecular liquid triphenyl phosphite. In *Phys. Rev. Lett.*, 2004; Vol. 92, pp 025701-1521.
81. Cohen, I.; Ha, A.; Zhao, X.; Lee, M.; Fischer, T.; Strouse, M.; Kivelson, D., A low-temperature amorphous phase in a fragile glass-forming substance. In *J Phys Chem-Us*, 1996; Vol. 100, pp 8518-8526.
82. Murata, K.-i.; Tanaka, H., Surface-wetting effects on the liquid-liquid transition of a single-component molecular liquid. In *Nat Commun*, 2010; Vol. 1, pp 16-9.
83. Mierzwa, M.; Paluch, M.; Rzoska, S.; Zioło, J., The liquid-glass and liquid-liquid transitions of TPP at elevated pressure. In *The Journal of Physical Chemistry B*, 2008; Vol. 112, pp 10383-10385.
84. Kurita, R.; Tanaka, H., Critical-like Phenomena Associated with Liquid-Liquid Transition in a Molecular Liquid. Supporting Online Material. In *Supporting Online Material*, 2004; pp 1-4.
85. Bolshakov, B.; Dzhonson, A., On the number of amorphous phases in n-butanol. In *DOKLADY PHYSICAL CHEMISTRY*, 2003; Vol. 393, pp 318-320.
86. Bolshakov, B.; Dzhonson, A., On the number of amorphous phases in n-butanol: Kinetics of free radicals oxidation by oxygen in frozen n-butanol. In *J Non-Cryst Solids*, 2005; Vol. 351, pp 444-454.
87. Derollez, P.; Hedoux, A.; Guinet, Y.; Danede, F.; Paccou, L., Structure determination of the crystalline phase of n-butanol by powder X-ray diffraction and study of intermolecular associations by Raman spectroscopy. In *Acta Crystallographica Section B: Structural Science, Crystal Engineering and Materials*, 2013; Vol. 69, pp 195-202.
88. Hédoux, A.; Guinet, Y.; Paccou, L.; Derollez, P.; Danède, F., Vibrational and structural properties of amorphous n-butanol: A complementary Raman spectroscopy and X-ray diffraction study. In *J Chem Phys*, 2013; Vol. 138, p 214506.
89. Wypych, A.; Guinet, Y.; Hedoux, A., Isothermal transformation of supercooled liquid n-butanol near the glass transition: Polyamorphic transitions in molecular liquids investigated using Raman scattering. In *Phys Rev B*, 2007; Vol. 76, p 144202.
90. Hassaine, M.; Jiménez-Rioboó, R. J.; Sharapova, I. V.; Korolyuk, O. A.; Krivchikov, A. I.; Ramos, M. A., Thermal properties and Brillouin-scattering study of glass, crystal, and "glacial" states in n-butanol. In *J. Chem. Phys.*, 2009; Vol. 131, p 174508.
91. Shmyt'ko, I.; Jiménez-Riobóo, R.; Hassaine, M.; Ramos, M., Structural and thermodynamic studies of n-butanol. In *J Phys-Condens Mat*, 2010; Vol. 22, p 195102.
92. Krivchikov, A.; Hassaine, M.; Sharapova, I.; Korolyuk, O.; Jiménez-Riobóo, R.; Ramos, M., Low-temperature properties of glassy and crystalline states of n-butanol. In *J Non-Cryst Solids*, 2011; Vol. 357, pp 524-529.
93. *Liquid crystals*. Princeton University Press: Princeton, 2002.
94. Collings, P. J.; Hird, M., *Introduction to liquid crystals chemistry and physics*. Taylor & Francis Ltd.: London, 1997.

95. Kurita, R.; Tanaka, H., Phase-ordering kinetics of the liquid-liquid transition in single-component molecular liquids. *J Chem Phys* 2007, *126* (20), 204505.
96. Tanaka, H., Two-order-parameter description of liquids: critical phenomena and phase separation of supercooled liquids. In *J Phys-Condens Mat*, 1999; Vol. 11, pp L159-L168.
97. Gebauer, D.; Kellermeier, M.; Gale, J. D.; Bergstrom, L.; Colfen, H., Pre-nucleation clusters as solute precursors in crystallisation. *Chem Soc Rev* 2014, *43* (7), 2348-71.
98. Erdemir, D.; Lee, A. Y.; Myerson, A. S., Nucleation of Crystals from Solution: Classical and Two-Step Models. *Acc Chem Res* 2009, *42*, 621.
99. Erdemir, D.; Chattopadhyay, S.; Guo, L.; Ilavsky, J.; Amenitsch, H.; Segre, C. U.; Myerson, A. S., Relationship between self-association of glycine molecules in supersaturated solutions and solid state outcome. *Phys Rev Lett* 2007, *99* (11), 115702.
100. Kawasaki, T.; Tanaka, H., Formation of a crystal nucleus from liquid. *Proceedings of the National Academy of Sciences* 2010, *107* (32), 14036-14041.
101. Bøjesen, E. D.; Iversen, B. B., The chemistry of nucleation. *CrystEngComm* 2016, *18* (43), 8332-8353.
102. Chung, S.-Y.; Kim, Y.-M.; Kim, J.-G.; Kim, Y.-J., Multiphase transformation and Ostwald's rule of stages during crystallization of a metal phosphate. *Nature Physics* 2008, *5* (1), 68-73.
103. Dey, A.; Bomans, P. H.; Muller, F. A.; Will, J.; Frederik, P. M.; de With, G.; Sommerdijk, N. A., The role of prenucleation clusters in surface-induced calcium phosphate crystallization. *Nat Mater* 2010, *9* (12), 1010-4.
104. Raiteri, P.; Gale, J. D., Water Is the Key to Nonclassical Nucleation of Amorphous Calcium Carbonate. *J Am Chem Soc* 2010, *132*, 17623.
105. Stephens, C. J.; Kim, Y. Y.; Evans, S. D.; Meldrum, F. C.; Christenson, H. K., Early stages of crystallization of calcium carbonate revealed in picoliter droplets. *J Am Chem Soc* 2011, *133* (14), 5210-3.
106. Wallace, A. F.; Hedges, L. O.; Fernandez-Martinez, A.; Raiteri, P.; Gale, J. D.; Waychunas, G. A.; Whitelam, S.; Banfield, J. F.; De Yoreo, J. J., Microscopic Evidence for Liquid-Liquid Separation in Supersaturated CaCO3 Solutions. *Science* 2013, *341*, 885.
107. Gebauer, D.; Voelkel, A.; Coelfen, H., Stable Prenucleation Carbonate Clusters. *Science* 2008, *322*, 1819.
108. Kovacs, T.; Meldrum, F. C.; Christenson, H. K., Crystal Nucleation without Supersaturation. *J Phys Chem Lett* 2012, *3* (12), 1602-6.
109. Demichelis, R.; Raiteri, P.; Gale, J. D.; Quigley, D.; Gebauer, D., Stable prenucleation mineral clusters are liquid-like ionic polymers. *Nat Commun* 2011, *2*, 590.
110. Georgalis, Y.; Kierzek, A.; Saenger, W., Cluster Formation in Aqueous Electrolyte Solutions Observed by Dynamic Light Scattering. *J Phys Chem B* 2000, *104*, 3405.
111. Jawor-Baczynska, A.; Sefcik, J.; Moore, B. D., 250 nm Glycine-Rich Nanodroplets Are Formed on Dissolution of Glycine Crystals But Are Too Small To Provide Productive Nucleation Sites. *Crystal Growth & Design* 2013, *13* (2), 470-478.
112. An, J.-G.; Hina, S.; Yang, Y.; Xue, M.; Liu, Y., Characterization of liquid crystals: a literature review. *Rev. Adv. Mater. Sci.* 2016, *44*, 398-406.
113. Ermakov, S.; Beletskii, A.; Eismont, O.; Nikolaev, V., Brief Review of Liquid Crystals. In *Liquid Crystals in Biotribology: Synovial Joint Treatment*, Springer International Publishing, 2016; pp 37-56.
114. Liquid Crystals. https://saylordotorg.github.io/text_general-chemistry-principles-patterns-and-applications-v1.0/s15-08-liquid-crystals.html (accessed 01/06/2017).
115. Slayter, E. M.; Slayter, H. S., *Light and Electron Microscopy*. Cambridge University Press: 1992.

116. Bradbury, S.; Evennett, P., *Contrast Techniques in Light Microscopy*. BIOS Scientific Publishers Limited: 1996.
117. Rawlins, D. J., *Light Microscopy*. BIOS Scientific Publishers Limited: Oxford, 1992.
118. Rubbi, C. P., *Light Microscopy*. John Wiley & Sons: Essential Data, 1994.
119. Murphy, D. B.; Oldfield, R.; Schwartz, S.; Davidson, M. W. Introduction to Phase Contrast Microscopy. http://www.microscopyu.com/articles/phasecontrast/phasemicroscopy.html (accessed 28 October 2015).
120. Robinson, P. C.; Davidson, M. W. Introduction to Polarized Light Microscopy. http://www.microscopyu.com/articles/polarized/polarizedintro.html (accessed 28 October, 2015).
121. Haidekker, M.; Brady, T.; Lichlyter, D.; Theodorakis, E., Effects of solvent polarity and solvent viscosity on the fluorescent properties of molecular rotors and related probes. In *Bioorganic chemistry*, 2005; Vol. 33, pp 415-425.
122. Turrell, G.; Corset, J., *Raman Microscopy: Developments and Applications*. Academic Press: 1996.
123. Lakowicz, J. R., *Principles of Fluorescence Spectroscopy*. Springer: 2006.
124. Strickler, S.; Berg, R., Relationship between absorption intensity and fluorescence lifetime of molecules. *The Journal of Chemical Physics* 1962, *37*, 814.
125. Uzhinov, B.; Ivanov, V.; Melnikov, M., Molecular rotors as luminescence sensors of local viscosity and viscous flow in solutions and organized systems. *Russian Chemical Reviews* 2011, *80* (12), 1179-1190.
126. Kuimova, M., Mapping viscosity in cells using molecular rotors. *Physical Chemistry Chemical Physics* 2012, *14* (37), 12671-12686.
127. Haidekker, M.; Theodorakis, E., Environment-sensitive behavior of fluorescent molecular rotors. *Journal of biological engineering* 2010, *4* (1), 11-24.
128. Steege, K.; Wang, J.; Uhrich, K.; Castner, E., Local Polarity and Microviscosity in the Hydrophobic Cores of Amphiphilic Star-like and Scorpion-like Macromolecules. Supporting Information. *Macromolecules* 2007, *40*, 1-12.
129. GmbH, B. H., *Modular FLIM Systems for Zeiss LSM 510 and LSM 710 Laser Scanning Microscopes. User Hanbook 4th edition*. 2009.
130. Jones, C.; Suhling, K., Refractive index sensing using fluorescence lifetime imaging (FLIM). 2006; Vol. 45, p 223.
131. Bonnett, P. E.; Carpenter, K. J.; Dawson, S.; Davey, R. J., Solution crystallisation via a submerged liquid–liquid phase boundary: oiling out. *Chemical Communications* 2003, (6), 698-699.
132. Gomez, L. R.; Vega, D. A., Amorphous precursors of crystallization during spinodal decomposition. *Phys Rev E Stat Nonlin Soft Matter Phys* 2011, *83* (2 Pt 1), 021501.
133. Jacobson, L. C.; Molinero, V., Can amorphous nuclei grow crystalline clathrates? The size and crystallinity of critical clathrate nuclei. *J Am Chem Soc* 2011, *133* (16), 6458-63.
134. Tenwolde, P.; Frenkel, D., Enhancement of Protein Crystal Nucleation by Critical Density Fluctuations. *Science* 1997, *277*, 1975.
135. Filobelo, L. F.; Galkin, O.; Vekilov, P. G., Spinodal for the solution-to-crystal phase transformation. *J Chem Phys* 2005, *123* (1), 014904.
136. Wang, Y.; Lomakin, A.; Latypov, R. F.; Laubach, J. P.; Hideshima, T.; Richardson, P. G.; Munshi, N. C.; Anderson, K. C.; Benedek, G. B., Phase transitions in human IgG solutions. *J Chem Phys* 2013, *139* (12), 121904.
137. Xu, L.; Kumar, P.; Buldyrev, S.; Chen, S.; Poole, P.; Sciortino, F.; Stanley, H., Relation between the Widom line and the dynamic crossover in systems with a liquid-liquid phase transition. In *P Natl Acad Sci Usa*, 2005; Vol. 102, pp 16558-16562.

138. Davey, R. J.; Schroeder, S. L.; ter Horst, J. H., Nucleation of organic crystals--a molecular perspective. *Angew Chem Int Ed Engl* 2013, *52* (8), 2166-79.
139. Lutsko, J. F.; Nicolis, G., Theoretical evidence for a dense fluid precursor to crystallization. *Phys Rev Lett* 2006, *96* (4), 046102.
140. Talanquer, V.; Oxtoby, D. W., Crystal nucleation in the presence of a metastable critical point. *The Journal of Chemical Physics* 1998, *109* (1), 223-227.
141. Mosses, J.; Turton, D. A.; Lue, L.; Sefcik, J.; Wynne, K., Crystal templating through liquid-liquid phase separation. In *Chem. Commun. (Camb.)*, 2015; Vol. 51, pp 1139-1142.
142. Wu, J.; Bertelo, C.; Caron, L., trans-1,2-dichloroethylene for improving fire performance of urethane foam. *J. Cell. Plast.* 2005, *41* (1), 15-27.
143. Wu, J.; Bertelo, C.; Enaux, V., trans-1,2-dichloroethylene as an additive for HFC-134a foam systems. *J. Cell. Plast.* 2005, *41* (4), 361-372.
144. Kawanishi, S.; Sasuga, T.; Takehisa, M., Existence of Novel Liquid Phases of trans-1, 2-Dichloroethylene at High Pressure. *J. Phys. Soc. Jpn.* 1981, *50*, 3080.
145. Kawanishi, S.; Sasuga, T.; Takehisa, M., A Novel Liquid State of trans-1, 2-Dichloroethylene. *J. Phys. Soc. Jpn.* 1982, *51*, 1579.
146. Zegrodnik, B., Hacura, A., Raman temperature study of liquid-liquid phase transition in trans-1,2-dichloroethylene. *Acta Phys. Pol.* 1989, *A75*, 469.
147. Merkel, K.; Kocot, A.; Wrzalik, R.; Ziolo, J., Origin of the liquid-liquid phase transition for trans-1, 2-dichloroethylene observed by IR spectroscopy. *J. Chem. Phys.* 2008, *129*, 074503.
148. Rzoska, S.; Zioło, J.; Drozd-Rzoska, A.; Tamarit, J.; Veglio, N., New evidence for a liquid–liquid transition in a one-component liquid. *J. Phys.: Condens. Matter* 2008, *20*, 244124.
149. Turton, D.; Martin, D.; Wynne, K., Optical Kerr-effect study of trans-and cis-1, 2-dichloroethene: liquid–liquid transition or super-Arrhenius relaxation. *Phys. Chem. Chem. Phys.* 2010, *12* (16), 4191-4200.
150. Kikuchi, K.; Kameda, T.; Higuchi, K.; Yamashita, A., A global classification of snow crystals, ice crystals, and solid precipitation based on observations from middle latitudes to polar regions. *Atmospheric Research* 2013, *132-133*, 460-472.
151. Hofmann, D.; Preuss, G.; Mätzler, C., Evidence for biological shaping of hair ice. *Biogeosciences* 2015, *12* (14), 4261-4273.
152. Kawanishi, S.; Sasuga, T.; Takehisa, M., Existence of Novel Liquid Phases of trans-1, 2-Dichloroethylene at High Pressure. In *J. Phys. Soc. Jpn.*, 1981; Vol. 50, p 3080.
153. Kawanishi, S.; Sasuga, T.; Takehisa, M., A Novel Liquid State of trans-1, 2-Dichloroethylene. In *J. Phys. Soc. Jpn.*, 1982; Vol. 51, pp 1579-60.
154. Merkel, K.; Kocot, A.; Wrzalik, R.; Ziolo, J., Origin of the liquid-liquid phase transition for trans-1, 2-dichloroethylene observed by IR spectroscopy. In *J Chem Phys*, 2008; Vol. 129, p 074503.
155. Rovira-Esteva, M.; Murugan, A.; Pardo, L. C.; Busch, S.; Ruiz-Martin, M. D.; Appavou, M. S.; Tamarit, J. L.; Smuda, C.; Unruh, T.; Bermejo, F. J.; Cuello, G. J.; Rzoska, S. J., Microscopic structures and dynamics of high- and low-density liquid trans-1,2-dichloroethylene. In *Phys Rev B*, 2010; Vol. 81, p 092202.
156. Rovira-Esteva, M.; Murugan, N. A.; Pardo, L. C.; Busch, S.; Tamarit, J. L.; Cuello, G. J.; Bermejo, F. J., Differences in first neighbor orientation behind the anomalies in the low and high density trans-1,2-dichloroethene liquid. In *J Chem Phys*, 2012; Vol. 136, p 124514.
157. Rzoska, S.; Zioło, J.; Drozd-Rzoska, A.; Tamarit, J.; Veglio, N., New evidence for a liquid–liquid transition in a one-component liquid. In *J Phys-Condens Mat*, 2008; Vol. 20, p 244124.

158. Turton, D. A.; Martin, D. F.; Wynne, K., Optical Kerr-effect study of trans- and cis-1,2-dichloroethene: liquid-liquid transition or super-Arrhenius relaxation. In *Phys Chem Chem Phys*, 2010; Vol. 12, pp 4191-4200.
159. Senker, J.; Rossler, E., Triphenyl phosphite: a candidate for liquid polyamorphism. In *Chemical Geology*, 2001; Vol. 174, pp 143-156.
160. Tanaka, H.; Kurita, R.; Mataki, H., Liquid-liquid transition in the molecular liquid triphenyl phosphite. *Phys. Rev. Lett.* 2004, *92* (2), 025701.
161. Kurita, R.; Tanaka, H., Critical-like phenomena associated with liquid-liquid transition in a molecular liquid. *Science* 2004, *306* (5697), 845-848.
162. Funston, A. M.; Fadeeva, T. A.; Wishart, J. F.; Castner, E. W., Fluorescence Probing of Temperature-Dependent Dynamics and Friction in Ionic Liquid Local Environments †. In *The Journal of Physical Chemistry B*, 2007; Vol. 111, pp 4963-4977.
163. Horng, M.; Gardecki, J.; Papazyan, A.; Maroncelli, M., Subpicosecond measurements of polar solvation dynamics: coumarin 153 revisited. In *The Journal of Physical Chemistry*, 1995; Vol. 99, pp 17311-17337.
164. Maroncelli, M., Continuum estimates of rotational dielectric friction and polar solvation. In *J. Chem. Phys.*, 1997; Vol. 106, pp 1545-1557.
165. Shirota, H.; Castner, E. W., Solvation in highly nonideal solutions: A study of aqueous 1-propanol using the coumarin 153 probe. In *J. Chem. Phys.*, 2000; Vol. 112, p 2367.
166. Zhao, X.; Kivelson, D., Light-scattering-studies of simple molecular supercooled liquids - structural considerations. In *J Phys Chem-Us*, 1995; Vol. 99, pp 6721-6732.
167. Van Der Zwan, G.; Hynes, J. T., Time-dependent fluorescence solvent shifts, dielectric friction, and nonequilibrium solvation in polar-solvents. In *J Phys Chem-Us*, 1985; Vol. 89, pp 4181-4188.
168. Wynne, K.; Hochstrasser, R., Coherence and adiabaticity in ultrafast electron transfer. In *Adv Chem Phys*, 1999; Vol. 107, pp 263-309.
169. Cave, R. J.; Castner, E. W., Time-Dependent Density Functional Theory Investigation of the Ground and Excited States of Coumarins 102, 152, 153, and 343. In *J Phys Chem A*, 2002; Vol. 106, pp 12117-12123.
170. Murata, K. i.; Kurita, R.; Tanaka, H., Dynamic Nature of the Liquid - Liquid Transition of Triphenyl Phosphite Studied by Simultaneous Measurements of Dielectric and Morphological Evolution. 2008; Vol. 982, p 196.
171. Lewis, J. E.; Maroncelli, M., On the (uninteresting) dependence of the absorption and emission transition moments of coumarin 153 on solvent. In *Chemical Physics Letters*, 1998; pp 197-203.
172. Jortner, J.; Bixon, M., Intramolecular vibrational excitations accompanying solvent - controlled electron transfer reactions. In *J. Chem. Phys.*, 1988; Vol. 88, pp 167-170.
173. Dobek, K., The influence of temperature on coumarin 153 fluorescence kinetics. In *J Fluoresc*, 2011; Vol. 21, pp 1547-1557.
174. Dobek, K.; Karolczak, J., The Influence of Temperature on C153 Steady-State Absorption and Fluorescence Kinetics in Hydrogen Bonding Solvents. In *J Fluoresc*, 2012; pp 1-11.
175. Veatch, S. L.; Keller, S. L., Separation of Liquid Phases in Giant Vesicles of Ternary Mixtures of Phospholipids and Cholesterol. In *Biophysical Journal*, 2003; pp 1-10.
176. Grant, C.; DeRitter, M.; Steege, K.; Fadeeva, T.; Castner, E., Fluorescence probing of interior, interfacial, and exterior regions in solution aggregates of poly (ethylene oxide)-poly (propylene oxide)-poly (ethylene oxide) triblock copolymers. In *Langmuir*, 2005; Vol. 21, pp 1745-1752.
177. Steege, K.; Wang, J.; Uhrich, K.; Castner, E., Local polarity and microviscosity in the hydrophobic cores of amphiphilic star-like and scorpion-like macromolecules. In *Macromolecules*, 2007; Vol. 40, pp 3739-3748.

178. Maroncelli, M.; Zhang, X.-X.; Liang, M.; Roy, D.; Ernsting, N. P., Measurements of the complete solvation response of coumarin 153 in ionic liquids and the accuracy of simple dielectric continuum predictions. *Faraday Discuss.* 2012, *154*, 409-424.
179. Wagner, B., The use of coumarins as environmentally-sensitive fluorescent probes of heterogeneous inclusion systems. In *Molecules*, 2009; Vol. 14, pp 210-237.
180. Kurita, R.; Shinohara, Y.; Amemiya, Y.; Tanaka, H., Microscopic structural evolution during the liquid-liquid transition in triphenyl phosphite. In *J Phys-Condens Mat*, 2007; Vol. 19, p 152101.
181. Molinero, V.; Sastry, S.; Angell, C. A., Tuning of Tetrahedrality in a Silicon Potential Yields a Series of Monatomic (Metal-like) Glass Formers of Very High Fragility. In *Phys. Rev. Lett.*, 2006; Vol. 97, pp 075701-4.
182. Bhat, M. H.; Molinero, V.; Soignard, E.; Solomon, V. C.; Sastry, S.; Yarger, J. L.; Angell, C. A., Vitrification of a monatomic metallic liquid. In *Nature*, 2007; Vol. 448, pp 787-U3.
183. Golovanov, D.; Lyssenko, K.; Antipin, M.; Vygodskii, Y.; Lozinskaya, E.; Shaplov, A., Long-awaited polymorphic modification of triphenyl phosphite. In *CrystEngComm*, 2005; Vol. 7, pp 465-468.
184. Mei, Q.; Siewenie, J.; Benmore, C.; Ghalsasi, P.; Yarger, J., Orientational correlations in the glacial state of triphenyl phosphite. In *The Journal of Physical Chemistry B*, 2006; Vol. 110, pp 9747-9750.
185. Senker, J.; Sehnert, J.; Correll, S., Microscopic Description of the Polyamorphic Phases of Triphenyl Phosphite by Means of Multidimensional Solid-State NMR Spectroscopy. In *J Am Chem Soc*, 2005; Vol. 127, pp 337-349.
186. Turton, D. A.; Corsaro, C.; Martin, D. F.; Mallamace, F.; Wynne, K., The dynamic crossover in water does not require bulk water. In *Phys. Chem. Chem. Phys.*, 2012; Vol. 14, pp 8067-7.
187. Taschin, A.; Bartolini, P.; Eramo, R.; Righini, R.; Torre, R., Evidence of two distinct local structures of water from ambient to supercooled conditions. In *Nat Commun*, 2013; Vol. 4, pp 1-1.
188. Murata, K.-i.; Tanaka, H., General nature of liquid–liquid transition in aqueous organic solutions. In *Nat Commun*, 2013; Vol. 4.
189. Franzese, G.; Malescio, G.; Skibinsky, A.; Buldyrev, S.; Stanley, H., Generic mechanism for generating a liquid-liquid phase transition. In *Nature*, 2001; Vol. 409, pp 692-695.
190. Moore, E. B.; Molinero, V., Structural transformation in supercooled water controls the crystallization rate of ice. In *Nature*, Nature Publishing Group: 2011; Vol. 479, pp 506-508.
191. Mosses, J.; Syme, C. D.; Wynne, K., Order Parameter of the Liquid-Liquid Transition in a Molecular Liquid. In *J Phys Chem Lett*, 2015; Vol. 6, pp 38-43.
192. Syme, C. D.; Mosses, J.; Gonzalez-Jimenez, M.; Shebanova, O.; Walton, F.; Wynne, K., Frustration of crystallisation by a liquid-crystal phase. *Sci Rep* 2017, *7*, 42439.
193. Hunt, N. T.; Turner, A. R.; Wynne, K., Inter- and intramolecular hydrogen bonding in phenol derivatives: a model system for poly-L-tyrosine. *J. Phys. Chem. B* 2005, *109* (40), 19008–19017.
194. Fecko, C.; Eaves, J.; Tokmakoff, A., sotropic and anisotropic Raman scattering from molecular liquids measured by spatially masked optical Kerr effect spectroscopy. *J Chem Phys* 2002, *117*, 1139–1154.
195. Fukasawa, T.; Sato, T.; Watanabe, J.; Buchner, R., Relation between dielectric and low-frequency Raman spectra of hydrogen-bond liquids. *Phys Rev Lett* 2005, *95* (19), 197802.
196. Hutter, J.; Bechhoefer, J., Banded spherulitic growth in a liquid crystal. In *Journal of crystal growth*, 2000; Vol. 217, pp 332-343.

197. Paolantoni, M.; Sassi, P.; Morresi, A.; Cataliotti, R. S., Infrared study of 1-octanol liquid structure. *Chemical Physics* 2005, *310* (1), 169-178.
198. Chen, L.; Zhu, W.; Lin, K.; Hu, N.; Yu, Y.; Zhou, X.; Yuan, L.-F.; Hu, S.-M.; Luo, Y., Identification of Alcohol Conformers by Raman Spectra in the C–H Stretching Region. *The Journal of Physical Chemistry A* 2015, *119* (13), 3209-3217.
199. Jensen, M. H.; Alba-Simionesco, C.; Niss, K.; Hecksher, T., A systematic study of the isothermal crystallization of the mono-alcohol n-butanol monitored by dielectric spectroscopy. *The Journal of Chemical Physics* 2015, *143* (13), 134501.
200. Hassaine, M.; Ramos, M. A., Calorimetric studies at low temperatures of glass-forming 1-butanol and 2-butanol. *physica status solidi (a)* 2011, *208* (10), 2245-2248.